

# **GPR-Based Periodic Monitoring of Reinforcement Corrosion in Chloride- Contaminated Concrete**

vorgelegt von  
Master of Science  
Shuxian Hong  
geb. in Quanzhou, Fujian, China

von der Fakultät VI - Planen Bauen Umwelt  
der Technischen Universität Berlin  
zur Erlangung des akademischen Grades

Doktor der Ingenieurwissenschaften  
- Dr.-Ing. -

genehmigte Dissertation

Promotionsausschuss:

Vorsitzender: Prof. Dr. rer. nat. Dietmar Stephan

Gutachter: Prof. Dr. rer. nat. Herbert Wiggensauser

Gutachter: Prof. Dr. –Ing. Frank U. Vogdt

Gutachter: Prof. Dr. Jens Tronicke

Tag der wissenschaftlichen Aussprache: 11. Juli. 2014

Berlin 2015



## **Abstract**

Chloride-induced reinforcement corrosion is one of the main deterioration processes in reinforced concrete structures. Most of the commonly used corrosion testing methods are electrochemical-based, like half-cell potential and linear polarization resistance. These methods provide indications of the current, instantaneous state of corrosion activity and could not measure the development of corrosion.

This thesis presents an experimental effort of periodical monitoring reinforcement corrosion with ground-coupled Ground-Penetrating Radar (GPR). A novel signal processing procedure was proposed for visualizing the development of reinforcement corrosion and the distribution of chloride in the cover concrete.

Laboratory experiments were carried out to monitor the accelerated reinforcement corrosion process. The data were processed in both time and time-frequency domains to investigate the sensitivity of GPR signal attributes to corrosion, moisture and chloride contamination. Based on the experimental observations, novel data processing methods were proposed in this thesis to visualize the reinforcement corrosion and chloride and/or moisture distribution with target-specified signal attribute mapping. To discover the development of corrosion from the historical GPR data, mutual information-based image registration technique was employed to align and normalize GPR data sets. Toolkits were developed in LabVIEW environment to implement the proposed signal processing methods. Half-Cell Potential and Laser-Induced Breakdown Spectroscopy (LIBS) were employed to verify the GPR observations and investigate the physical mechanisms.

The proposed method was applied to a case study, which showed an example of ten-year long-term periodic monitoring of the reinforcement corrosion under ambient environmental conditions. The results successfully visualized the development of corrosion within the last ten years, which warrants the possibilities of further transferring the proposed method to large-scale measurements on site.

## **Kurzfassung**

Bewehrungskorrosion durch Chlorideintragung ist einer der häufigsten Schadensprozesse im Betonbau. Die am häufigsten geutzten Methoden zum Auffinden von Bewehrungskorrosion arbeiten auf elektrochemischer Basis, wie zum Beispiel die Potenzialfeldmethode (HCP) oder die Methode zur Bestimmung des linearen Polarisationwiderstands. Mit Hilfe dieser Methoden kann man aktive Korrosion auffinden. Die gemessenen Ergebnisse sind Momentaufnahmen, sie können keine voranschreitende Korrosionsentwicklung darstellen.

Die vorgelegte Dissertation stellt experimentelle Ergebnisse periodischer Messungen mit Hilfe des Georadarverfahrens (GPR) vor. Es wird weiterhin eine neuentwickelte Methode für die Signalverarbeitung zur Visualisierung fortschreitender Bewehrungskorrosion und die Verteilung der Chloride in der Deckbetonschicht präsentiert.

In Laboruntersuchungen wurde auf der Oberfläche von Probekörpern mit künstlich beschleunigter Bewehrungskorrosion periodisch gemessen. Alle Daten wurden im Zeitbereich, sowie im Zeit-Frequenzbereich in der LabVIEW Softwareumgebung ausgewertet. Empfindlichkeit der GPR Signalparameter wurden untersucht. Auf der Grundlage der experimentellen Beobachtungen, werden in dieser Dissertation neue Methoden für die Signalverarbeitung vorgestellt, die die Bewehrungskorrosion und die Chlorid- und/oder Feuchteverteilung mit Hilfe einer parameterspezifischen flächigen Signalverteilung bildgebend darstellen können. Um die Korrosionsentwicklung anhand vorhandener GPR-Daten mit unterschiedlichem Messraster zu zeigen, mussten die Datensätze normalisiert werden. Dafür wurde eine Bildregistrierung mit ausgleichender Transformation der Datensätze durchgeführt. Verschiedene zerstörungsfreie Prüfmethoden einschließlich der bereits genannten Potenzialfeldmethode und die Laseremissionsspektroskopie (LIBS) wurden eingesetzt, um die mittels GPR ermittelten Beobachtungen zu verifizieren und die physikalischen Mechanismen untersuchen zu können.

Die vorgeschlagene Methode wurde in einer Fallstudie an einem Probekörper, der über zehn Jahre unter realen Umweltbedingungen der Korrosion ausgesetzt war, angewendet. Die Darstellung der Korrosionsentwicklung über Jahre belegt, dass die neue Methode zukünftig in Feldversuche überführt werden kann.

## Acknowledgments

The work was performed during a full-time Marie Curie Research Fellow position at the Federal Institute for Materials Research and Testing in Berlin, Germany, during the European Initial Training Network SmartEN-ITN, funded by the European Commission under contract number 238726. The thesis is part of the work of Workprogramme 3: Non-destructive evaluation in research topic 3.5 damage identification.

I would like to express my sincere gratitude to my supervisor Prof. Dr. –Ing. Frank U. Vogdt and the division leader of BAM Division 8.2 Dr. rer. nat. Herbert Wiggerhauser for their guidance and support during this research. I am indebted and grateful to my project advisor Ms. Rosemarie Helmerich for her patience, motivation and continuous support of my Ph.D study and research.

In particular, I am grateful to Dr. Wai-Lok Lai for enlightening me into research at first glance. I thank my colleagues in BAM Division 8.2: Mr. Thomas Kind, Dr. Christiane Trela, Dr. Martin Krause, Mr. Gerd Wilsch, Mr. Jens Wötmann, Ms. Kerstin Borchard, Mr. Marco Lange and Mr. Sean Smith for their cooperation, discussion and support.

My sincere thanks also go to Prof. Marios Chryssanthopoulos, Mr. Brian Bell and Dr. Steve Denton for offering me secondment opportunities at the University of Patras, Network Rail and Parsons Brinckerhoff.

My highest gratitude goes to my parents Zhenwu and Shaoshan, my husband Weihua, my daughter Boyuan and all the other members of my family, for their love and encouragement. Without their love and support, I would not have accomplished this work.

## **Contents**

<b>Abstract .....</b>	<b>I</b>
<b>Kurzfassung.....</b>	<b>II</b>
<b>Acknowledgments .....</b>	<b>III</b>
<b>Chapter 1 Introduction.....</b>	<b>1</b>
1.1 General overview .....	1
1.2 Research objectives.....	2
1.3 Research methodologies .....	2
1.4 Outline of the thesis .....	3
<b>Chapter 2 State of the Art .....</b>	<b>5</b>
2.1 Introduction.....	5
2.2 Chloride-induced reinforcement corrosion .....	5
2.2.1 Chloride transportation .....	6
2.2.2 Corrosion initiation .....	7
2.2.3 Corrosion propagation.....	7
2.3 Current corrosion inspection, detection and monitoring techniques.....	10
2.3.1 Visual inspection.....	10
2.3.2 Non-/semi-destructive testing .....	11
2.3.3 Corrosion monitoring.....	12
2.4 The previous research of GPR-based corrosion and chloride measurement .....	13
2.5 Research objects and approaches .....	14
<b>Chapter 3 Theoretical Background.....</b>	<b>15</b>
3.1 Ground-penetrating radar principles related to this work .....	15

3.1.1 Ground-Penetrating Radar (GPR) Systems .....	15
3.1.2 GPR data.....	16
3.1.3 GPR survey.....	18
3.2 GPR signal.....	23
3.2.1 EM wave reflection .....	23
3.2.2 EM wave propagation in subsurface material .....	23
3.2.3 Signal attenuation due to absorption .....	23
3.2.4 Dielectric properties of chloride-contaminated concrete.....	25
3.3 Signal processing.....	26
3.3.1 Basic data processing steps.....	26
3.3.2 Signal energy .....	29
3.3.3 Frequency analysis by using Fourier transform .....	30
3.3.4 Short-Time Fourier Transform (STFT) .....	33
3.3.5 S-Transform.....	33
3.3.6 Image registration technique .....	34
3.4 Other NDT techniques used in this work .....	36
3.4.1 Half-Cell Potential (HCP) .....	36
3.4.2 Laser-Induced Breakdown Spectroscopy (LIBS).....	37
<b>Chapter 4 Accelerated Corrosion Experiment and GPR-Based Periodic Monitoring ....</b>	<b>41</b>
4.1 Accelerated corrosion by means of impressing current technique .....	41
4.2 GPR system description .....	43
4.3 Data acquisition .....	43
4.4 Data processing .....	44
4.4.1 Attribute study .....	44
4.4.2 2D visualization by mapping the selected attributes .....	50

4.4.3 Image registration and normalization .....	52
<b>Chapter 5 Experimental Work .....</b>	<b>57</b>
5.1 Experiment 1 .....	57
5.1.1 Preparation of specimen.....	57
5.1.2 Experiment procedure .....	58
5.1.3 Results of GPR monitoring .....	60
5.1.3.1 Setup 1.....	60
5.1.3.2 Setup 2.....	71
5.1.4 Verification of the corrosion mapping .....	75
5.1.5 Verification of the chloride mapping .....	78
5.1.6 Discussion .....	81
5.1.6.1 Effect of corrosion on GPR signal .....	81
5.1.6.2 Effect of moisture and chloride on GPR signal .....	82
5.2 Experiment 2 .....	84
5.2.1 Preparation of specimens .....	84
5.2.2 GPR measurements .....	86
5.2.3 Experimental results.....	87
5.2.4 Discussion .....	97
5.3 Experiment 3 .....	98
5.3.1 The BAM Large Concrete Slab (LCS) .....	98
5.3.2 Artificial initiation to generate pitting corrosion .....	100
5.3.3 HCP monitoring .....	100
5.3.4 GPR-based corrosion monitoring.....	103
5.3.5 Summary .....	111



<b>Chapter 6 Conclusions .....</b>	<b>113</b>
<b>Publications.....</b>	<b>117</b>
<b>References.....</b>	<b>118</b>



## List of Figures

### Chapter 1

Figure 1.1 Causes of damages on bridge structures of the German highway network [1].....	1
--	---

### Chapter 2

Figure 2.1 Service life prediction model for reinforced concrete corrosion [11].....	5
Figure 2.2 Typical depth profiles of chloride ingress, measured with LIBS [14].....	6
Figure 2.3 Modified service life model .....	8
Figure 2.4 General reinforcement corrosion and cracking patterns. ....	8
Figure 2.5 Pitting corrosion.....	9
Figure 2.6 Phenomena of corrosion-related damage observed during visual inspection: (a) Concrete scaling; (b) Rust staining; (c) Leakage from the construction joint; (d) Leakage form cracks; (g) Efflorescence.....	11

### Chapter 3

Figure 3.1 Time domain GPR system operated in reflection mode. ....	16
Figure 3.2 (a) Signal paths between transmitter and receiver of ground-coupled system; (b) the recorded A-scan. ....	17
Figure 3.3 (a) B-scan data collection for a point reflector; (b) B-scan image of a point reflector.....	18
Figure 3.4 GPR vertical resolution, pulses are clearly separated when $\Delta t \geq w/2$ . ....	19
Figure 3.5 Propagation of a plane wave and its E- and M-field.....	20
Figure 3.6 Survey grid and GPR lateral resolution. ....	22
Figure 3.7 Velocity estimation by hyperbola fitting where the hyperbolic function has been fitted at a velocity of 0.12 m/ns. ....	29

Figure 3.8	Comparison of periodic and non-periodic sine wave and their results of FFT: (a) periodic sine signal, (b) non-periodic sine signal, (c) frequency spectrum of the signal in (a), frequency spectrum of the signal in (b) showing a spectral leakage.	31
Figure 3.9	Applying window function to reduce spectral leakage of non-periodic signal: (a) Hanning window, (b) windowed non-periodic sine wave (Figure 2.22 (b)), (c) frequency spectral of the signal in (b) with reduced leakage.	32
Figure 3.10	Deformation of image including: rigid translation, rigid rotation and scaling.	35
Figure 3.11	Principle of half-cell potential measurement.	37
Figure 3.12	LIBS experiment setup [14].	38
Figure 3.13	Typical LIBS spectrum measured on cement mortar, in which chloride is detected with a wavelength of 837.6 nm [14].	38
<b>Chapter 4</b>		
Figure 4.1	An example of accelerating corrosion setup by impressing direct current.	41
Figure 4.2	Signal processing flow used in this work.	44
Figure 4.3	Estimation of the peak-to-peak amplitude of an given time domain signal.	45
Figure 4.4	(a) Time domain A-scan signal with an RW reflected by a rebar embedded in a depth of 4.5 cm inside the specimen, (b) PSD of the signal (a).	45
Figure 4.5	(a) time-frequency spectrum of the signal shown in Figure 4.4 calculated by using STFT with a Hamming window, window size 1.5 ns, (b) frequency spectrum of DW, (c) frequency spectrum of RW.	46
Figure 4.6	(a) time-frequency spectrum of the signal shown in Figure 4.4 calculated by using general S-transform, (b) frequency spectrum of DW, (c) frequency spectrum of RW.	47
Figure 4.7	(a) Time domain A-scan signal with an RW reflected by a rebar embedded at 9 cm deep inside the specimen, (b) PSD of the signal (a).	48

Figure 4.8 (a) time-frequency spectrum of the signal shown in Figure 4.7 calculated by using STFT with a Hamming window, window size 1.5 ns, (b) frequency spectrum of DW, (c) frequency spectrum of RW.....	48
Figure 4.9 (a) time-frequency spectrum of the signal shown in Figure 4.7 calculated by using general S-transform, (b) frequency spectrum of DW, (c) frequency spectrum of RW.....	49
Figure 4.10 Developed S-transform toolkit: (a) user interface; (b) input and output of the toolkit.....	50
Figure 4.11 Developed Labview toolkits for GPR attributes mapping: (a) energy mapping (b) frequency mapping. ....	52
Figure 4.12 Flowchart for automatic image registration and intensity normalization. ....	54
Figure 4.13 Developed Labview toolkit for GPR image registration and intensity normalization. ....	55

## Chapter 5

Figure 5.1 Drawing of the test specimen and the measurement grid (unit: mm). ....	58
Figure 5.2 Set-up used in Setup1 for accelerating reinforcement corrosion. ....	59
Figure 5.3 GPR B-scan showing the location of four rebars in the first layer and the position of DW and RW in the A-scan signal (amplitudes are specified in arbitrary units).61	
Figure 5.4 . Time domain A-scans recorded on cathode bar during Setup 1. ....	62
Figure 5.5 . Time domain A-scans recorded on anode bar during Setup 1. ....	62
Figure 5.6 Variation of the normalized peak-to-peak amplitude (A) of RW (reflected wave) measured in Setup 1.....	64
Figure 5.7 Variation of the normalized peak-to-peak amplitude (A) of DW (reflected wave) measured in Setup 1.....	64

Figure 5.8 Corrosion imaging with normalized signal energy intensity plot (Setup 1): (a) baseline, before chloride contamination, (b) after chloride contamination, (c) Day 4, (d) Day 10, (e) Day 16, (f) Day 24, (g) Day 35, (h) Day 46.....	66
Figure 5.9 Half-cell potential contour map measured on day 16 of Setup 1. ....	67
Figure 5.10 Time-frequency spectrogram of the time domain signal recorded on anode bar (Figure 5.5): (a) baseline, before chloride contamination (b) after chloride contamination, (c) Day 4, (d) Day 10, (e) Day 16, (f) Day 24, (g) Day 35, (h) Day 46.....	69
Figure 5.11 Frequency spectra of the direct wave signals recorded on anode bar (point A)...	69
Figure 5.12 Frequency spectrum of the reflected wave signal recorded on cathode bar (point B).....	70
Figure 5.13 Mapping of direct wave peak frequency (Setup 1): (a) baseline, before chloride contamination, (b) after chloride contamination, (c) Day 4, (d) Day 10, (e) Day 16, (f) Day 24, (g) Day 35, (h) Day 46. ....	71
Figure 5.14 Time domain A-scans acquired at point C (cathode): during the experiment stage 2 with a 2.6 GHz antenna.....	72
Figure 5.15 Time domain A-scans acquired at point D (anode) : during the experiment stage 2 with a 2.6 GHz antenna.....	73
Figure 5.16 Effect of corrosion on the peak-to-peak amplitude (A) measured with a 2.6 GHz antenna in Setup 2 .....	73
Figure 5.17 Corrosion visualization with normalized signal energy intensity plot (Setup 2): (a) Day 2 , (b) Day 4, (c) Day 7, (d) Day 9, (e) Day 11, (f) Day 15. ....	74
Figure 5.18 Frequency spectra of the reflected wave signal recorded on anode bar (point D).	75
Figure 5.19 Location of the core samples. ....	76
Figure 5.20 (a) Core sample taken from position a (bar no. 1) in Figure 5.19, .....	76
Figure 5.21 Core sample taken form position b. ....	77

Figure 5.22 . Core sample taken from position f showing the corrosion initiation that occurred. .....	77
Figure 5.23 (a) Core sample taken from position d, (b) corroded rebar no. 1 and the stained concrete that surrounded it with rust particles.....	78
Figure 5.24 (a) The split core from position 1. (b) Spatially resolved chloride distribution: red = Cl, black = absence of Cl (aggregate), (c) Depth profiles of Chloride ingress.....	79
Figure 5.25 Location of the core samples for LIBS test.....	80
Figure 5.26 Chloride depth profile of the core samples measured with LIBS: (a) C1-C6; (b) C7-C9. ....	81
Figure 5.27 Schematic drawing of the test specimens and the measurement grid (unit: mm).85	
Figure 5.28 Schematic drawing of the reference specimens and the measurement grid (unit: mm).....	86
Figure 5.29 Time domain A-scans acquired above the rebar in specimen S1(a) and S2(b). ..	87
Figure 5.30 Effect of corrosion on the peak-to-peak amplitude (A) measured on: (a) S1, (b) S3 (c) S2 and (d) S4.....	89
Figure 5.31 Corrosion visualization of specimen S1 (cover: 4.5 cm, rebar diameter: 25 mm) with normalized signal energy intensity plot: (a) day 0, (b) day 6 and (c) day 18.90	
Figure 5.32 Corrosion visualization of specimen S3 (cover: 4.5 cm, rebar diameter: 16 mm) with normalized signal energy intensity plot: (a) day 0, (b) day 6 and (c) day 18.91	
Figure 5.33 Corrosion visualization of specimen S2 (cover: 9 cm, rebar diameter: 25 mm) with normalized signal energy intensity plot: (a) day 0, (b) day 6 and (c) day 18.92	
Figure 5.34 Corrosion visualization of specimen S4 (cover: 9 cm, rebar diameter: 16 mm) with normalized signal energy intensity plot: (a) day 0, (b) day 6 and (c) day 18.93	
Figure 5.35 Procedure to obtain the frequency spectra of the direct and reflected wave: (a) time domain A-scan measured on S1 (cover: 4.5 cm, rebar size: 25 mm); (b)	

time-frequency representation of (a); (c) frequency spectrum of DW; (d) frequency spectrum of RW. ....	94
Figure 5.36 Procedure to obtain the frequency spectra of direct wave and reflected wave: (a) time domain A-scan measured on S2 (cover: 9 cm, rebar size: 25 mm); (b) time-frequency representation of (a); (c) frequency spectrum of DW; (d) frequency spectrum of RW. ....	95
Figure 5.37 The frequency spectra of reflected waves acquired above the anode bar of test specimen: (a) S1 (cover: 4.5 cm, rebar size: 25 mm) and (b) S2 (cover: 9 cm, rebar size: 25 mm), during inducing corrosion process. ....	96
Figure 5.38 Frequency spectra of the rebar reflected waves. ....	97
Figure 5.39 BAM Large Concrete Slab. ....	98
Figure 5.40 Foundation of the slab with ducts to position radiation sources [58]. ....	99
Figure 5.41 Reinforcement of the corrosion testing area of LCS and the positions of corrosion initiation spots. ....	100
Figure 5.42 Potential mapping measured in March 2004, before installing the corrosion initialization spots [59]. ....	101
Figure 5.43 Potential mapping measured in April 2004, approximately 3 weeks after installing the corrosion initialization spots [59]. ....	102
Figure 5.44 Potential mapping measured in May 2011 ....	102
Figure 5.45 Potential mapping measured in August 2013. ....	103
Figure 5.46 GPR signal: (a) B-scan, (b) A-scan ....	104
Figure 5.47 Corrosion visualization with GPR signal energy mapping measured in (a) 2003, (b) 2005 and (c) 2013. ....	106
Figure 5.48 Magnitude relationship of the non-corroded area in the energy intensity plots measured in 2005 (Figure 5.47 (b)) and 2013 (Figure 5.47 (c)) ....	107



Figure 5.49	Magnitude relationship of the corroded area in the energy intensity plots measured in 2005 (Figure 5.47 (b)) and 2013 (Figure 5.47 (c)).	107
Figure 5.50	Normalized signal energy intensity mapping for corrosion visualization measured with a 1.5-GHz antenna in (a) 2003, (b) 2005 and (c) 2013.	109
Figure 5.51	Normalized signal energy intensity mapping for corrosion visualization measured with a 2.6-GHz antenna in 2013.	109
Figure 5.52	Mapping of direct wave peak frequency: (a) 2003, (b) 2005 and (c) 2013.	110

## List of Tables

### Chapter 2

Table 2.1 Corrosion damage and failure mode of general corrosion and pitting corrosion. ....	8
--	---

### Chapter 3

Table 3.1 Summarized commonly used window function for FFT. ....	32
--	----

### Chapter 4

Table 4.1 System specifications of SIR-20 and SIR-3000.....	43
---	----

### Chapter 5

Table 5.1 Comparison between setup 1 and 2 .....	60
--	----

Table 5.2 The design parameters of the test specimens and test programme .....	84
--	----

Table 5.3 Specifications of concrete mixture of LCS.....	99
--	----

Table 5.4 Parameters of the GPR measurements performed in 2003, 2005 and 2013. ....	104
---	-----

### Chapter 6

Table 6.1 Summary of correspondences and mechanisms for corrosion and chloride contamination with GPR signal attributes. ....	113
---	-----

# Chapter 1 Introduction

## 1.1 General overview

The corrosion of reinforcing steel is one of the major causes of deterioration, reduced durability or even failure of reinforced concrete structures. The German Committee for Structural Concrete (DAfStB-Deutscher Ausschuss für Stahlbeton) reported in the project report [1] that 66% of structural failures of German infrastructure building resulted from chloride-induced corrosion of reinforcement and 5% resulted from carbonation-induced corrosion (Figure 1.1).

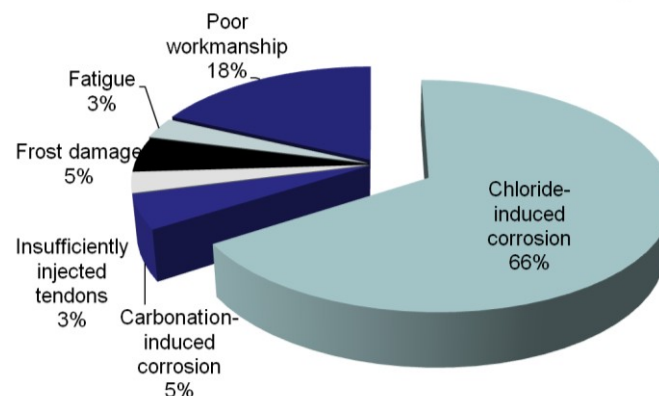


Figure 1.1 Causes of damages on bridge structures of the German highway network [1].

Most of the widely used conventional methods for corrosion detection are electro-chemical methods, like Half-Cell Potential (HCP) and Linear Polarization Resistance (LPR) measurements. These methods provide indications of the current state of corrosion activity and do not directly allow the detection of accumulative corrosion damage [2]. The inconvenience of these methods is that they require a connection to a steel bar as an electrode, which is semi-destructive and may interrupt the traffic when bridges and highways are investigated. To overcome these weaknesses, many efforts have been made to further develop advanced non-destructive testing (NDT) methods for corrosion detection.

Ground-penetrating radar (GPR) is a time- and cost-efficient non-destructive method for subsurface imaging. GPR was invented primarily for military use to locate buried landmines and underground tunnels. It is also used for geophysical survey to investigate soil layers [3], soil contamination area [4] or locate the depth of bedrocks [5], groundwater tables [6] and sinkholes [7]. With the development of a high-frequency antenna, GPR was adapted to civil

engineering applications such as tunnel lining condition assessments[8], embedded rebar and tendon ducts mapping, concrete cover depth and slab thickness measurements, detection of voids in concrete, and thickness estimation of road pavement, etc [9]. Recently, researchers have been investigating GPR techniques to assess the deterioration in concrete bridge decks, characterize the moisture or chloride content in concrete [10].

### 1.2 Research objectives

Three research objectives are identified as:

- Laboratory monitoring of accelerated reinforcement corrosion, and further extension of point monitoring to an area
- Investigating the response of GPR signal attributes to corrosion and chloride contamination
- 2-D visualization of the reinforcement corrosion and chloride contamination with target-specific signal attribute mapping
- Verifying the GPR observations about corrosion and chloride contamination by combining other NDT techniques, including HCP and laser-induced breakdown spectroscopy (LIBS)
- Transferring the laboratory monitoring methodology of accelerated corrosion to periodic monitoring of the corrosion under the on-site ambient environment

### 1.3 Research methodologies

An extensive literature search and review has been performed to identify the existing gaps of knowledge which help to justify the formulation of research approaches. A research plan was established and brought about an integrated and coordinated series of experiments. These experiments were performed within laboratory and on-site to monitor the reinforcement corrosion process. Several NDT methods, including half-cell potential, ultrasonic echo and laser-induced breakdown spectroscopy, were used to verify the GPR observations and investigate the mechanism. Data processing in both time and time-frequency domains were performed in LabVIEW<sup>TM</sup> software environment to obtain GPR signal attributes. These sets of attributes were subsequently amalgamated to investigate the mechanism and establish a signal processing procedure for corrosion and chloride mapping.

## **1.4 Outline of the thesis**

This thesis starts with a fundamental review of literature and theoretical background of reinforcement corrosion and GPR in Chapter 2 and Chapter 3. Chapter 4 introduces the method used for laboratory corrosion monitoring experiments, the proposed signal processing procedure and the Labview toolkits developed in this study.

Chapter 5 is the main chapter of this thesis, including three experiments:

- In Experiment 1, the feasibility of using GPR for corrosion detection/monitoring was tested by investigating the response of GPR signal attributes to accelerated general corrosion
- Experiment 2 tested the reproducibility of the result of Experiment 1. The influence of the parameters: rebar size and cover depth was investigated
- In Experiment 3, the knowledge of the laboratory monitoring of artificial corrosion was transferred to a long-term monitoring of a specimen that has been under ambient environmental conditions for the last ten years. The GPR data recorded in the past were processed with the new toolkits developed to visualize the corrosion and chloride distribution.

Finally, Chapter 6 concludes this research, summarizes the major contributions to knowledge achieved in this research, and suggests some recommendations for future research.



## Chapter 2 State of the Art

### 2.1 Introduction

This literature review is divided into five sections. Section 2.2 reviews the mechanism of chloride transportation and reinforcement corrosion in concrete. Section 2.3 reviews some current techniques for reinforcement corrosion inspection, detection and monitoring. Their functions' advantages and disadvantages are introduced and compared. Section 2.4 reviews the recent research on GPR-based reinforcement corrosion measurements. The important findings and the limitations will be discussed. Section 2.5 identifies the gaps in knowledge justifying the research approach on carrying out a series of experiments and the signal processing methods.

### 2.2 Chloride-induced reinforcement corrosion

In concrete, reinforcements are protected against corrosion, by the alkaline environment of the concrete. This protection could be broken down when it is exposed to the chloride contamination. Then, the corrosion initiates. With ongoing corrosion, the steel section deteriorates. The corrosion process of reinforcement during the service life of RC structures is usually divided into two distinct phases: the corrosion initiation phase ( $T_i$ ) and corrosion propagation phase ( $T_p$ ) as first proposed by Tuutti [11], as shown in Figure 2.1.

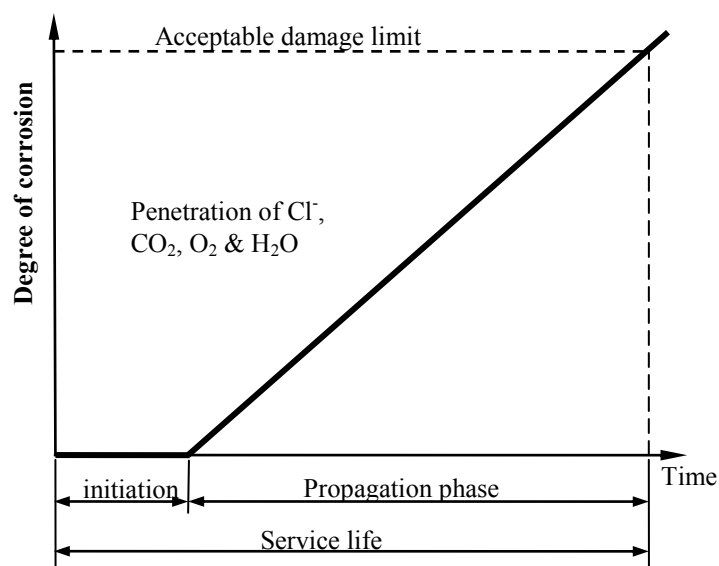


Figure 2.1 Service life prediction model for reinforced concrete corrosion [11].

### 2.2.1 Chloride transportation

Chloride-induced reinforcement corrosion caused either by use of de-icing salt or marine salt spray is a major problem in most parts of the world. Chloride ions penetrate into concrete via different mechanisms depending on the driving forces involved. The moisture state of concrete and the exposure environment determined the dominant mechanism by chlorides penetrate into concrete. Structures subjected to rain, wind, sun and snow. The chloride ions penetrate into concrete under cyclic wetting and drying, for which absorption and diffusion are main transport mechanisms [12, 13].

When the concrete surface is wet, water containing chlorides is quickly drawn into the concrete pore structure through capillary absorption to some depth in the concrete by absorption. However, for good quality concrete, the depth of wetting is small, and the effect of absorption is typically limited to a shallow cover region, resulting in a high concentration of chloride ions in a relatively short range from the concrete surface. The penetration depth also depends on drying depth. If the concrete cover dries out to a greater depth, the subsequent wetting will carry the chlorides deeper into the concrete.

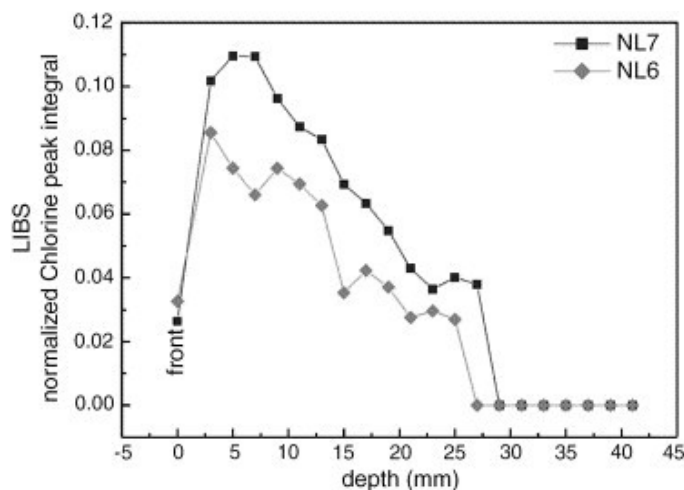


Figure 2.2 Typical depth profiles of chloride ingress, measured with LIBS [14].

After the chlorides are brought to a certain depth by absorption, diffusion becomes the primary transport mechanism. Diffusion is a slow process driven by the chloride concentration gradient. Chlorides are transported from the region with higher concentration in pore solution into the deeper region with minor concentration. Figure 2.2 shows a typical chloride depth profile of chloride ingress in marine environment measured with Laser-



Induced Breakdown Spectroscopy [14]. A region of higher chloride content is generally present in the near-surface concrete.

### **2.2.2 Corrosion initiation**

When the chloride ions reach the rebar surface and accumulate to a certain amount, the passive film can be dissolved and corrosion initiates. Field experience and research on the existing structures subjected to chloride ingress show that a threshold concentration of about 0.026% by weight of concrete is sufficient to break down the passive film. European standard EN 206-1 provides limiting values of 0.4% and 0.1% for reinforced and pre-stressed concrete, respectively. However, it should be remembered that only the free chlorides dissolved in the pore solution are important with regard to corrosion. Thus, the duration of initiation phase depends on the chloride-binding capacity of the hardened concrete paste matrix, exposure environment, concrete cover thickness and penetration rate of the corrosive agents.

### **2.2.3 Corrosion propagation**

Once the passive protection is destroyed, corrosion propagates if sufficient moisture and oxygen reach the reinforcement surface. The corrosion rate depends on the micro-climatic condition (temperature, moisture, pH value, etc.). There are mainly two types of corrosion damage: general and pitting corrosion.

**General corrosion** normally occurs in the case of uniformly distributed high chloride contamination or carbonation of the concrete or both resulting in a more uniform corrosion on the surface of reinforcement. The corrosion-related damage and failure mode are different from that of pitting corrosion. For general corrosion, Liu and Weyers [15] proposed a modified service life model as shown in Figure 2.3. In this model, the propagation period,  $T_p$ , is divided into three different periods: free expansion ( $T_{free}$ ), stress built-up ( $T_{stress}$ ) and concrete cracking ( $T_{cracking}$ ).

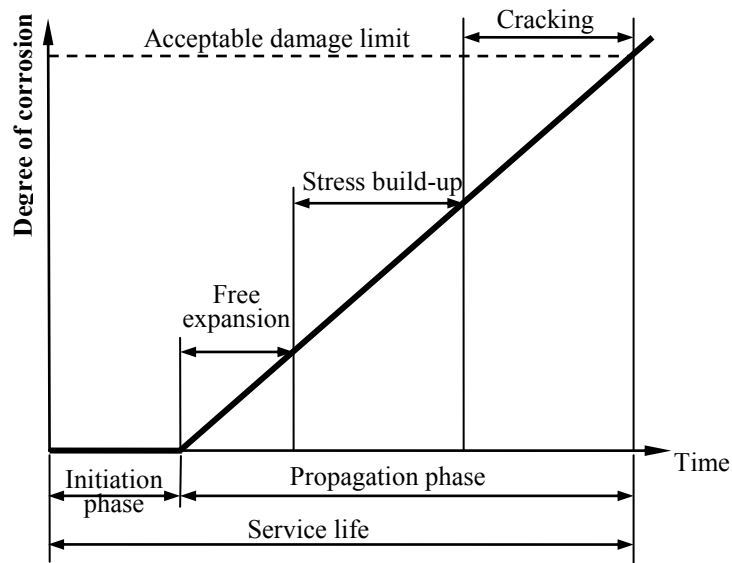


Figure 2.3 Modified service life model

The first is the free expansion period,  $T_{\text{free}}$ . During this period, the corrosion products accumulate in the concrete-steel interfacial transition zone (ITZ). It is reported that not all corrosion products contribute to expansive pressure on the concrete; some of them fill the voids and pores around the rebar which is named as steel-concrete ITZ; some of them migrate from ITZ into the concrete pores [16].

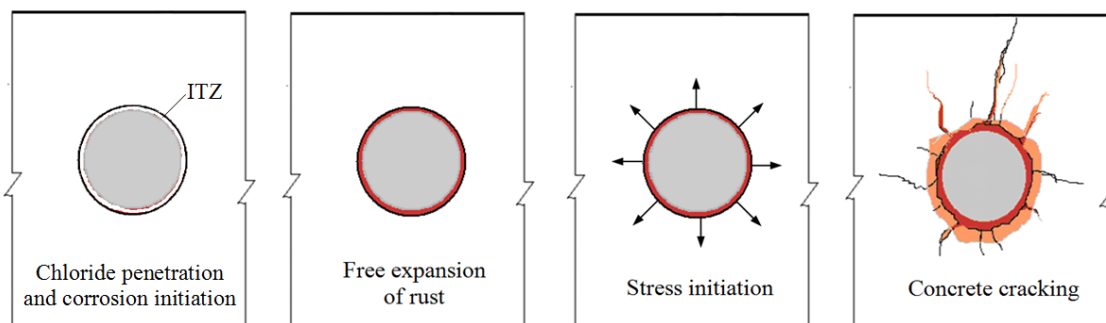


Figure 2.4 General reinforcement corrosion and cracking patterns.

Since the volume of the rust can be 1.5 to 6.4 times the volume of steel, once voids in ITZ are filled completely with the rust, it starts the period for stress built up,  $T_{\text{stress}}$ , in which the further rust accumulation causes expansive stress. The concrete around the rebar is considered as a thick-wall cylinder with a wall thickness equal to the thickness of concrete cover. When the expansive stress in the circumferential direction at every part of the ring reached the

tensile strength of concrete, then concrete starts to crack, which is the beginning of the cracking period,  $T_{\text{crack}}$ . In this period, the rust expansion-induced cracks propagate in concrete surrounding the reinforcing steels and the corrosion products diffused gradually into the cracks until some critical failure mode, such as the spalling or delaminations of concrete cover. The corrosion-cracking process is modeled by a schematic diagram proposed by Weyers [16] as shown in Figure 2.4.

**Pitting corrosion** normally happens in concrete with relative high conductivity and a moderate level of chloride. The passive film is broken down locally and the anodic reaction happens where the chloride concentration is high or the passive film is weak. Conversely, in other areas, where the steel remains passive or has a lower corrosion rate, the cathodic reaction happens. Pitting corrosion results in a rapid loss of rebar cross section. It generally occurs as a local corrosion pit, but the corrosion products are usually deposited over the larger remaining non-corroded area, without forming sufficient stress in the concrete matrix to cause cracking (Figure 2.5).

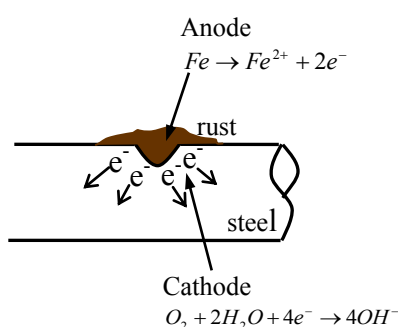


Figure 2.5 Pitting corrosion.

	General corrosion	Pitting corrosion
Cause	Carbonation or uniformly distributed high chloride contamination	Non-uniform distributed chloride contamination
Dimension	Uniform corrosion in an area	Localized
Damage	Expansion caused cracks, spallings and delaminations	Extreme loss of bar section occurs without signs of deterioration on the concrete surface.
Failure mode	Loss of bond between steel and concrete	Significant loss of steel section

Table 2.1 Corrosion damage and failure mode of general corrosion and pitting corrosion.

Table 2.1 summarizes the corrosion damage and failure mode of general corrosion and pitting corrosion. Since the damage and failure mechanism are different, the related corrosion testing methods can also be different. In Chapter 5, the change of GPR signal is going to be explained with the corrosion damage mechanism.

### 2.3 Current corrosion inspection, detection and monitoring techniques

There have been several techniques developed for structural inspection which can be classified into three levels:

- Visual inspection
- Non-destructive testing
- Corrosion monitoring

This section is going to provide a review of the corrosion inspection process based on the experience from the industrial visit and the advance non-destructive testing and structural health monitoring methods which had been developed in the academic institute and hold the potential for further industrial application.

#### 2.3.1 Visual inspection

Visual inspection is the standard method and usually the first step for detecting damage and assessing deterioration in most structures. It is carried out by the inspectors from the convenient access place with normal hand tools like hammers and torches, mapping defects and providing locations of the areas needing further tests. During a visual inspection, some phenomena can be observed related to corrosion deterioration: water leakage, concrete scaling, rust staining, cracking (relatively wide cracks which run parallel to the corroding reinforcement), delamination, spalling and efflorescence (Figure 2.6).



(a) Concrete scaling



(b) Rust staining



(c) Leakage from the construction joint



(d) Leakage from cracks



(e) Spalling



(f) Spalling and previous repair



(g) Efflorescence

Figure 2.6 Phenomena of corrosion-related damage observed during visual inspection: (a) Concrete scaling; (b) Rust staining; (c) Leakage from the construction joint; (d) Leakage from cracks; (g) Efflorescence.

### 2.3.2 Non-/semi-destructive testing

Visual inspection can reveal signs of corrosion only when the condition becomes numerous and dangerous. In order to reduce the repair cost and maintain the structure in better service

condition, it needs Non-Destructive Testing or monitoring techniques that detect the corrosion at an early stage.

HCP is one of the most common corrosion testing methods. It provides the likelihood of active corrosion in reinforced concrete by measuring the potential of corrosion activity. HCP method is adopted as a standard method with criteria for the interpretation given by the American Society for Testing and Material (ASTM) [17] and the German Society for Non-destructive Testing (DGZFP) [18]. However, the method has several drawbacks:

- The criteria are now recognized to be oversimplified. Ambient environment, like moisture, temperature, chloride content and cover concrete carbonation, etc., influence the results of HCP measurements
- HCP does not provide the information about the reinforcement. Reinforcement location and depth of cover have to be determined by a cover meter
- The method only provides indications of the risk of corrosion activity
- A destructive connection to the reinforcement is required.

**Linear Polarization Resistance (LPR)** is another electrochemical-based method [19], which allows for a direct measurement of the ongoing corrosion rate. It compromises the accuracy of HCP measurement caused by concrete carbonation of water saturation. However, just like for HCP, it requires a direct electrical connection to the steel reinforcement. LPR can measure the corrosion rate, which is instantaneous and not cumulative. The corrosion rate varies with time due to changes of the environmental conditions measurements like moisture, contamination of chlorides and/or carbonation [2]. It cannot be used to directly measure the cumulative loss of steel section. To use the LPR data to calculate reinforcing steel section loss and predict the remaining service life, “it is essential to take a series of measurements in order to understand the trends in the data rather than using individual values.” [19]

### 2.3.3 Corrosion monitoring

The traditional NDT methods are usually applied by the human operators and need adequate access to the structure which usually causes the interruption of traffic, especially for railway bridges. Many efforts have been made to develop embeddable sensors and monitoring system to monitor corrosion process. Most corrosion-monitoring sensors are electric-chemical-based to measure the potential or current due to corrosion activities. Anode ladder

[20] is one of the well-known corrosion sensors. It monitored the development of corrosion by comparing the potential between each rod of the ladder with a reference electrode. Another electro-chemical sensor is the LPR probe [19], which directly monitors the corrosion rate. Some sensors were developed based on electrical properties of concrete/steel. McCarter [21] proposed a sensor system to monitor the corrosion dynamics by measuring the spatial distribution of electrical conductivity which related with the ionic diffusion in cover concrete. Novel optical fibre sensors have also been adopted to monitor different factors related to the chemical properties of the cover concrete, such as chlorides [22], humidity [23] and pH changes [24] due to carbonation of concrete.

A feature of corrosion monitoring system with embedded sensor is that it only provides the local information of where the sensors have been embedded. If a large number of sensors are installed in order to monitor the corrosion in a large area or entire structure, the data acquisition and analysis may become issues.

## **2.4 The previous research of GPR-based corrosion and chloride measurement**

GPR is advantageous as a non-destructive testing tool for field measurement. It can acquire the data and visualize the subsurface objects (like reinforcements) rapidly and even during traffic. It has been used for assisting transportation projects by many studies, like detecting the location of reinforcements, measuring pavement thickness, detecting pavement voids. Narayanan et al. [25] initiated the research devoted to the detection of reinforcement corrosion in concrete with GPR in a field test. In their study, the amplitude reflection strength was used as an indicator of reinforcement corrosion with a combination of the statistical variance technique. Hubbard et al. [26] started to investigate the change of GPR signal attributes before and after accelerated corrosion. But, in that study, the influence of moisture was ignored and the mechanisms are still not clear. Lai et al. [27] started to continuously monitor the accelerated corrosion with GPR on one single point, giving the idea for this research in GPR-based corrosion monitoring. However, the changes of GPR signal attributes (like travel time, amplitude and frequency spectrum) are also strongly influenced by the dielectric properties of concrete, which is related with the chloride and moisture content in the concrete. In these previous researches, the influence of chloride and moisture has not been considered.

## **2.5 Research objects and approaches**

In this study, the 1D continuous monitoring is extended into a 2D periodic monitoring. Accelerated corrosion experiments were carried out under controlled conditions to separate the influences of corrosion and chlorides to GPR signal attributes. A novel method is proposed for corrosion and chloride mapping with the most sensitive GPR attributes.



## Chapter 3 Theoretical Background

### 3.1 Ground-penetrating radar principles related to this work

Ground-penetrating radar (GPR) is a geophysical method that uses electromagnetic waves to map the subsurface object. Similar to air-directed radar, it transmits a burst of electromagnetic energy and records the reflections from a target which has a contrast in the dielectric properties to the medium. GPR was invented primarily for military use to locate buried landmines and underground tunnels. It is also used for geophysical survey to investigate soil layers, soil contamination areas or locate the depth of bedrocks, groundwater tables and sinkholes. With the development of a high-frequency antenna, GPR was adapted to civil engineering applications such as road pavements and tunnel lining condition assessments, embedded rebar and tendon duct mapping, concrete cover depth and slab thickness measurements, detection of voids in concrete, and thickness estimation of road pavement, etc. Recently, researchers have been investigating GPR techniques to assess the deterioration in concrete bridge decks, characterize the moisture or chloride content in concrete, and, in particular, detect reinforcement corrosion.

#### 3.1.1 Ground-Penetrating Radar (GPR) Systems

GPR systems can be classified into two types according to the operating domain: time domain and frequency domain [28]. Most commercial GPR systems are operating in time domain. Figure 3.1 shows a typical time domain GPR system. It has three main components: transmitter and receiver that are directly connected to antennas and a control unit (timing). The timing unit controls the transmitting antenna to radiate a short high-frequency EM pulse into the ground. Most time domain GPR systems use ultra-wideband (UWB) signal. The center frequency of the transmitted pulse,  $f_c$ , around which most of the pulses' energy is concentrated, is determined by the design of the antenna and the associate bandwidth,  $B$ , is determined by the pulse length. In order to obtain a high depth resolution, the wavelength of the pulse has to be short. Thus, the ultra-wideband is used, for which the 3dB bandwidth similar to the center frequency of the pulse, i.e.,  $B \sim f_c$ . The receiving antenna measures the electric field of the reflected pulses and recorded as an analogue signal. After that, the recorded analogue signal is amplified and converted to a digital form in time domain.

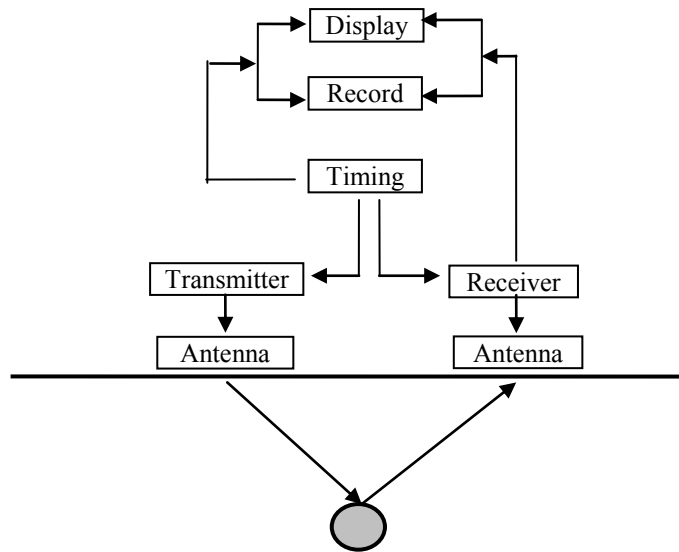


Figure 3.1 Time domain GPR system operated in reflection mode.

### 3.1.2 GPR data

The data recorded during a GPR survey are generally represented in one, two or three dimension, called A-, B- and C-scans, respectively:

- **A-scan**

A single trace of signal recorded by a GPR with the antennas placed at a given position is commonly known as A-scan. Depending on the way antennas are deployed, GPR systems can also be classified as air-coupled and ground-coupled systems, for which the recorded A-scan waveforms are different. For air-coupled systems, the antennas are typically 150 to 500 mm above the surface. When a pulse signal is transmitted, the receiving antenna records the first arrival wave, called direct wave (DW), which propagates directly from transmitter to receiver through the air. When the transmitted signal encounters the air-ground interface, part of the EM energy is reflected back by the air-ground interface and recorded as a ground wave (GW). The rest of the energy penetrates through the interface into the ground and is reflected by the subsurface object which has a significant dielectric contrast with the host material and is eventually recorded as a reflected wave (RW) in the A-scan. For a ground-coupled system, Figure 3.2(a), the antennas are placed on the test surface. It transmits higher energy into the subsurface material resulting in a higher penetration depth. The GPR signal has two direct waves: one propagates in the air, the other in the ground. When two antennas are close together within one or two wavelengths, these two waves overlap. When the receiver is

moved away from the transmitter at a sufficient distance, these two waves are then clearly separated in the A-scan. In this study, a single antenna was used as transmitter and receiver. A typical waveform is shown in (Figure 3.2 (b)).

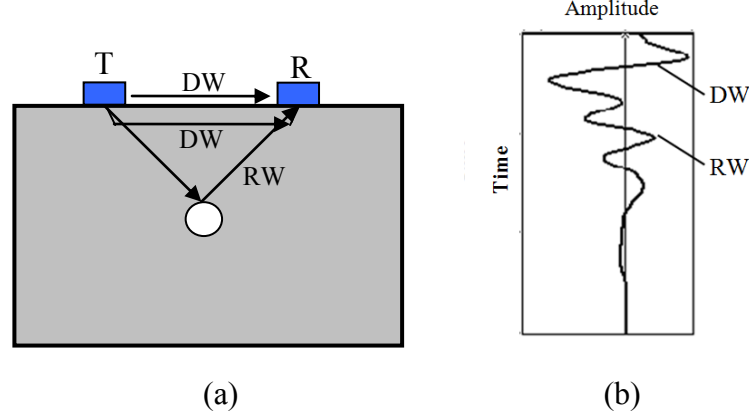


Figure 3.2 (a) Signal paths between transmitter and receiver of ground-coupled system; (b) the recorded A-scan.

#### • B-scan

By moving the antennas along a line in the x direction, a set of A-scans can be obtained, forming a two-dimensional B-scan), which represents a vertical slice in the ground. When the measurement line is perpendicular to a rebar, the resulting geometric signature of the rebar is a hyperbola-like curve in the GPR B-scan image (Figure 3.3 (b)). The vertex of the hyperbola is referred to as the uppermost location of the rebar. When the dielectric permittivity is known, the depth of the subsurface object can be estimated by:

$$d = v \cdot \frac{t}{2}, \quad (3.1)$$

where  $v$  is the velocity of an EM wave,  $t$  is the two-way travel time. The velocity of an EM wave propagating in a dielectric material is given by:

$$v = \frac{c}{\sqrt{\epsilon_r}}, \quad (3.2)$$

where  $c$  is the speed of light,  $\epsilon_r$  is the relative dielectric constant,  $\epsilon_r = \epsilon / \epsilon_0$ ,  $\epsilon_0$  is the dielectric constant of air.

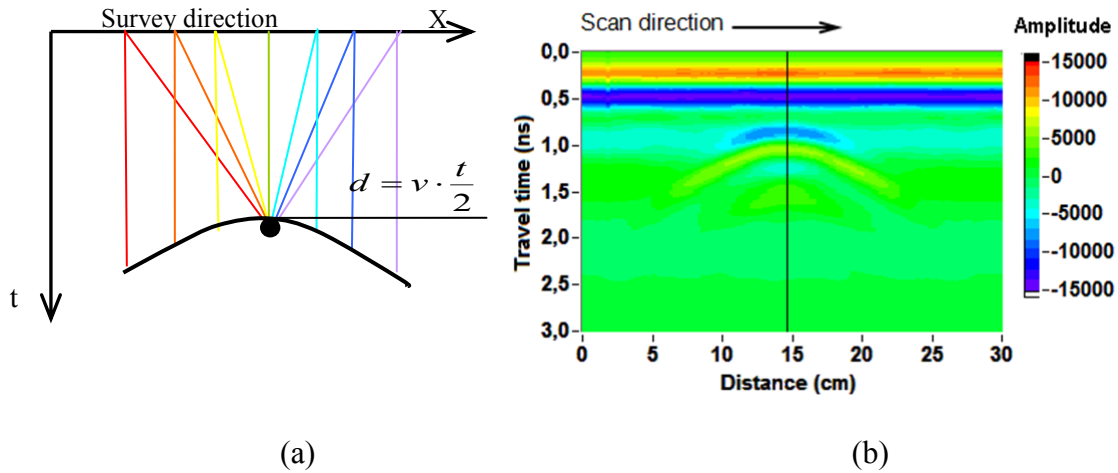


Figure 3.3 (a) B-scan data collection for a point reflector; (b) B-scan image of a point reflector.

### • C-scan

When moving the antennas over a regular grid in an x-y plane to scan an area, a data set in three dimensions can be obtained, called C-scan. Usually a C-scan is represented as a two-dimensional horizontal slice parallel to the x-y plane at a specified time  $t$ .

### 3.1.3 GPR survey

When a GPR survey is carried out in reflection mode, in the most common case, transmitting and receiving antennas are placed with a fixed distance, so-called common (or single) offset, and moved over the surface to detect the signal reflected or scattered from the subsurface objects. Single offset mode can be used to determine the depth of point reflector (like steel bar), which was described in section 3.1.2. But it cannot be used to determine the depth of flat sub-horizontal reflector (like water table in the soil) if no information about the dielectric permittivity of the material is available. In this case, one can use multi-offset mode, for which the distance between the antenna is increased stepwise while keeping a common midpoint, called Common-MidPoint (CMP), or keeping the transmitter at a fixed position, called Wide Angle Reflection or Refraction (WARR) [29]. For doing a monostatic reflection survey, several parameters have to be defined: operating frequency (or called center frequency) of the antenna, time window, sampling frequency, spatial sampling interval, measurement grid and antenna orientation.

- **Center frequency**

The center frequency has to be decided by considering the vertical resolution and penetration depth. The resolution indicates the limit to identify the two closest objects at a distance. GPR resolution consists of two aspects: lateral (or spatial) resolution and vertical (or depth) resolution. Lateral resolution is determined by the coverage area by the antenna, called footprint, which will be illustrated later in this section. Vertical resolution is controlled mainly by the wavelength ( $\lambda$ ) of the radar pulse propagating in the material which is explained in Figure 3.4. Two wavelets can be clearly separated when the time difference,  $\Delta t$  is bigger than half of  $w$  (pulse width at half amplitude). The wavelength is determined by the signal frequency,  $f$  and propagation velocity,  $v$ :

$$\lambda = v / f \quad (3.3)$$

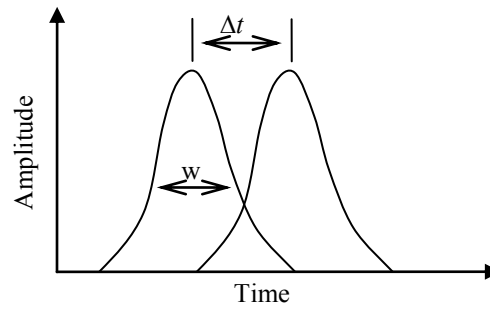


Figure 3.4 GPR vertical resolution, pulses are clearly separated when  $\Delta t \geq w/2$ .

The higher operating frequency can achieve better vertical resolution due to the signal attenuation occurring during propagation. Signal frequency decreases with increasing depth. Thus, resolution decreases as the depth increases. A special case for the vertical resolution is the detection of shallow objects in the ground or concrete. The direct wave is one of the main radar clutter interferences affecting target echo. The smaller wavelength in the transmitted pulse is the less overlapping of the direct wave and reflected wave. But, on the other hand, the maximum penetration depth depended on the attenuation of the signal in the material. The higher frequency signal that is transmitted, the smaller the penetration depth that is achieved. There is a trade-off between vertical resolution and penetration depth. Anna et al. [30] proposed a formulation to estimate the initial operating frequency:

$$f_c = \frac{150}{x\sqrt{\epsilon_r}} \text{ MHz} . \quad (3.4)$$

- **Antenna Polarization**

When a plane electromagnetic (EM) wave is transmitted by GPR antenna and travels in a single direction, the electric field and the magnetic field are perpendicular to each other and to the direction the plane wave is propagating in. As shown in Figure 3.5, the wave is travelling in the +z-direction, its electric-field (E-field) is oriented in the +x-direction and its magnetic field is in the +y-direction. Polarization is the direction of E-field while propagating. If the E-field stays along a single line, it is linearly polarized. If the E-field rotates in a circle, it is called circularly polarized. The polarization of an antenna is the polarization of the radiated fields produced by an antenna. Hence, antennas are often classified as "linearly polarized" or a "circularly polarized antenna".

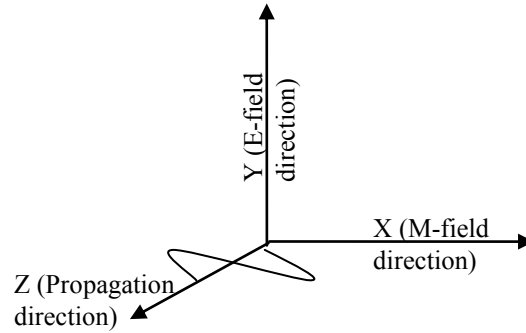


Figure 3.5 Propagation of a plane wave and its E- and M-field.

Due to the reciprocity theorem, antennas transmit and receive in a same polarization [31]. For two antennas polarized with an angle  $\theta$ , the power loss due to the mismatch of polarization is given as the Polarization Loss Factor (PLF):

$$PLF = \cos^2 \theta. \quad (3.5)$$

Hence, if a horizontally polarized antenna communicates with a vertically polarized antenna, there will be no reception.

- **Time Window**

The time window here means the duration of whole A-scan. Time window can be estimated by:

$$W = 1.3 \frac{2 \cdot D}{v}, \quad (3.6)$$

where  $D$  is the estimated depth of subsurface object,  $v$  is the propagation velocity. It is suggested by Anna [30] to increase the time window by 30% to take into account the uncertainties from the estimation of velocity and depth.

- **Sampling Frequency**

The continuous signal  $x(t)$  is sampled with a constant temporal sampling interval,  $dt$ , which is the inverse term of sampling frequency  $f_s$ . In order to reconstruct the original signal  $x(t)$  from a finite sequence of samples, the sampling frequency,  $f_s$ , must be at least twice as high as the bandwidth,  $B$ , i.e.:

$$f_s > 2B. \quad (3.7)$$

This criterion is called the Nyquist-Shannon sampling theorem or simply the sampling theorem. If the sampling theorem is not satisfied, the frequency component above  $f_s/2$  is indistinguishable from a lower-frequency component, called an alias.

For GPR signals with a center frequency ( $f_c$ ) equal to the 3 dB bandwidth, the Nyquist sampling criteria is transformed into:

$$f_s > 3f_c. \quad (3.8)$$

For the application, a value that is two times of the ideal criteria value is more appropriate:

$$f_s > 6f_c. \quad (3.9)$$

- **Lateral sampling interval**

When the measurement is carried out along a line in  $x$  direction, a set of A-scan signals are recorded with a certain distance  $\Delta x$ , called lateral sampling interval. In order to prevent spatial aliasing problems,  $\Delta x$  should not exceed the Nyquist sampling interval, which is one quarter of the wavelength in the host material:

$$\Delta x \leq \frac{\lambda}{4} = \frac{c}{4f_c \sqrt{\epsilon_r}}, \quad (3.10)$$

where  $f_c$  is the operating frequency of the GPR system.

- **Survey grid**

GPR survey is usually carried out within a regular grid, as shown in Figure 3.6. The spacing between the survey lines depends on the degree of target variation in the trend direction. When small point targets are interested, the line spacing should be estimated by considering the lateral resolution of an antenna. Lateral resolution is determined by the antenna footprint, which is the area illuminated by a GPR antenna. The radar antenna footprint is elliptical in shape and its size increases with depth, which can be estimated by:

$$a = \frac{\lambda}{4} + \frac{d}{\sqrt{\epsilon_r - 1}}, \quad b = \frac{a}{2}, \quad (3.11)$$

where  $a$  is the semi-major axis of an elliptical footprint, while  $b$  is the semi-minor axis,  $d$  is the depth of subsurface object.

For a small-point target, the survey line spacing should be smaller than the antenna footprint. For mapping reinforcements in concrete, when the direction of rebar is known, the survey lines should be oriented perpendicular to the rebars. The polarization should be placed parallel to the rebar to get the strongest reflection signal. If the survey is taken in two directions, a relatively bigger spacing between survey lines can be employed.

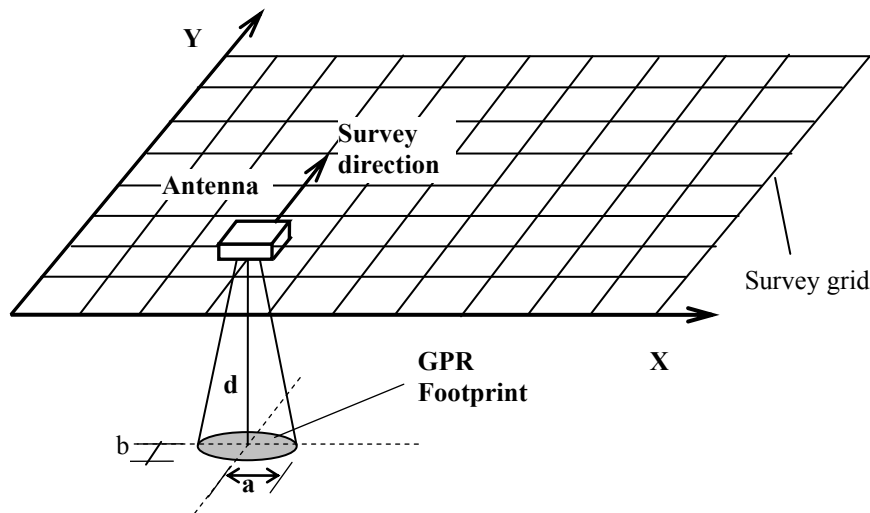


Figure 3.6 Survey grid and GPR lateral resolution.



## 3.2 GPR signal

### 3.2.1 EM wave reflection

When the transmitted EM wave encounters an interface between two materials with different electromagnetic properties, part of the signal travels through the interface to the next layer and the rest of the signal is reflected by the interface and recorded by the receiving antenna. The amplitude of the reflected signal is a function of the electromagnetic impedance of the two materials: the greater the contrast, the stronger the GPR reflection. For low-loss materials and at high GPR frequencies, magnitude of the returned signal amplitude of the reflected wave can be quantified with the reflection coefficient:

$$R = \frac{\sqrt{\varepsilon_1} - \sqrt{\varepsilon_2}}{\sqrt{\varepsilon_1} + \sqrt{\varepsilon_2}}, \quad (3.12)$$

where  $\varepsilon_1$  and  $\varepsilon_2$  are the dielectric constants of the upper and lower materials respectively.

When the transmitted signal encounters a metal surface, such as a rebar, since metals are strong reflectors of electromagnetic waves, the reflection is often stronger than that resulting from a change in dielectric properties. When the reflector is a linear object, such as rebar or tendon duct, the antenna-target polarization also influences the reflected signal [32]. When the polarization of the antenna is parallel to the rebar, the highest intensity of the recorded signal can be obtained.

### 3.2.2 EM wave propagation in subsurface material

As an EM pulse propagates, its energy reduces mainly due to two mechanisms: spreading and attenuation. Spreading is the distribution of the transmitted pulse energy over a spherical shell, which is related with the distance away from the source. Attenuation is caused by scattering and absorption of the signal, which depend on the properties of subsurface materials. For concrete, signal attenuation due to absorption is more important.

### 3.2.3 Signal attenuation due to absorption

For a plane wave, the monochromatic propagating electric field is given by:

$$E(r, t) = E_0 e^{i(kr - \omega t)}$$

where  $\omega$  is the angular frequency, the complex wave number is given by:

$$k = \beta + i\alpha$$

The real part of the wave number gives the phase velocity  $v_{ph} = \omega / \beta$  and the imaginary part gives the absorption attenuation:

$$\alpha = \omega \sqrt{\frac{\mu\epsilon}{2}} \cdot \sqrt{(\sqrt{1 + \tan^2 \delta} - 1)}, \quad (3.13)$$

$$\beta = \omega \sqrt{\frac{\mu\epsilon}{2}} \cdot \sqrt{(\sqrt{1 + \tan^2 \delta} + 1)}, \quad (3.14)$$

where the  $\epsilon$  is dielectric permittivity;  $\sigma$  is electrical conductivity;  $\mu$  is magnetic permeability, for non-magnetic materials like concrete,  $\mu$  is equal to the free space permeability,  $\mu_0$ ;  $\tan \delta$  is the loss tangent, defined as:

$$\tan \delta = \frac{\sigma}{\omega\epsilon}. \quad (3.15)$$

Strictly speaking, when the material only contains bounded charges, it can be named as dielectrics with the conductivity  $\sigma = 0$ , like solids and crystalline. The propagation of EM wave became similar with the propagation in vacuum with attenuation coefficient  $\alpha = 0$ , except the phase velocity is lower, given as in Eq. 3.2. If the dielectric permittivity is frequency independent, different frequency components of the EM wave will propagate through the material with the same phase velocity. The shape of the wavelet will not change during propagation. If  $\epsilon$  is frequency-dependent, the waves of different frequencies will propagate with different phase velocities, resulting in a phenomenon called wave dispersion.

In GPR frequency range, the dielectric permittivity of most dry solid materials can be simplified to a frequency-independent constant. But for the material in which the molecules have permanent electric dipole moments, which may be covalently bonded gases or liquid (like water), the dielectric permittivity and conductivity are frequency-dependent and complex quantities:

$$\epsilon = \epsilon' + i \cdot \epsilon'' \quad (3.16)$$

$$\sigma = \sigma' + i \cdot \sigma'' \quad (3.17)$$

To take into account both of these properties, an effective dielectric permittivity,  $\epsilon_e$ , is defined as [33]:

$$\varepsilon_e = \varepsilon + \frac{\sigma}{i\omega} = (\varepsilon' + i\varepsilon'') + \frac{\sigma' + i\sigma''}{i\omega} = \left(\varepsilon' + \frac{\sigma'}{\omega}\right) + i\left(\varepsilon'' + \frac{\sigma''}{\omega}\right) = \varepsilon'_e + i\varepsilon''_e, \quad (3.18)$$

where  $i^2 = -1$ . The real part of the effective permittivity  $\varepsilon'_e$  represents the capacity of the dielectric media to store the energy of EM wave and influences the wave velocity. The imaginary part  $\varepsilon''_e$  represents the loss of energy due to absorption. The energy adsorption happens primarily due to dielectric relaxation and electrical conduction. The energy losses due to dielectric relaxation is a result of the friction occurring between the polar molecules when they direct their dipolar moment parallel to the E-field. The losses due to conduction are related with the friction between moving free charges and bounded particles. In GPR frequency range, the energy losses of high-frequency component in an EM pulse are more pronounced, leading to a downshift of center frequency in its frequency spectrum.

### 3.2.4 Dielectric properties of chloride-contaminated concrete

The attenuation of EM wave in a lossy dielectric material is related with both dielectric permittivity and conductivity. Chloride-contaminated concrete is a kind of lossy dielectric material. The theory of EM wave attenuation in single-phase medium in section 3.2.3 can be applied to multiple-phase medium, such as concrete, by adopting a mixing model. The behavior of concrete dielectric properties can be decomposed into three phases: a solid phase, including all the solid components (aggregates, hydrated components, anhydrous cement, etc.); a gaseous phase (air); and a liquid phase, which is pore solution. The effective permittivity of concrete can be simply expressed as a mixture law proposed by Halabe [34]:

$$\sqrt{\varepsilon_e} = (1 - \phi)\sqrt{\varepsilon_m} + (1 - S_w)\phi\sqrt{\varepsilon_a} + \phi S_w\sqrt{\varepsilon_{sw}}, \quad (3.19)$$

where:

$\varepsilon_m$  is relative permittivity of the solid phase (matrix);

$\varepsilon_a$  is relative permittivity of the gaseous phase (air);

$\varepsilon_{sw}$  is the relative permittivity of the liquid phase (pore solution);

$S_w$  is the degree of saturation;

$\phi$  is the porosity of concrete.

The relative permittivity of concrete solid phase is a real number that normally lies between 3 and 5, and for gaseous phase, the air (dry) in pores is also a constant value 1. In chloride-contaminated concrete, the free chlorides can exist in pore solution or in crystalline form. The relative permittivity of crystalline sodium chloride is 5.9.

Based on Equation 3.19, the imaginary part of complex permittivity of concrete is mainly contributed by pore solution. The permittivity and conductivity of a sodium chloride solution at 20°C had been measured by Peyman [35] for different concentrations and over the frequency range 0.13-20 GHz. In the frequency band of GPR, normally 10 MHz to 4 GHz, the relative dielectric permittivity of NaCl-solution ranges from 81 (pure water) to 40 (high salinity 5 mol/L), while the conductivity ranges from 0 S/m (pure water) to 23 S/m (high salinity 5 mol/L).

### 3.3 Signal processing

Signal Processing is the art and science which derives meaning or significance from acquired raw data for the purposes of analysis or enhancement. The general processing techniques for GPR data are more developed for enhancing the 2D time-distance record (B-scan) and generating the 3D images of the subsurface. The basic processing steps, such as data editing, dewow filtering, time-zero correction, band-pass filtering, gain control and velocity estimation etc, are usually applied to the raw data to correct the system error and improve the data quality. There are several dedicated proprietary software that can be used to do this processing, like RADAN<sup>TM</sup> from GSSI and ReflexW from Sandmeier Software.

In addition, there is a more advanced analysis tools called attribute analysis, which helps the user to extract further information from the data to help to characterize the physical/natural property of the material. Signal attributes such as energy, coherency, similarity, frequency, and phase relation had been analyzed in some specific studies. Combining with advanced processing techniques, it is usually highly specialized and requires understanding of the mechanism.

#### 3.3.1 Basic data processing steps

- **Data editing**

This is normally the first step for GPR signal processing to correct mistakes in the measurements (e.g. de-saturation or de-clipping) as well as reversing profile direction, cutting or merging files, etc.

- **Dewow filtering**

This step of processing aims to remove the initial DC signal component and subsequent decay of ‘Wow’ noise which is very low-frequency components from the signal. Wow noise is caused by the swamping or saturation of the recorded signal by early arrivals and/or the close proximity of receiving and transmitting antenna. Dewow filter performs on each trace independently and shifts the data to the mean zero level. In ReflexW, Dewow filter is applied on each trace by calculating a mean value in a moving time window and subtracting the mean value from the central point of the window. The size of the window has to be carefully selected depending on the intention. If the size of the time window is improperly selected, the signal spectrum will be distorted.

- **Time-zero correction**

The first arrival time of the direct wave can have a drift when the antenna moves on an uneven surface. The drift may also be caused by the temperature difference between the instrument electronics and the air temperature. In order to correct this drift and calculate the arrival time of the reflected wave, one has to define a time point on the direct wave as the beginning of an A-scan time trace, so called ‘time-zero’. Traces have to be adjusted to this common time-zero position before applying other processing methods. There are several criteria suggested by some researchers to define the time-zero position. For most cases, the positive or negative peak of direct wave, or the zero amplitude point between these two peaks, is used. Lai et. al. [36] suggest the first differentiating point before the direct wave of the A-scan when doing frequency analysis. Yelf et. al. introduce a calibrate value in advance of the first positive peak of the direct wave by antenna lifting tests [37].

- **Band-pass filtering**

A combination of both high- and low-pass filters is applied in the frequency domain to filter the frequency components in a specific band pass region and remove signal noise at

frequencies either higher or lower than the main GPR signal band. To avoid removing the main signal components, it is suggested to use a pass region equal to 1.5 times the peak frequency and set symmetrically around it [38], e.g. for a 2-GHz peak frequency, the pass region should be 0.5-3.5 GHz. Due to the ground-air coupling, the peak frequency of the measured data is usually lower than the center frequency of the antenna, which has to be taken into account for setting the pass region.

- **Gain control**

During propagation, the radar signal energy decays due to spreading, attenuation and scattering, as explained in section 3.2. The reflected amplitude from the deep object becomes small and can be invisible. Therefore, most of the time, GPR signal has to be time-gained to compensate the rapid fall-off. One of the most common gain functions is automatic gain control (AGC), which equalizes the amplitudes within a window all the way down each trace. When a signal is applied with AGC, it tends to keep some information from the amplitude of the other reflections in the window; thus, the amplitude of the signal cannot be used to characterize the subsurface material or objects. Another popular gain function is spherical and exponential gain compensation (SEC), with which a linearly increasing time gain combined with an exponential increase is applied. The velocity and attenuation of signal through the trace is estimated in order to compensate the spherical spreading losses and exponential energy dispersion [39].

- **Velocity estimation and depth conversion**

To convert the time domain signal into the depth scale, an average of the signal travel velocity has to be estimated. Techniques of GPR velocity estimation are related to the data collection modes. For monostatic system (reflection mode operating with single antenna or two antennas casting in fix distance), signal velocity can be estimated by Hyperbolic fitting. An example of this is shown in Figure 3.7, where the hyperbolic function has been fitted at a velocity of  $0.12 \text{ m/ns}$ . The related algorithm can be found in the reference [40, 41].

There are other techniques available, such as signal deconvolution, to remove the effect of source wavelet, leaving the reflected impulses of the subsurface only; migration to convert the time-domain data to a depth scale and develop the more spatial realistic images of the subsurface, etc. Although many different GPR signal processing techniques are available, it

doesn't mean it would be necessary to apply all the processing steps. The processing steps have to be chosen based on the quality of the raw data and purpose of the investigation. The processing which is used has to be fully understood and avoid introducing additional errors or bias into the data.

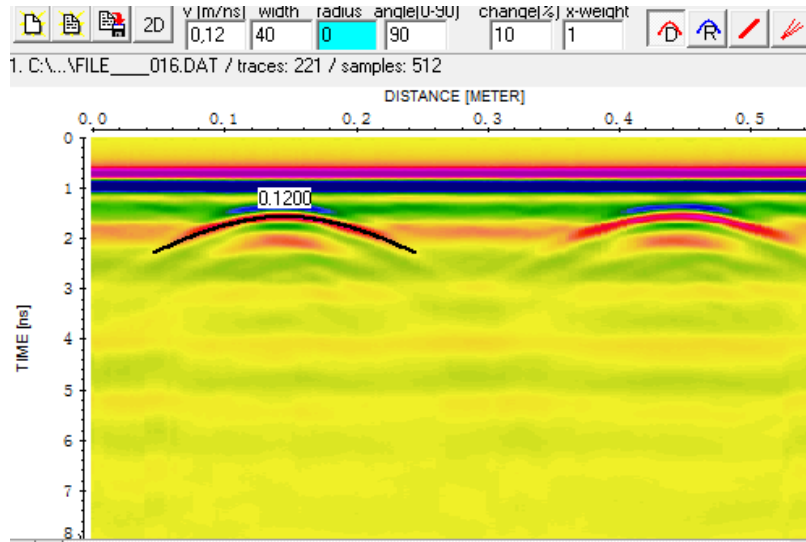


Figure 3.7 Velocity estimation by hyperbola fitting where the hyperbolic function has been fitted at a velocity of 0.12 m/ns.

After the basic processing steps, 3D GPR data sets are usually reconstructed as time-slices (C-scan). Subsurface objects at different depths can be visualized with signal amplitude. In addition, signal attributes can be used to extract useful information and provide a powerful aid for specific investigation purposes.

### 3.3.2 Signal energy

Signal energy is usually used to highlight the amplitude difference in an area. It is commonly used in archaeology GPR survey [42, 43]. The total energy of the discrete-time signal  $x(n)$  is calculated as:

$$\sum_{n_2}^{n_1} |x(n)|^2, \quad (3.20)$$

where  $x(n)$  is the signal trace after background removal;  $n_1, n_2$  are the start and end positions of the reflected wave. Evaluation of this equation over all survey lines and interpolated in area result in a so-called energy intensity plot in the depth of subsurface objects.

### 3.3.3 Frequency analysis by using Fourier transform

As illustrated in section 3.2.2, EM waves are subject to frequency-dependent attenuation when it propagates in the subsurface material as a result of absorption and dispersion. In time-domain, the absorption is related to amplitude decay due to the energy loss during propagation, while dispersion refers to the pulse deformation with a broader pulse. In frequency-domain, a signal disperses as its spectrum becomes narrower and shifts toward lower frequencies. Frequency analysis has been used by several authors to characterize the material properties [36].

For frequency analysis, Fourier transform is a powerful tool which has been commonly used. It was proposed by the French mathematician Joseph Fourier in 1822 and expresses a time function  $x(t)$  in terms of a sum of its projections onto a set of orthogonal basic functions ( $\{\sin(2\pi ft), \cos(2\pi ft), f \in R\}$ , or equivalently  $\{e^{-i2\pi ft}, f \in R\}$ ):

$$FFT(x(t)) = X(f) = \int_{-\infty}^{\infty} x(t) \cdot \exp(-i \cdot 2\pi ft) dt, \quad (3.21)$$

where  $i^2 = -1$ ,  $X(f)$  is the Fourier transform of  $x(t)$ , often called the spectrum of  $x$ . The magnitude of  $X(f)$  gives how much power  $x(t)$  contains at a particular frequency  $f$ .

$x$  can be obtained by calculating the inverse Fourier transform:

$$IFFT(X(f)) = x(t) = \int_{-\infty}^{\infty} X(f) \cdot \exp(i \cdot 2\pi ft) df. \quad (3.22)$$

The experimental signals were obtained from a data acquisition system with a sampling interval  $\Delta t$  within a total measurement time  $T$ . The continuous Fourier transform can be modified into the discrete Fourier transform (DFT), which is defined as:

$$DF(x_k) = X_k = \sum_{n=0}^{N-1} x_n e^{-i \frac{2\pi}{N} nk}, \quad (3.23)$$

where  $N = T / \Delta t$  is the number of samples,

$x_n$  ( $n = 1, 2, \dots, N-1$ ) is the sampled discrete signals.



To compute the DFT, a fast Fourier transform (FFT) algorithm was first invented by Carl Friedrich Gauss in 1805. The basic assumption of the FFT is that a signal is periodic. Figure 3.8 (a) and (c) show a periodic sine wave and its FFT frequency spectrum which contains a narrow peak at 10 Hz. When the signal is modified to a non-periodic as shown Figure 3.8 (b), the frequency spectral computed with FFT is then suffered from spectrum leakage with lower amplitude and dispersed energy which makes it more difficult to identify the peak frequency (Figure 3.8 (d)). To reduce the spectral leakage, a window function (e.g. Hanning window shown in Figure 3.9 (a)) can be applied to the signal to modify the non-periodic signal in Figure 3.9 (b) into a signal that is zero at the beginning and end as shown in Figure 3.9 (b). The computed frequency spectral is also applied with a weighting factor so that a spectral similar to Figure 3.9 (c) can be obtained.

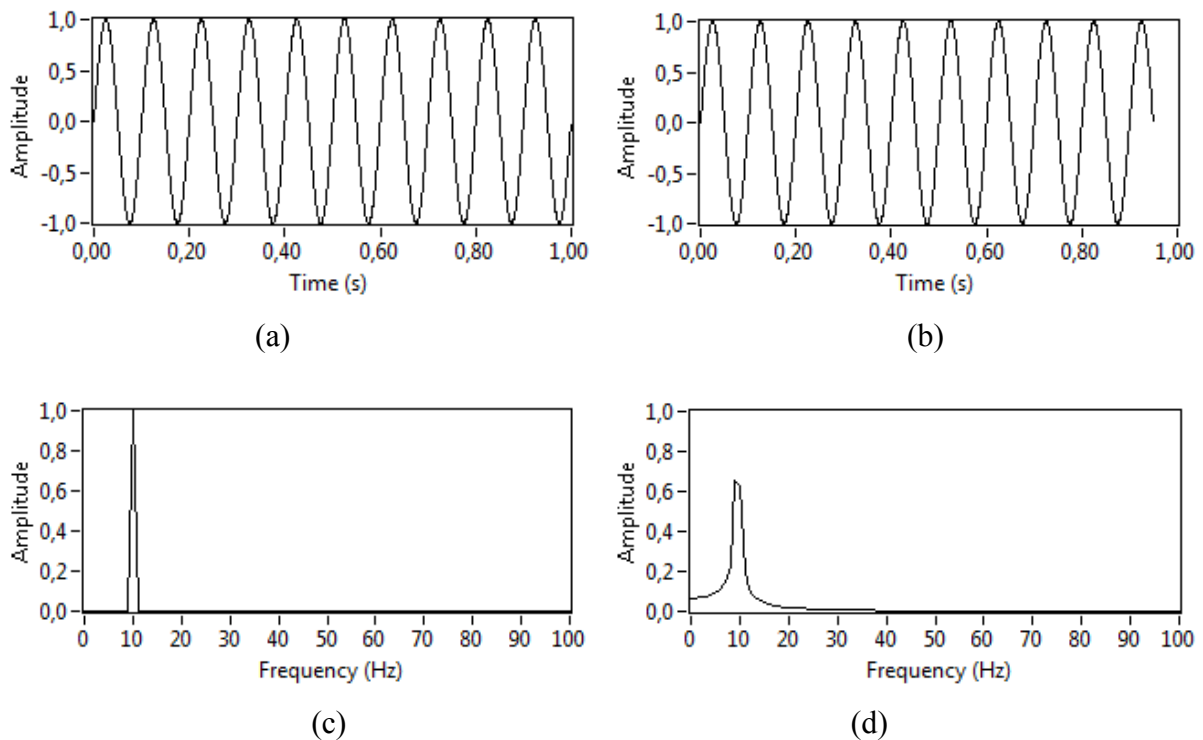


Figure 3.8 Comparison of periodic and non-periodic sine wave and their results of FFT: (a) periodic sine signal, (b) non-periodic sine signal, (c) frequency spectrum of the signal in (a), frequency spectrum of the signal in (b) showing a spectral leakage.

There are several window functions available. The most common windows are summarized in the Table 2.1. The best type of window function should be chosen for each specific application based on the type of signal and the desired frequency resolution. A

drawback of using window function is that it reduces the contribution of the beginning and ending part of the signal in the calculation of the spectrum. The solution involves calculating the average spectral from overlapping sequences [44].

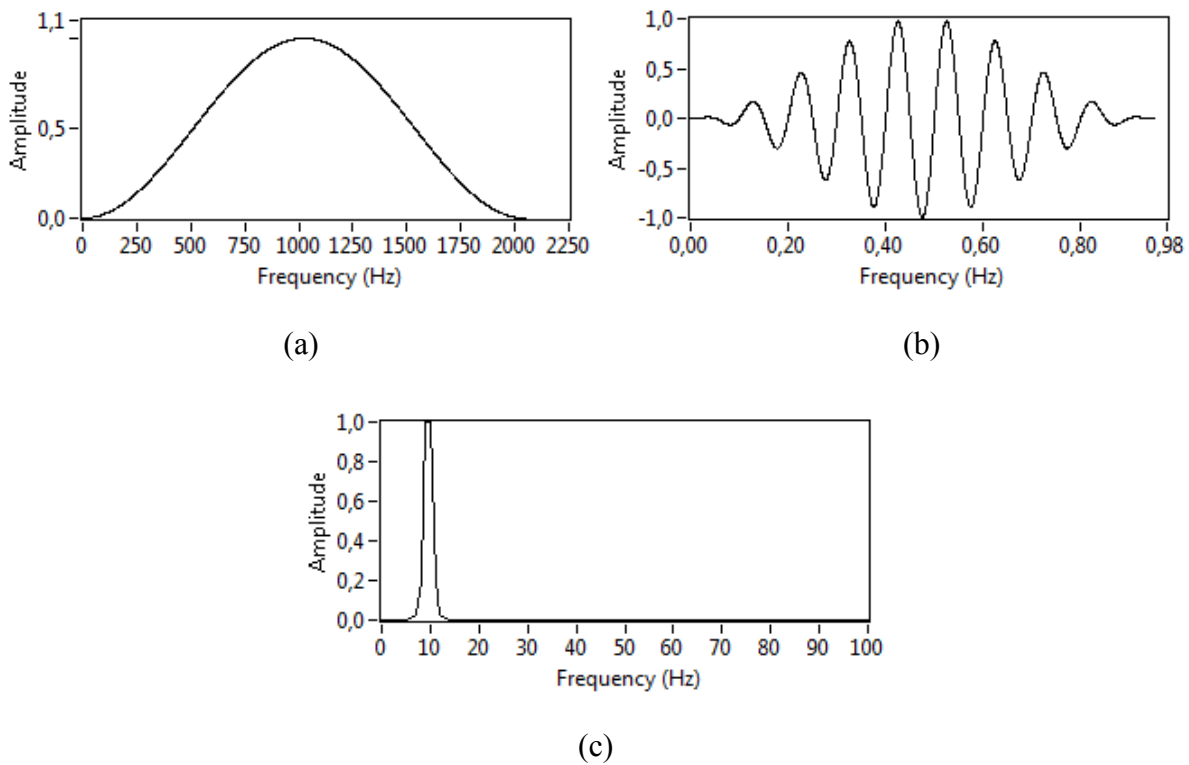


Figure 3.9 Applying window function to reduce spectral leakage of non-periodic signal: (a) Hanning window, (b) windowed non-periodic sine wave (Figure 2.22 (b)), (c) frequency spectral of the signal in (b) with reduced leakage.

Window	Recommended signal type	Frequency resolution	Spectral leakage	Amplitude accuracy
Boxcar	Transient, Synchronous sampling	Best	Poor	Poor
Hanning	Random	Good	Good	Fair
Hamming	Random	Good	Good	Good
Gaussian	Random	Good	Good	Good
Kaiser-Bessel	Random	Fair	Good	Good
Flat top	Sinusoids	Poor	Good	Best

Table 3.1 Summarized commonly used window function for FFT.

### 3.3.4 Short-Time Fourier Transform (STFT)

FFT evaluates the average frequency spectral within a signal. When calculating the FFT of a GPR signal, the high-level spectral component of direct wave can obscure the nearby low-level spectral component of reflected wave. Due to attenuation and scattering effects occurring during signal propagation, the spectrum of GPR signal varies with the time axis. The use of Fourier transform to evaluate the average frequency content is, therefore, inadequate. A Short-time Fourier transform (STFT) is then commonly used to provide simultaneous time and frequency information. The STFT is obtained by applying a fixed-sized, sliding window to the input signal. For each time location where the window is centered, a Fourier transform is calculated, resulting in a representation of a signal in both time and frequency domain. Mathematically, it is defined as:

$$STFT(\tau, f) = \int_{-\infty}^{\infty} x(t)w(\tau - t) \cdot \exp(-i \cdot 2\pi ft) dt \quad (3.24)$$

where  $w(\tau - t)$  is the window function centered at time  $t$ , commonly a truncated Gaussian window or a Hanning window.

One shortcoming of STFT is that it has a fixed resolution. The window length affects the resolution of the STFT. A narrow window results in a higher time resolution but a lower frequency resolution, and vice versa. The window length should be narrow enough to ensure good localization in the time domain and wide enough to avoid significant spectral leakage [45]. For using STFT to analyze GPR signal, Lai et. al. suggest using Hanning window, with a window length equal to eight times time taken from the first peak to the first valley (or 1/2 wavelength) in the direct wave.

### 3.3.5 S-Transform

During the propagation in subsurface materials, GPR signal attenuates. Especially for the dispersive material, the signal may contain reflected waves of different wavelength. Since the STFT employs an invariant window, one cannot find an appropriate window width for analyzing a GPR signal through the entire trace. To overcome this weakness, a relatively new technique called S-transform has been used to analyze GPR signals. The S-transform was first introduced by Stockwell in 1996 [46]. It can be derived from the STFT by using a variable, frequency-dependent window instead of a fixed-size window. The standard S-transform of a signal  $x(t)$  is given as follow:

$$S(\tau, f) = \int_{-\infty}^{\infty} x(t)w(\tau - t, f) \cdot \exp(-i \cdot 2\pi ft) dt, \quad (3.25)$$

where  $w$  is given as a scalable truncated Gaussian function:

$$w(\tau - t, \sigma) = \frac{\sigma}{\sqrt{2\pi}} \exp\left(-\frac{\sigma^2(t - \tau)^2}{2}\right), \quad (3.26)$$

where  $\sigma$  is a coefficient controlling the width of the window function as an proportion to the local frequency:

$$\sigma = |f|. \quad (3.27)$$

The window width defined by Eq. 3.26 and 3.27 varies with frequency which results in a multi-resolution of S-transform: high-frequency resolution at high frequencies and high time resolution at low frequencies.

The S-transform can be simplified and calculated by the inverse Fourier transform:

$$S(\tau, f) = \int_{-\infty}^{\infty} X(v + f) \cdot W(v) \cdot \exp(j \cdot 2\pi vt) dv = \text{IFFT}(X(v + f) \cdot W(v)), \quad (3.28)$$

in which  $W$  is the Fourier transform of the window  $w$ .

### 3.3.6 Image registration technique

Image registration is a process of aligning two images acquired by identical/different sensors, at different times or from different viewpoint. It is widely used for medical image processing to align the images from different medical image studies, such as Computerized Topography (CT), Magnetic Resonance Imaging (MRI), to the same spatial location before they can be integrated and visualized. In this study, this method is employed to align the GPR images/datasets measured at different times, with different antennas and measure parameters (sampling frequency, grid, spatial sampling interval, etc.).

To register images, one needs to determine geometric transformation that aligns images with respect to the reference image. For GPR images obtained from area scans, the deformations are mainly: rigid translation, rigid rotation and scaling (Figure 3.10). Many strategies have been proposed and implemented for the image registration based on either the geometrical features (point-like anatomic features or surfaces) or intensity similarity measures (cross correlation, squared intensity differences or mutual information). In this thesis, a mutual information-based image automatic registration method is employed.

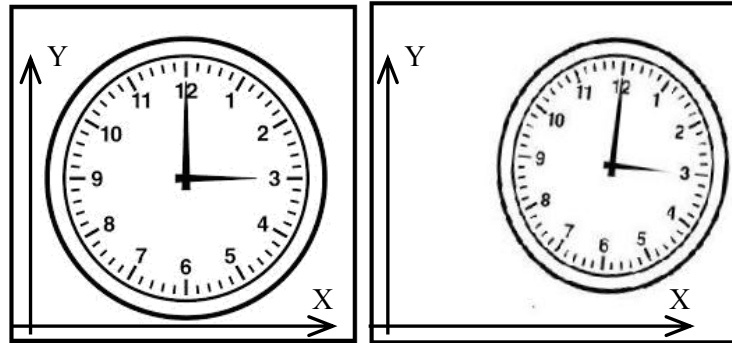


Figure 3.10 Deformation of image including: rigid translation, rigid rotation and scaling.

Mutual information was proposed by Viola and Wells in 1996 and is now accepted as one of the most accurate and robust retrospective registration measures. It is a histogram-based measure which evaluates the statistical dependence (association) between two image intensity distributions.

An image  $A$  can be taken as a matrix with the elements that are its intensities,  $a$ . According to communication (information) theory, the uncertainty of the random variable  $a$  ( $a \in A$ ) with a probability mass function  $p(a)$  can be measured by its entropy. In this study, the Shannon entropy measure is chosen, which is defined as:

$$H(A) = -\sum_x p(a) \log_2 p(a)$$

Given with two images  $A$  and  $B$ , the definition of the mutual information  $MI(A,B)$  is:

$$MI(A,B) = H(A) + H(B) - H(A,B) \quad (3.29)$$

where  $H(A,B)$  is their joint entropy:

$$H(A,B) = -\sum_{a,b} p(a,b) \log_2 p(a,b) \quad (3.30)$$

where  $p(a,b)$  is the joint distribution of random variables  $a$  and  $b$  ( $a \in A, b \in B$ ).

To use the MI measure for image registration, first, a part of image  $A$  is selected as a reference image,  $A_1$ . Second, scale and rotate  $A_1$ , with the scaling factors  $k_x$  in X-direction,  $k_y$  in Y-direction and rotation angle  $\theta$ . Third, search  $A_1'(k_x, k_y, \theta)$  in image  $B$  and find the best

align part  $B_l$  when the mutual information  $MI(A_l', B_l)$  is maximized. Then the parameters about image translation  $(\Delta x, \Delta y)$ , rigid rotation  $(\theta)$  and scaling  $(k_x, k_y)$  can be obtained.

### 3.4 Other NDT techniques used in this work

In order to achieve a better understanding of the sub-surface corrosion damage characteristic, the GPR measurements were carried out with a combination of several non-destructive or semi-destructive techniques [47]: half-cell potential, laser-induced breakdown spectroscopy and X-ray radiography.

#### 3.4.1 Half-Cell Potential (HCP)

Half-cell potential method is an electro-chemical method for corrosion measurement. It compares the electrochemical potential of embedded reinforcing steel with a standard reference half-cell placed on the concrete surface (Figure 3.11). In this work, Proceq's Canin+ Corrosion Analyzing Instrument connecting with a copper-copper sulphate half-cell is used. The measurements were carried out within grids. The results are presented in potential contour maps, which provide probability indications of active corrosion.

A criterion is given by ASTM:

- If potentials over an area are more positive than  $-200$  mV CSE, there is a greater than 90 % probability that no reinforcing steel corrosion is occurring in that area at the time of measurement.
- If potentials over an area are in the range of  $-200$  to  $-350$  mV CSE, corrosion activity of the reinforcing steel in that area is uncertain.
- If potentials over an area are more negative than  $-350$  mV CSE, there is a greater than 90 % probability that reinforcing steel corrosion is occurring in that area at the time of measurement.

In combination with the information about concrete cover depth and resistivity measurements, HCP provides an indication of the likelihood of active corrosion. In the area where HCP or measurements indicate that corrosion has initiated, resistivity test is carried out. Low resistivity ( $<10$  k $\Omega$ .cm) indicates that the rate of corrosion is likely to be high; low resistivity in the presence of chloride ions are the conditions needed for localized corrosion

which leads to pitting of the steel. Conversely, high resistivity indicates a low rate of general corrosion.

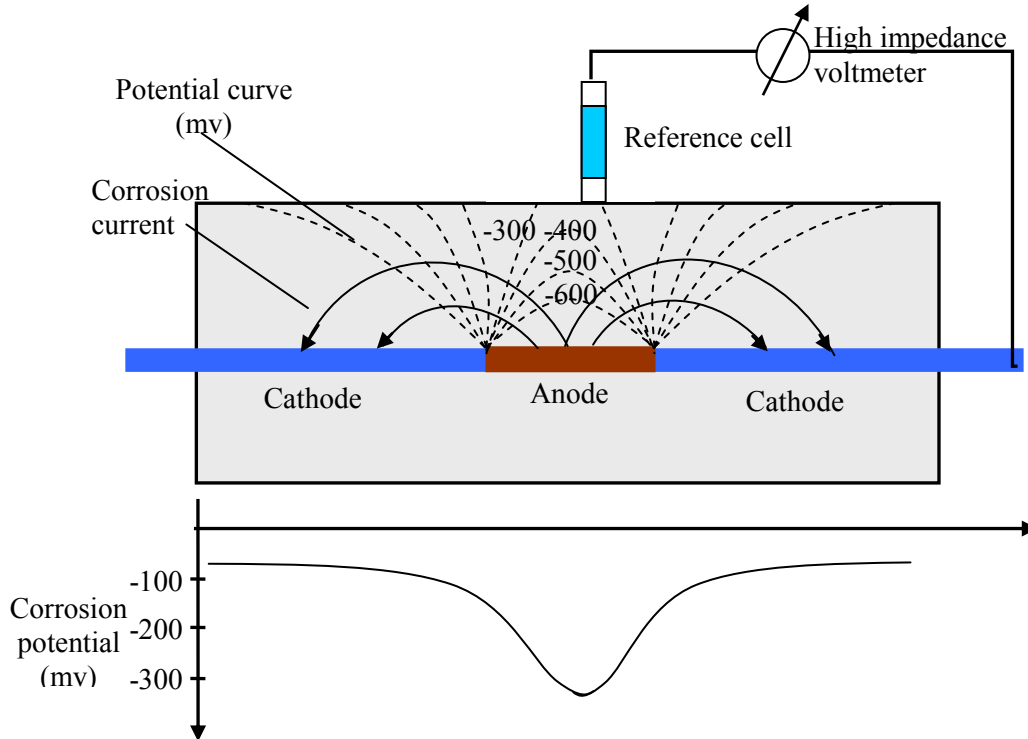


Figure 3.11 Principle of half-cell potential measurement.

### 3.4.2 Laser-Induced Breakdown Spectroscopy (LIBS)

LIBS was employed in this study to analysis the chloride distribution in the specimens and verify the result of GPR measurement. LIBS is a method used for the element analysis on the surface of solids, liquids or gases. In civil engineering, it is mainly used for the testing of building materials like concrete and mortar. The LIBS set-up used in BAM is shown in Figure 3.12 [14]. A highly energetic ( $> 2 \text{ GW/cm}^2$ ) laser pulse is transduced by a pulsed laser generator (Nd-YAG Laser) and focused on the samples to excite and atomize the material on the surface of the sample and form a plasma plume. During the relaxation process, elements emit light with specific wavelength. The light is guided through an optical fiber to the detection unit. The light intensity is measured as a function of the wavelength, see Figure 3.13. In this study, LIBS was employed to investigate the penetration of chloride in concrete which is detected with a wavelength of 837.6 nm.

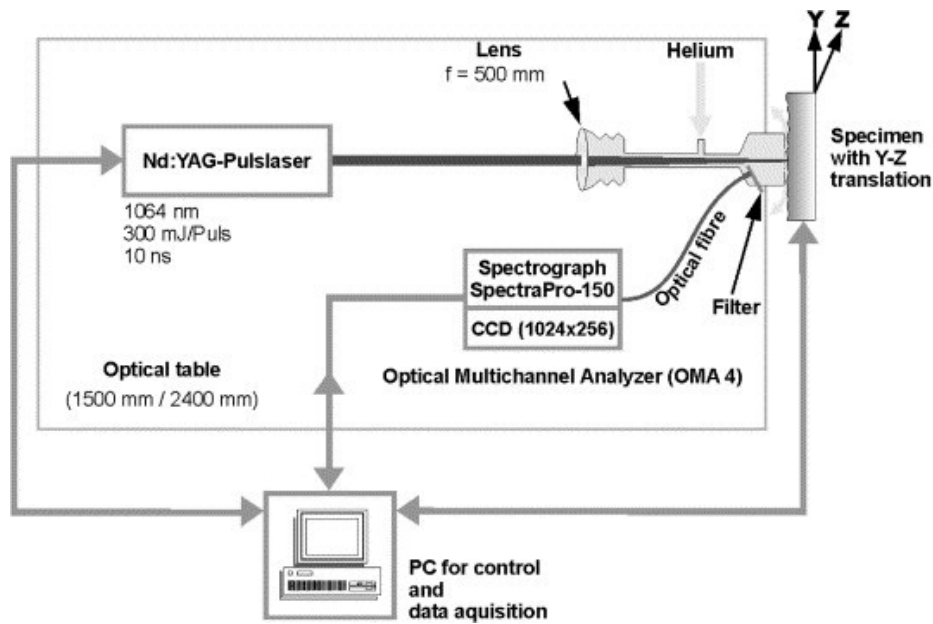


Figure 3.12 LIBS experiment setup [14].

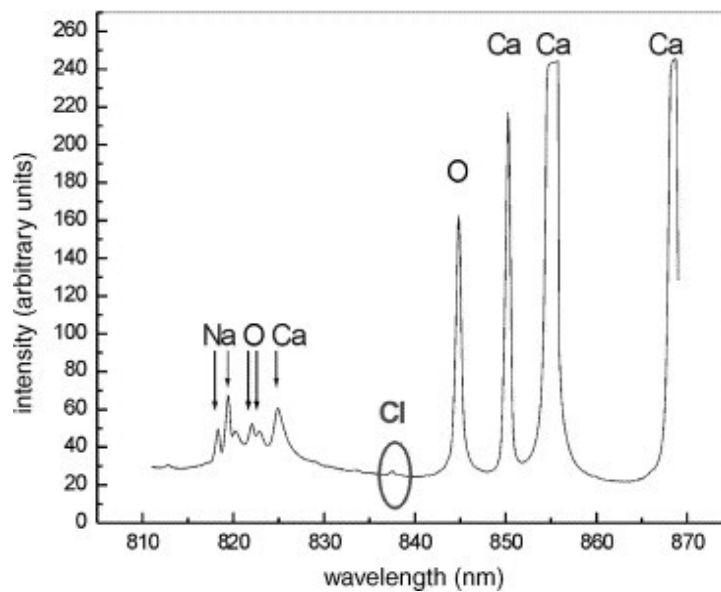


Figure 3.13 Typical LIBS spectrum measured on cement mortar, in which chloride is detected with a wavelength of 837.6 nm [14].

To prepare a flat test surface, concrete cores are usually taken from the structures, and split into two parts. The element distributions in the test surface were obtained by scanning the whole surface. The measured intensity values were normalized with the background value. The areas marked in black represent low ratios, i.e. aggregates; the areas marked in red represent the distribution of chloride. The result of LIBS usually has to be calibrated by using an internal



or added standard to evaluate the element concentration. The average intensity was calculated for each horizontal scan line to obtain a depth profile plot.



## Chapter 4 Accelerated Corrosion Experiment and GPR-Based Periodic Monitoring

### 4.1 Accelerated corrosion by means of impressing current technique

Protected by the alkaline environment in concrete, reinforced corrosion is a slow process which takes a long time for the initiation and progress even in the case of aggressive environment exposure. For a laboratory experiment, it is difficult to achieve a significant degree of corrosion in a short period in natural condition. To accelerate the corrosion process, various techniques for inducing accelerated corrosion of reinforcement in concrete have been proposed by researchers: Impression of direct current through the reinforcements which is also called Galvanostatic method;

- Exposure of specimen to high-humidity environment via wet-dry cycling, spraying or pounding the specimens in a chloride solution.
- Contaminate of specimen with chloride added directly into the concrete mixture, immerse or spray with chloride solution.

In this study, in order to induce **general corrosion** in the specimens, the impress current technique is used. The specimens were contaminated with chloride (immersion and/or add into concrete mixture) and applied direct current (D.C) between the reinforcing steel (anode) and a cathode. Figure 4.1 shows an example of accelerating corrosion setup by impressing current. This setup is used in the first experiment in this thesis (See Chapter 4). A pair of reinforcing bars is used as anode and cathode bar, respectively.

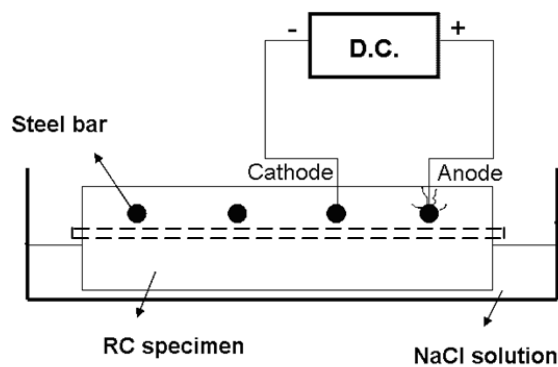


Figure 4.1 An example of accelerating corrosion setup by impressing direct current

By impressing current technique, the corrosion initiation period for the anode bar can be reduced from years to days, and the amount of steel loss can be determined theoretically with Faraday's law of electro-chemical equivalence:

$$\Delta m = MI t / zF, \quad (11)$$

where  $\Delta m$  is the mass of steel consumed;  $M$  is the atomic weight of steel;  $t$  is the duration of time in seconds;  $z$  is the ionic charge; and  $F$  is Faraday's constant ( $F = 9.65 \times 10^4 \text{ amp} \cdot \text{s}$ )

The induced degree of corrosion can be estimated by:

$$\gamma = \frac{\Delta m}{m} \times 100\% \quad (12)$$

where  $m$  is the mass of the non-corroded rebar.

For GPR measurements, as introduced in Chapter 2, the GPR signal is very sensitive to moisture, which increases the attenuation of signal. Thus, during the experiment, the moisture of the specimens has to be controlled under a constant condition; also, a reference rebar or reference specimen should be prepared and exposure to the same condition as test specimen to monitor the influence of moisture and chloride.

It is clear that the design of accelerated reinforcement corrosion experiment intends to induce not only a certain degree of corrosion in a required time frame, but also to induce corrosion which is consistent with that which actually happens in the field. Using a high current intensity can achieve the desired corrosion degree in a short period. But it doesn't allow the generated rust to penetrate into the concrete pores and cracks gradually, resulting in a large concentration of the rust around the rebar and a higher expansion stress in the surrounding concrete. Most previous studies have used current densities that are from 3 to 100 times the maximum current densities measured from field experiments [48].

To investigate the GPR response to the **pitting corrosion**, a specimen built in July 2002 was used. To initiate the pitting corrosion, in 2004, some initialization spots were installed by drilling holes in the cover concrete and filling with chloride solution (Chapter 5). The specimen was exposed to an environment comparable to on-site bridge decks. The long-term corrosion process was periodically monitored with GPR and HCP.

## 4.2 GPR system description

In this research, the impulse GPR system SIR-20 and SIR-3000 manufactured by Geophysical Survey Systems, Inc. (GSSI) were used. SIR-20 is a powerful multi-channel data acquisition system combined with a rugged notebook PC. SIR-3000 is a portable system designed for industrial application with single channel. Some of the specifications of these two systems are summarized in Table 4.1.

System	SIR-20			SIR-3000	
Number of channels	2			1	
Antenna	Compatible with all GSSI antennas				
Max scan rate (sans/Sec)	Samples/scan	1 channel	2 channels	Samples/scan	1 channel
	256	265	135	256	220
	512	153	78	512	120
Samples per scan	256, 512, 2014, 2048, 4096, 8192				
Operating mode	Free run, survey wheel, point mode				
Time range	0-8000 ns full scale, user-selectable				
Data format	RADAN (.dzt)				
Gain	Manual adjustment, 1-8 gain points (-20 to +100 dB)			Manual or automatic, 1-5 gain points (-20 to +80 dB)	
Dimension	446x395x174 mm			315x220x105 mm	
Weight	12.2 kg			4.1 kg	

Table 4.1 System specifications of SIR-20 and SIR-3000.

The ground-coupled antennas from GSSI with the center frequency 1.5 GHz, 2.0 GHz and 2.6 GHz were used in this research. The single-bowtie antenna operates as transmitter and receiver.

## 4.3 Data acquisition

GPR data were collected within grids. The grid size was selected for around 2 to 10 cm, according to the lateral resolution of the antenna (section 3.1.3). The lateral sampling interval was selected as 400 scan/m. For each A-scan, the time window was set at 5 ns with a sampling frequency of 512 scan/5ns.

#### 4.4 Data processing

The signal processing flow used in this research is depicted in Figure 4.2, which is classified into three parts in this work: pre-processing, attribute study and 2D visualization. The signal pre-processing steps are applied by using the commercial software ReflexW, including: trace editing, remove header gain, band pass filtering, D.C removal, and dewow filtering. The basic descriptions of these steps can be found in section 3.3.

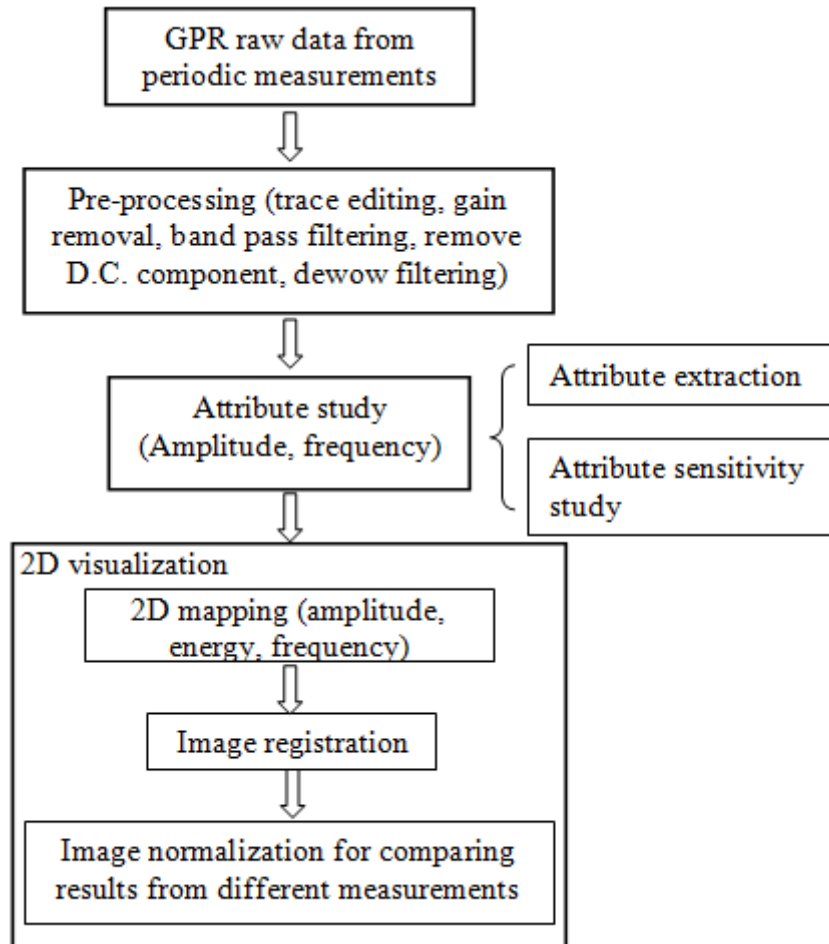


Figure 4.2 Signal processing flow used in this work.

##### 4.4.1 Attribute study

After pre-processing, the signals were processed to extract the signal attributes signal amplitude and peak frequency of the direct wave and the reflected wave of the rebar. With the understanding of corrosion damage mechanism and physical properties of electromagnetic wave, the sensitivities of extracted attributes to reinforcement corrosion and moisture variation were investigated.

- **Peak-to-peak amplitude**

To investigate the change of signal amplitude, several signal processing toolkits were developed based on Labview. In a given B-scan signal, the hyperbolas representing the location of rebars are automatically located first; then the A-scan signal with reflected amplitude was selected to estimate its peak-to-peak amplitude of reflected wave (Figure 4.3).

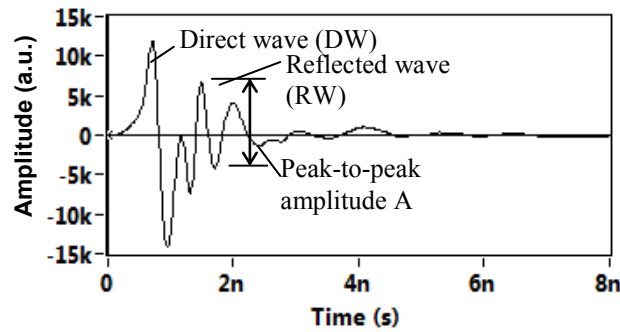


Figure 4.3 Estimation of the peak-to-peak amplitude of an given time domain signal.

- **Signal frequency**

To estimate the peak frequency of direct wave and reflected wave, the joint time-frequency analysis was carried out to obtain the time-frequency representation of the selected A-scan. Figure 4.4 (a) shows a time domain A-scan, measured in the second experiment (section 5.2). The rebar is embedded 4.5 cm deep inside the specimen, represented by the second positive peak in the waveform. Its normalized Power Spectrum Density (PSD) calculated by using FFT is depicted in Figure 4.4b with a first peak frequency 0.83 GHz. With the PSD, one cannot estimate the frequency spectrum of DW and RW separately.

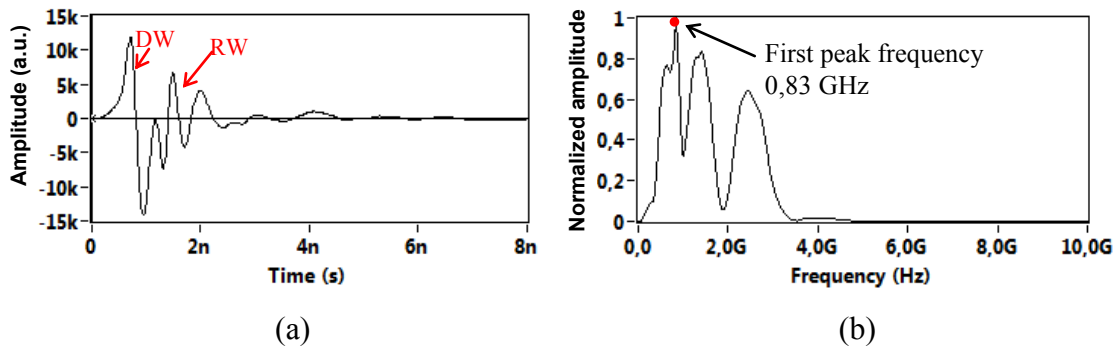


Figure 4.4 (a) Time domain A-scan signal with an RW reflected by a rebar embedded in a depth of 4.5 cm inside the specimen, (b) PSD of the signal (a).

To obtain the frequency spectrum of DW and RW, first the time-frequency spectrum of the A-scan signal has to be calculated by using the time-frequency transform. Then, the frequency spectrum of the DW and RW can be obtained as a cross-section of the time-frequency spectrum at the arrival time of DW and RW on the time axis. Figure 4.5 (a) shows the time-frequency spectrogram of the signal shown in Figure 4.4 calculated by using STFT. In order to preserve sufficient time resolution, the Hamming window was applied with width equal to six times the time taken from the first peak to the first valley in the DW. The STFT spectrogram is able to detect the basic DW component and the overlapping of DW and RW. The frequency spectra of the DW and RW are shown in Figure 4.5 (b) and (c) with the peak frequency 1.3 and 2.3 GHz, respectively.

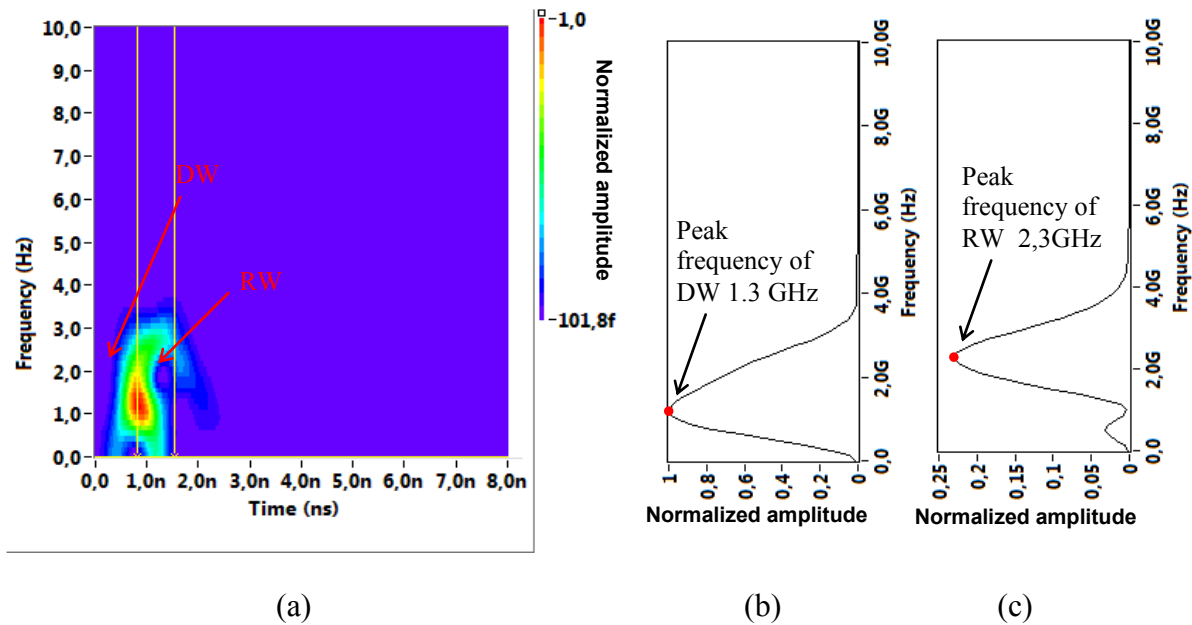


Figure 4.5 (a) time-frequency spectrum of the signal shown in Figure 4.4 calculated by using STFT with a Hamming window, window size 1.5 ns, (b) frequency spectrum of DW, (c) frequency spectrum of RW.



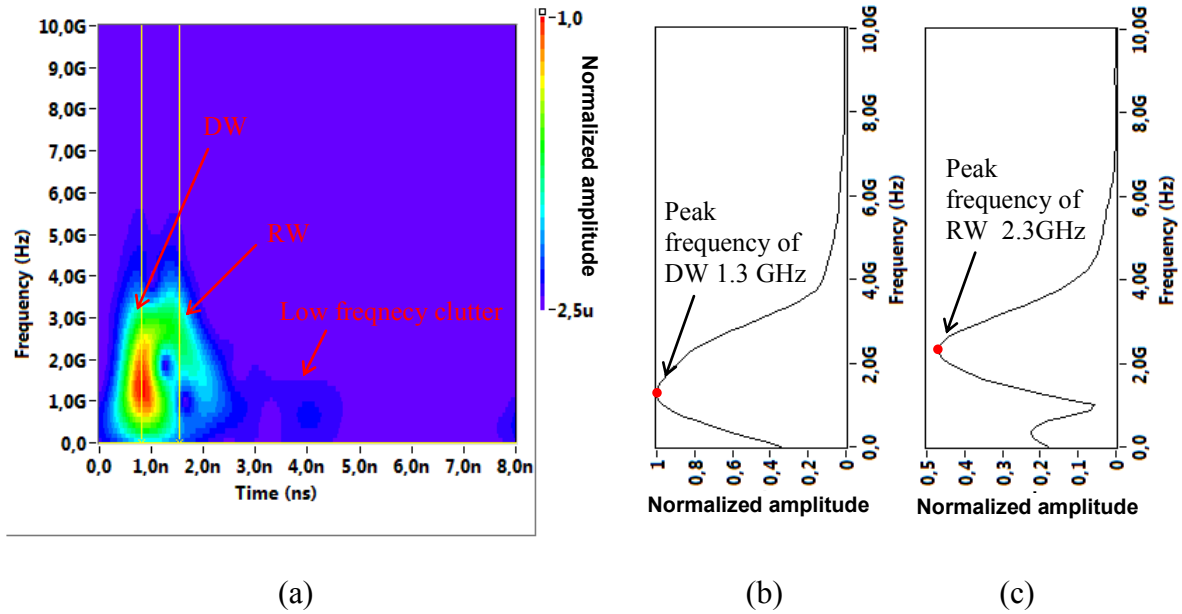


Figure 4.6 (a) time-frequency spectrum of the signal shown in Figure 4.4 calculated by using general S-transform, (b) frequency spectrum of DW, (c) frequency spectrum of RW.

Applying S-transform with moving scalable Gaussian window provides high-frequency resolution at low frequencies. Figure 4.6 (a) shows the time-frequency representation with the basic component of DW, the overlapping of DW and RW and the low-frequency component at the tail of the signal. The frequency spectra of the DW and RW are shown in Figure 4.6 (b) and (c) with the peak frequency 1.3 and 2.3 GHz, respectively, which are the same as those obtained by STFT. However, by comparing Figure 4.5(c) and Figure 4.6(c), the frequency spectrum of RW obtained by S-transform has a higher amplitude than that of STFT.

Figure 4.7 shows a time domain A-scan and its PSD, for which the rebar is embedded 9 cm deep inside the specimen, represented by the third positive peak in the waveform. Comparing Figure 4.8 with Figure 4.9, STFT and ST methods can obtain the similar peak frequency of DW and RW. However, comparing with STFT, S-transform has an improvement of tracking the attenuation of GPR signal, by providing a clearer detection of the weak RW component.

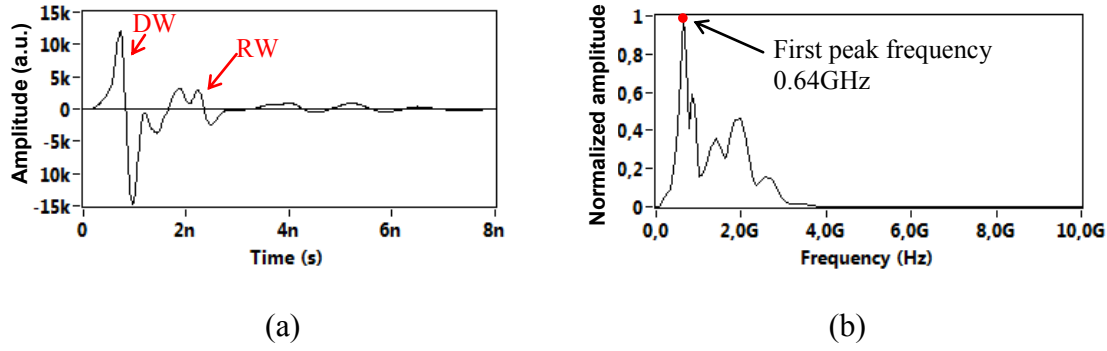


Figure 4.7 (a) Time domain A-scan signal with an RW reflected by a rebar embedded at 9 cm deep inside the specimen, (b) PSD of the signal (a).

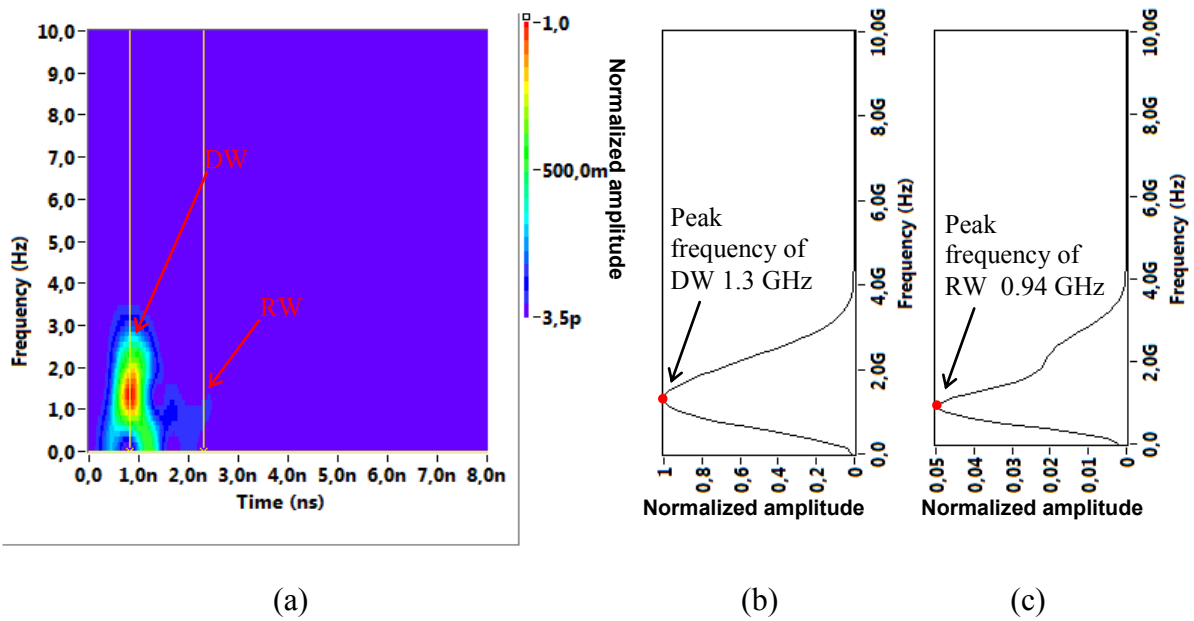


Figure 4.8 (a) time-frequency spectrum of the signal shown in Figure 4.7 calculated by using STFT with a Hamming window, window size 1.5 ns, (b) frequency spectrum of DW, (c) frequency spectrum of RW.

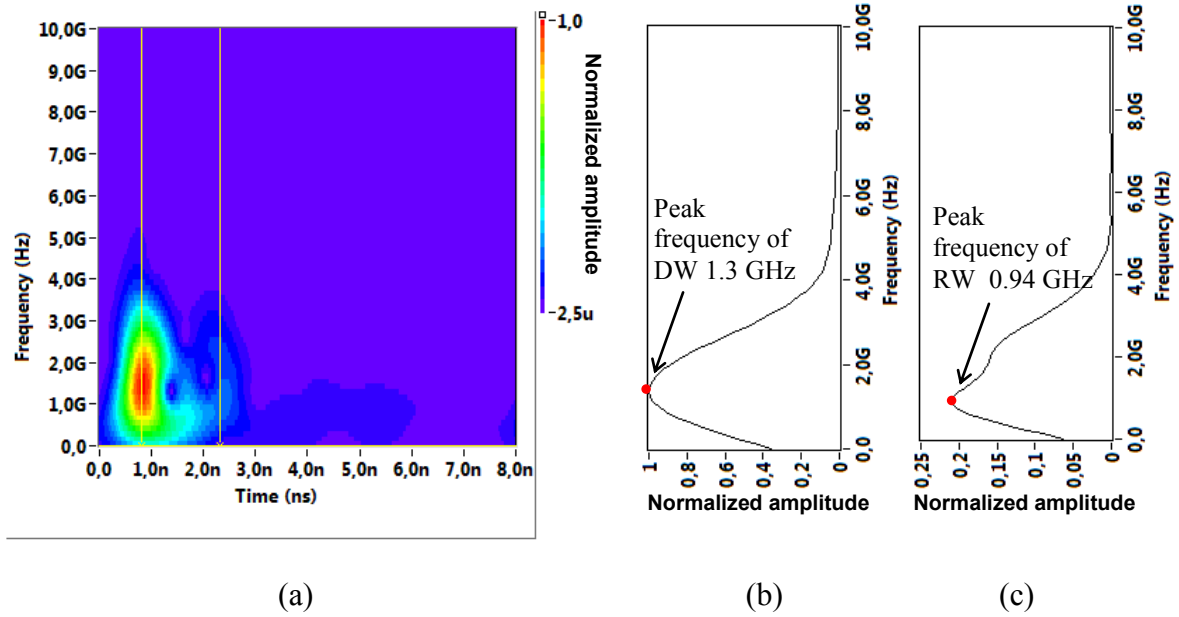
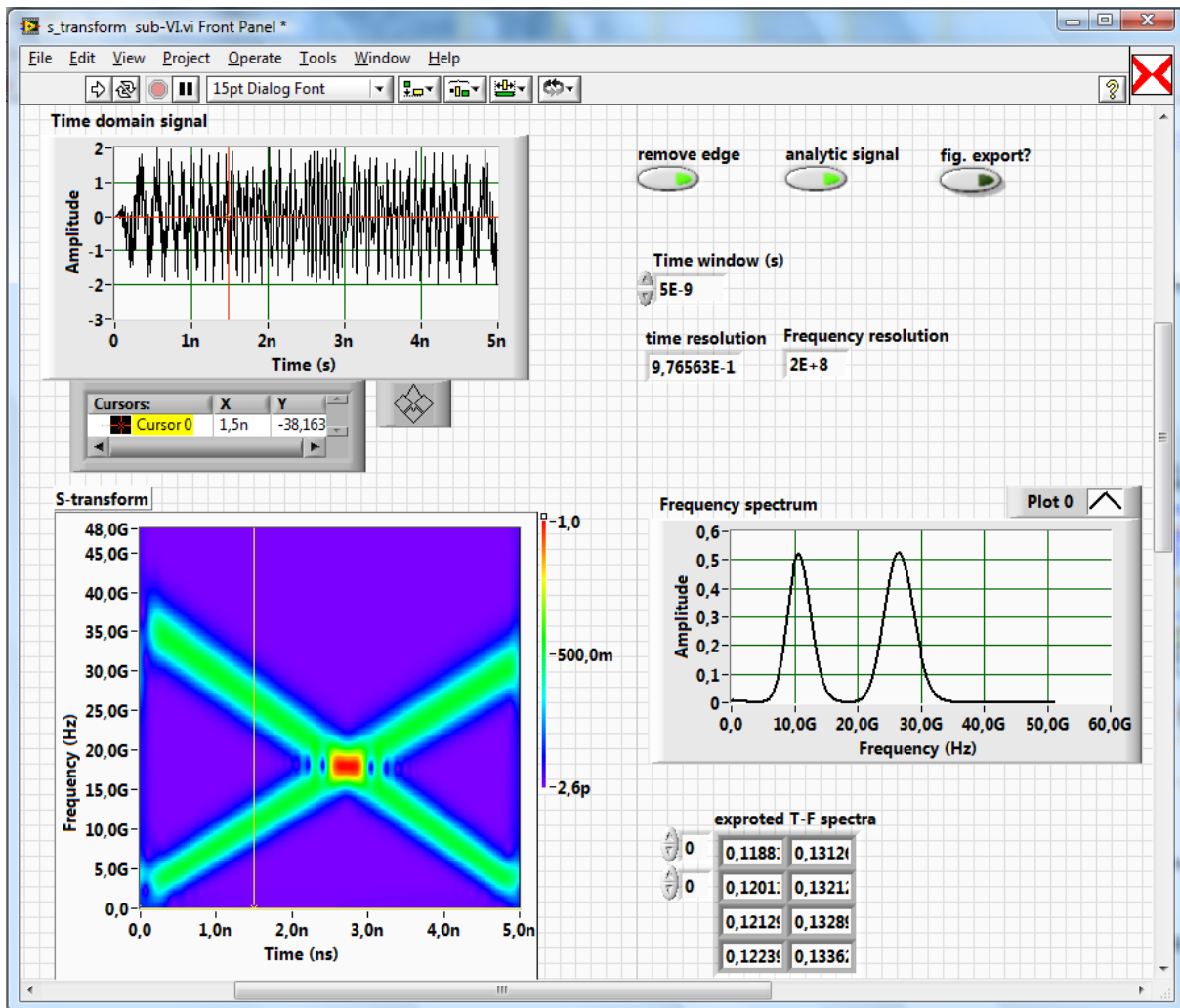
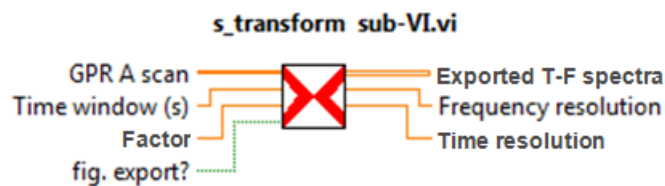


Figure 4.9 (a) time-frequency spectrum of the signal shown in Figure 4.7 calculated by using general S-transform, (b) frequency spectrum of DW, (c) frequency spectrum of RW.

In this work, S-transform was adopted to analyze the frequency variation during the experiments. A toolkit was developed (Figure 4.10) based on Labview to implement the calculation by using fast Fourier transform and inverse Fourier transform (see section 3.3.5). This toolkit can be used as a sub-VI function for further processing by being given several inputs, including: time domain signal, time duration of the signal and k factor. It provides a 2D array of the time-frequency spectra and its time and frequency resolution.



(a)



(b)

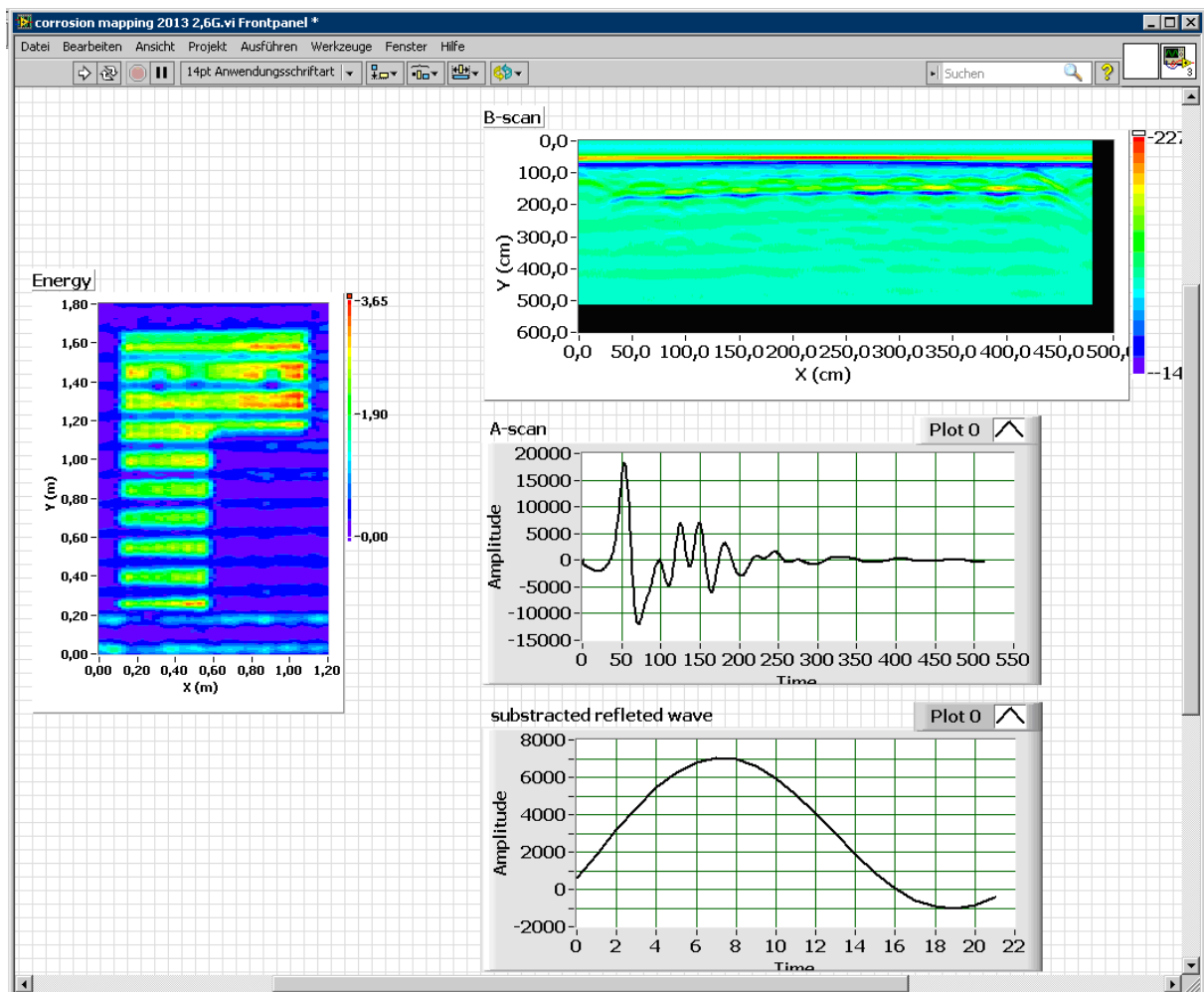
Figure 4.10 Developed S-transform toolkit: (a) user interface; (b) input and output of the toolkit.

#### 4.4.2 2D visualization by mapping the selected attributes

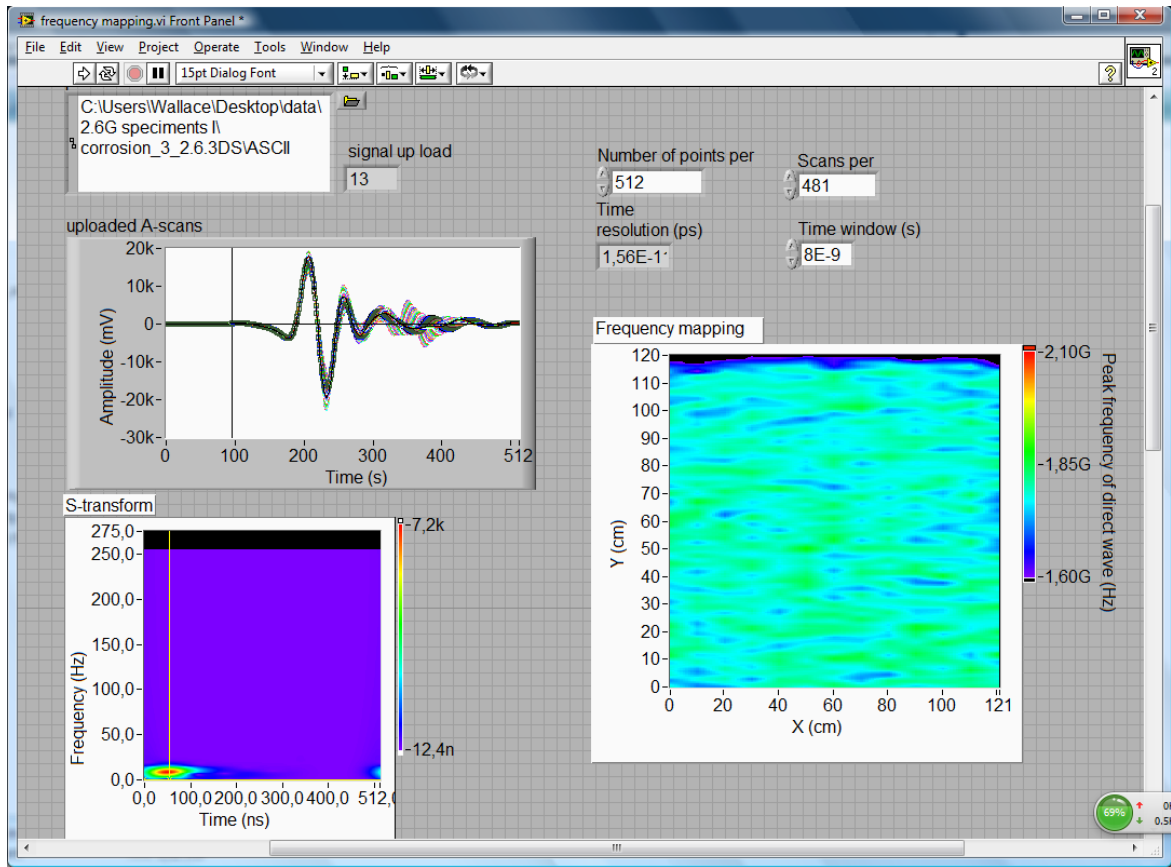
Usually, in the GPR archaeological survey, the extracted attributes were calculated within a window sliding along the time axis of A-scan signals and represented as a 3D data cube or

time slices [43, 49]. In this research, the subsurface targets, reinforcements, are relatively simple and embedded in similar depth in concrete. Thus, the signal attributes, amplitude and frequency, can be calculated only for DW and RW and mapped in an area.

Labview toolkits (Figure 4.11) were developed for mapping the selected attributes. The changes of RW amplitude were enhanced by calculating signal energy. The reflected wavelets were automatically subtracted for each A-scan. Then, signal energy was calculated (see section 3.3.2) and mapped in 2D intensity plot with the toolkit shown in Figure 4.11 (a). Peak frequency of DW was selected as an attribute for evaluating the signal dispersion related with chloride contamination, which will be explained in the next chapter. The peak frequency of DW was mapped with the toolkit shown in Figure 4.11 (b).



(a)



(b)

Figure 4.11 Developed Labview toolkits for GPR attributes mapping: (a) energy mapping (b) frequency mapping.

#### 4.4.3 Image registration and normalization

In order to compare the results measured at different time and/or with different measure parameters, a novel method for the image intensity normalization is proposed, which consists of two parts: automatic image registration and intensity normalization. Image intensity-based mutual information (section 2.5.3) is used as the similarity measure for image registration. The proposed algorithmic steps of image registration and intensity normalization are as follows:

- Take the result from the baseline measurement as a baseline image, 'A', and select an area, 'a'

- Interpolate the subject image, 'B', (the result from the motoring measurement) to obtain a new image ('B<sub>1</sub>') within the data grid of baseline image
- Apply a sliding 2D window with the same size as 'a' to select an area 'b' from B<sub>1</sub>
- Rotate 'b' and generate new image with interpolation within the baseline data grid
- Move the window and calculate the MI similarity measure between the baseline image 'a' and the transformed subject image 'b' for every transformation step (rigid translation and rotation)
- Read the transformation matrix which results in the maximum MI and apply it on subject image B<sub>1</sub> to obtain the aligned image 'b'
- Plot the intensity relationship between of the aligned images 'a' and 'b'
- Obtain the intensity normalization function  $b=f(a)$  by finding the best fitting curve of the joint intensity histogram
- Use the normalization function to normalize the intensity of subject image (B<sub>1</sub>):  $B_2=f(B_1)$ .

The flowchart in Figure 4.12 gives an overview of these steps. A Labview toolkit was developed to implement this procedure as shown in Figure 4.13. To use the toolkit, first, the users are asked to crop a reference area from the baseline image. For corrosion monitoring, the non-corroded area is considered to be stable and can be taken as a reference area. The way to determine non-corroded area will be described in Section 5.3.4. To save the computational time, a starting point can be selected in the subject image 'B', close to the lower left corner of the selected reference area 'a'. The returned computational results include:

- position of the matched area within the subject image
- angle through which it has rotated to match the reference area
- intensity relationship of the aligned image, the fitted normalization function
- normalized subject image.

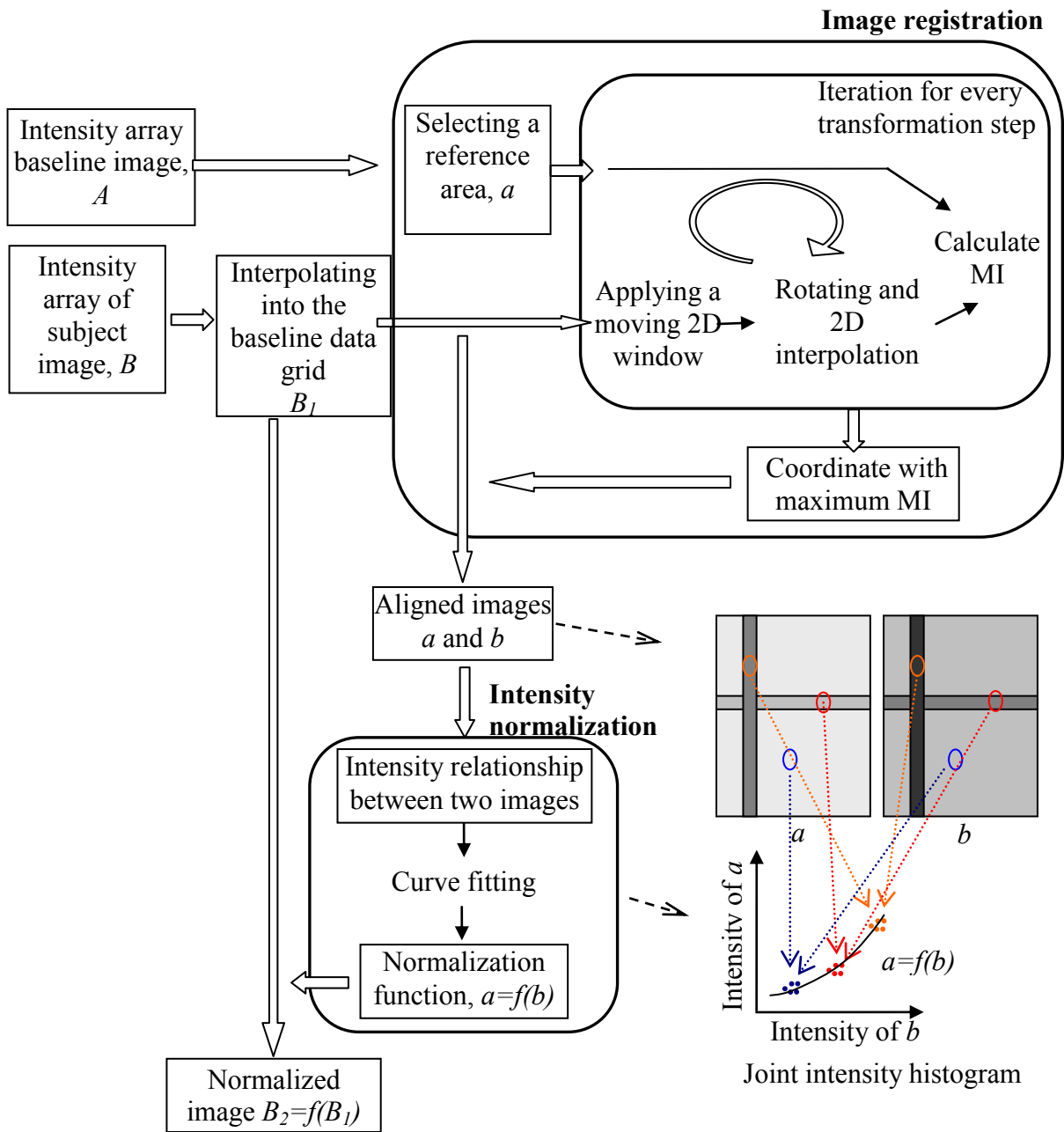


Figure 4.12 Flowchart for automatic image registration and intensity normalization.



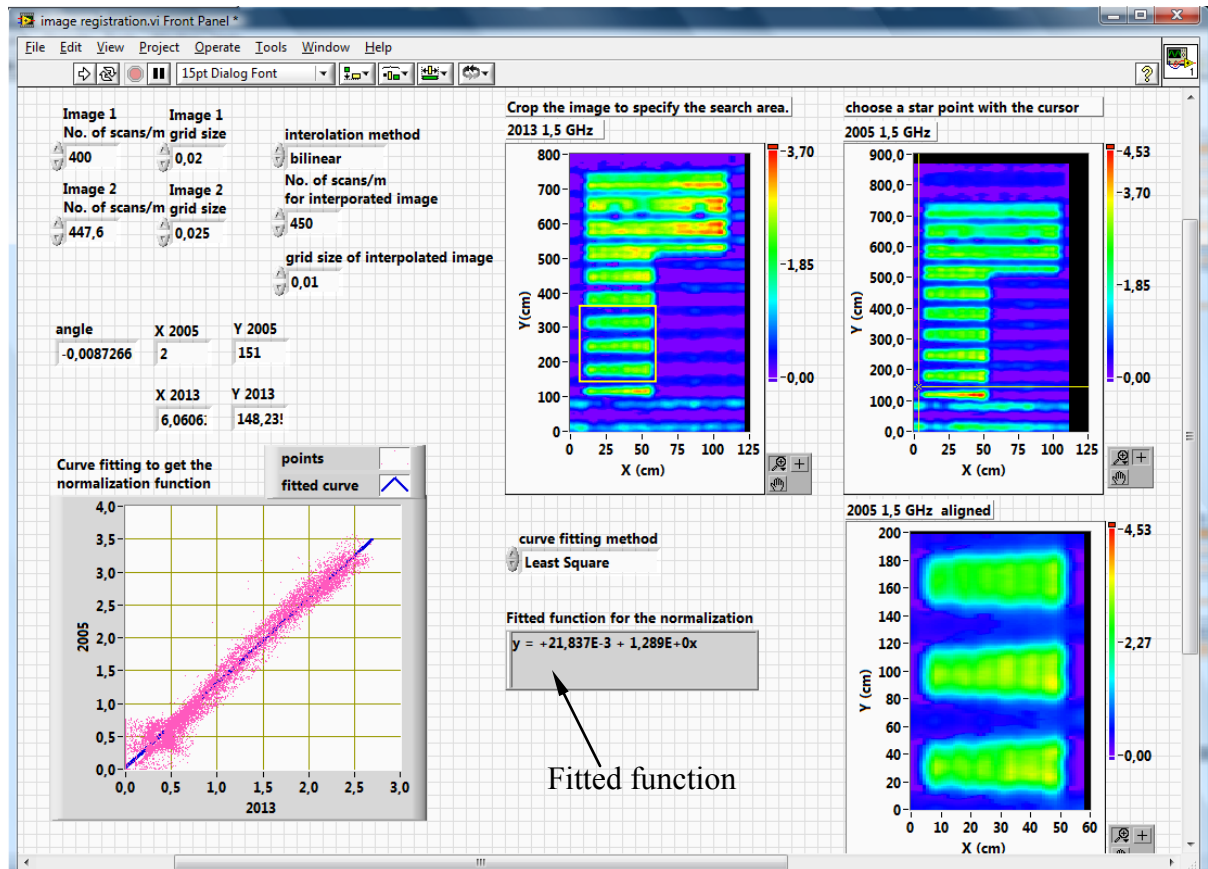


Figure 4.13 Developed Labview toolkit for GPR image registration and intensity normalization.



## Chapter 5 Experimental Work

### 5.1 Experiment 1

The aims of this experiment include:

- testing the feasibility of using GPR for corrosion detection/monitoring
- investigating the response of GPR signal to accelerated corrosion
- analyzing the capacity of GPR signal attributes, including amplitude, energy, peak frequency etc., for obtaining the information about reinforcement corrosion, chloride and moisture
- investigating the mechanism of GPR response to corrosion and chloride contraindication by combining the results of other NDT measurements (LIBS, US and HCP)

#### 5.1.1 Preparation of specimen

A reinforced concrete slab with a size of 150 cm×150 cm×30 cm was cast and sufficiently cured for 8 months before the first corrosion experiment was started. The drawing of the specimens and GPR measurement grid is shown in Figure 5.1. The slab was reinforced with two layers of perpendicular steel bars (diameter: 25 mm). These two layers are separated by a vertical distance (3 cm) to avoid short circuit during the accelerated corrosion. Ribbed steel bars were used except bar no. 3 in the upper layer of rebars, which was made of a stainless steel round bar and was used as a cathode in the experiments. The upper-layer steel bars were placed in the x-direction with a concrete cover of 7 cm. 7 cm cover depth is considered sufficient to adequately separate the wavelets of direct wave and reflected wave. The second layer steel bars were placed in the y-direction with a concrete cover of 12.5 cm. The concrete class C35/45 was selected. The mix proportion includes 285 kg/m<sup>3</sup> of cement, 170 kg/m<sup>3</sup> of water (with a water-to-cement ratio of 0.6), 1867 kg/m<sup>3</sup> of well-graded fine and coarse aggregate. The specimen was cured in the laboratory's ambient environment, where the temperature was around 20°C and relative humidity was around 50%.

### 5.1.2 Experiment procedure

The experiment was carried out in two setups:

In setup 1, in order to achieve similar chloride distribution as happened in an actual structure, the specimen was first immersed in a 5% sodium chloride solution for 5 days. Then, water level was reduced slightly below the lower layer steel bars. During the experiment the cover concrete became dry and the chlorides were transported to the concrete surface driven by capillary forces [50]. The water level dropped over time due to evaporation. In order to obtain unequal salt distribution on the slab, fresh water was added only on one side of the tank (Figure 5.2). So the salt concentration of the solution in this side is lower than the other side.

The induced corrosion process was started 2 days after reducing the water level. The corrosion process of rebars in concrete was accelerated by means of impressing direct current (D.C.) [51, 52]. Bar no.1 was connected to the positive terminal of a DC power source and bar no. 2 to the negative terminal, as shown in Figure 5.2. A constant 0.5 A direct current was applied between these two rebars, equal to a current intensity  $0.424 \text{ mA/cm}^2$ . The amount of induced steel mass loss on the anode bar due to corrosion can be calculated theoretically by using Eq. 3.1 and 3.2.

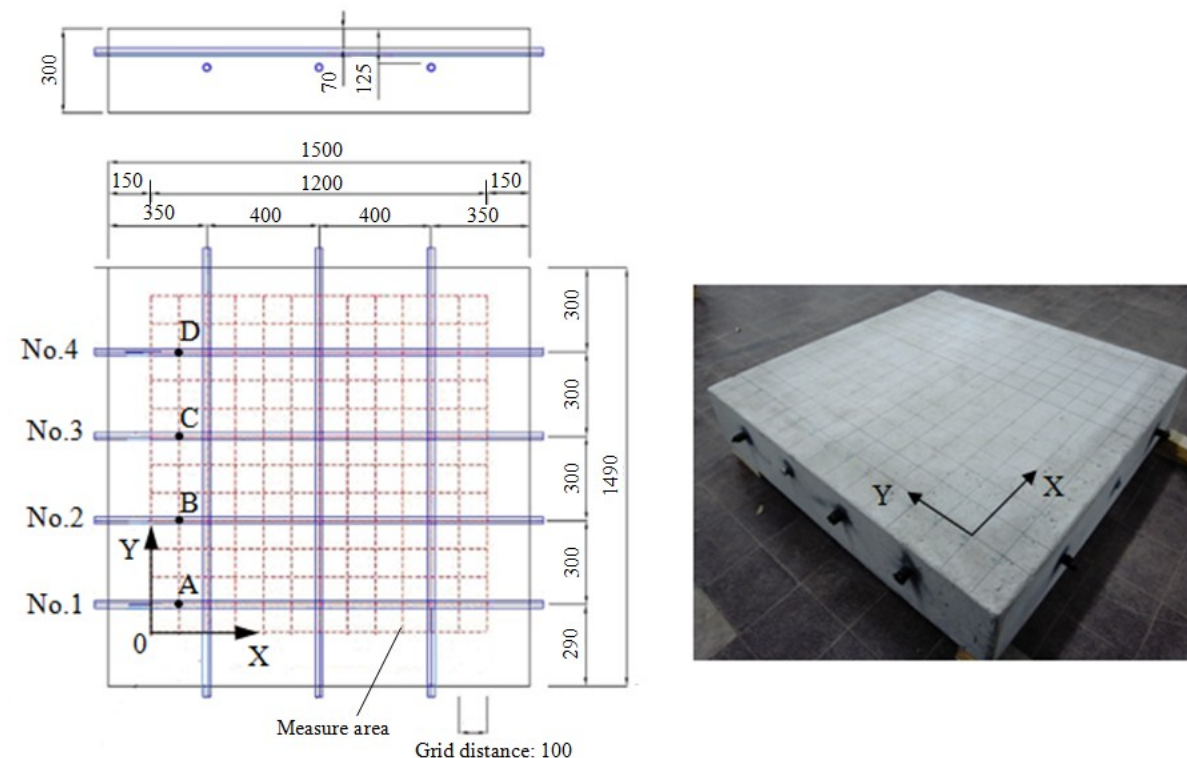


Figure 5.1 Drawing of the test specimen and the measurement grid (unit: mm).

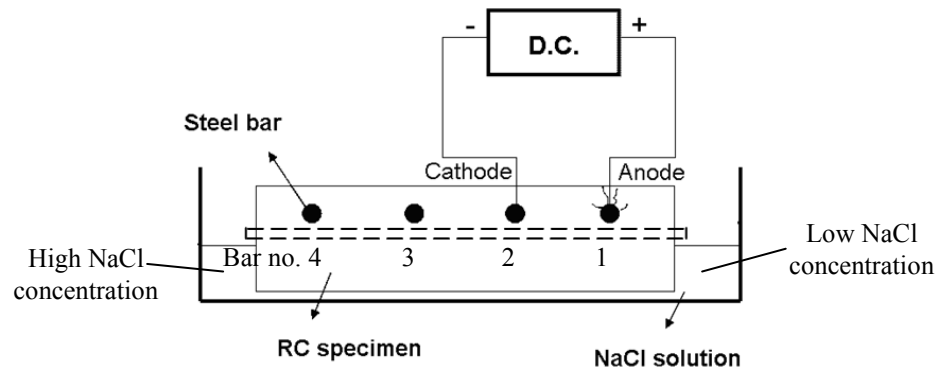


Figure 5.2 Set-up used in Setup1 for accelerating reinforcement corrosion.

The first GPR measurement was carried out before chloride contamination to determine the baseline data. After that, the second measurement was carried out before the accelerated corrosion was started. The further GPR measurements were carried out periodically to monitor the induced corrosion procedure. The experiment was stopped on the 50<sup>th</sup> day when the crack became wide open and continuous along the anode bar.

In setup 2, the accelerated corrosion process was carried out on the same specimen under dry conditions. The specimen was taken out from the water bath and stored in the lab for two months to obtain a rather stable low moisture content in the concrete. The steel bar no.3 and no.4 were selected as cathode and anode, respectively. Again, just like in Setup 1, a constant 0.5 A direct current was impressed between them. The impressed current was stopped after 14 days, when a wide-open crack appeared on the concrete surface. The GPR measurements were

carried out periodically (every 2 days) during this period. A comparison between setup 1 and 2 is reported in Table 5.1.

Parameters	Setup1	Setup2
Current density (mA/cm <sup>2</sup> )	0.242	0.24
Anode (Bar no.#)	1	4
Cathode (Bar no.#)	2	3
First crack was observed after	14 days	4 days
Longitudinal continuous crack appeared after	24 days	6 days
The crack became wide open and the experiment stopped on	Day 50	Day 15

Table 5.1 Comparison between setup 1 and 2

After the induced corrosion process, core samples were taken and split into two halves. Laser-induced breakdown spectroscopy (LIBS) was employed to obtain the information about the depth profile of the concrete ingress, which is used to validate the results from setup 2.

### 5.1.3 Results of GPR monitoring

GPR data was collected with GSSI 2.6 GHz antennas in perpendicular GPR traverses in both x- and y- direction (400 scans/m, 512 data points in 5 ns for each A-scan) with 10 cm grid size as shown in Figure 5.1 during the corrosion process. The collected GPR raw data were first pre-processed following the process shown in Figure 4.2.

#### 5.1.3.1 Setup 1

In this setup, cracks developed and propagated on the concrete surface above the anode bar. The first micro-cracks had been observed on the slab surface after impressing current for 14 days. After 24 days, the concrete surface was cracked above the anode bar over the whole concrete surface.

- **Changes of the waveforms recorded on anode and cathode**

A time domain A-scan signal is extracted at the vertex of the hyperbola in the B-scan (Figure 5.3) to investigate the change of GPR waveform of the cathode and anode bars. The DW and RW are presented by the first wavelets and the fourth wavelets, respectively.

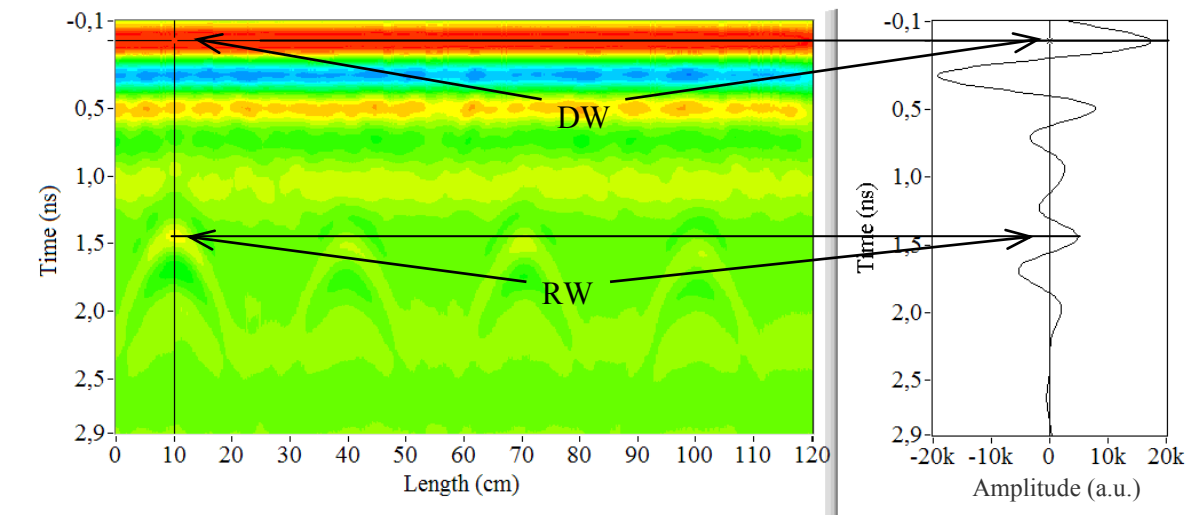


Figure 5.3 GPR B-scan showing the location of four rebars in the first layer and the position of DW and RW in the A-scan signal (amplitudes are specified in arbitrary units).

The change of time domain A-scans recorded on the cathode bar (point B in Figure 5.1) and anode bar (point A in Figure 5.1) in Setup 1 are shown in Figure 5.4 and Figure 5.5. It can be observed that the immersion in NaCl solution led to a decrease in the amplitude of the DW and the RW and a delay of the arriving time of the RW (from the peak of DW to the peak of RW). Then the direct current was applied to start the corrosion process. In the meantime, the cover concrete became dry and the chlorides in dissolved form were transported by capillary action through the concrete matrix. The moisture was drawn to the surface and evaporated, leaving the salt accumulated in the near surface pores. Since bar no.2 was connected to cathode and thus it was protected from being corroded, it could be considered a relatively stable reference. The RW acquired at the cathode bar was influenced only by the change of moisture and chloride content. In Figure 5.4, it is observed that, as the concrete got dry, the amplitude of DW and RW increased slightly and the travel time also decreased slightly. For the anode bar, in Figure 5.5, when the corrosion process was started, the amplitude of RW increased and travel time decreased in a much large scale than that in the cathode bar. Unlike the signal recorded on the cathode bar, the signals recorded on the anode bar were influenced not only by drying and chloride ingress but also reinforcement corrosion.

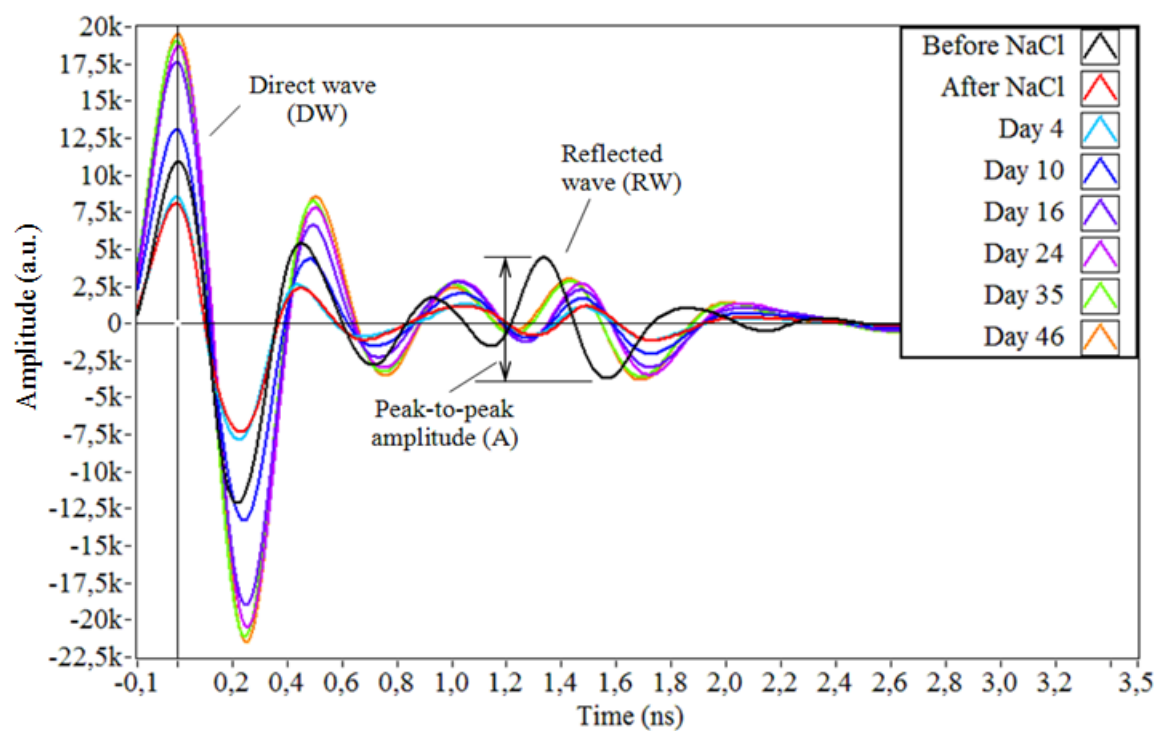


Figure 5.4. Time domain A-scans recorded on cathode bar during Setup 1.

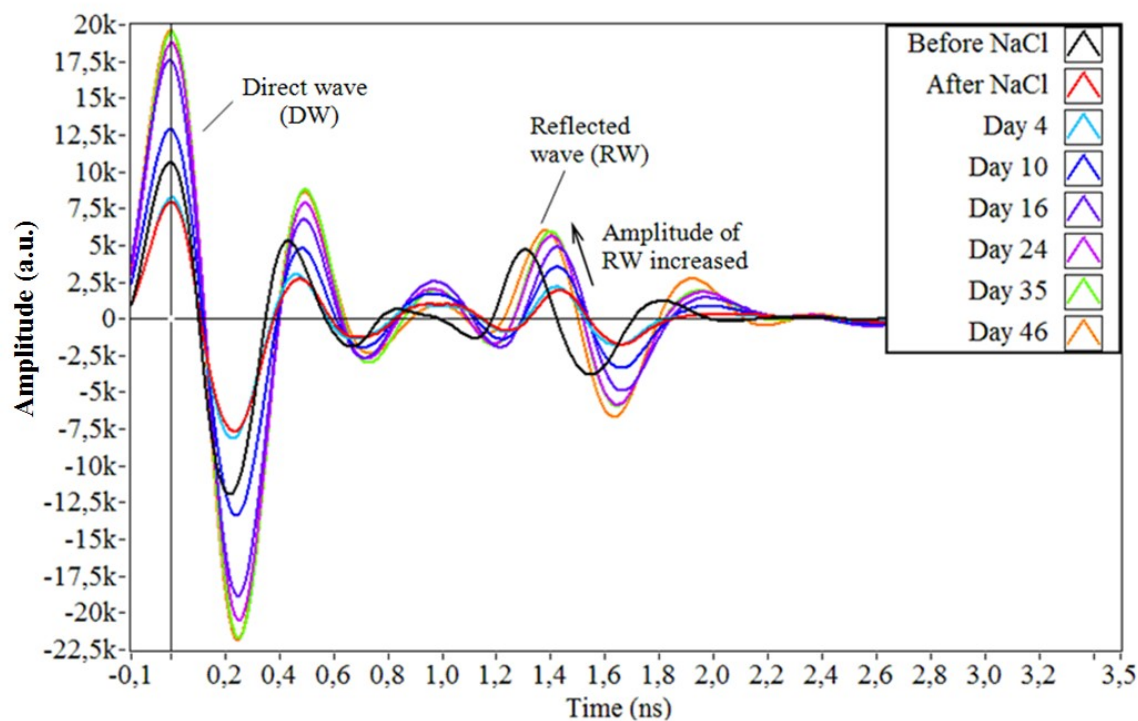


Figure 5.5. Time domain A-scans recorded on anode bar during Setup 1.



- **Change of peak-to-peak amplitude (A) of the reflected wave**

Figure 5.6 shows the variation of the peak-to-peak amplitude (A) of the reflected wave record on the cathode and anode bar during Setup 1, which was obtained by the following steps:

- locate the A-scan signal with maximum reflected amplitude of both cathode and anode bar for all 13 vertical survey lines according to Figure 5.1
- calculate the peak-to-peak amplitude of the rebar reflected waves from the reinforcements according to Figure 5.4 and Figure 5.5
- normalize the obtained peak-to-peak amplitude values (A) in relation to the amplitudes measured before chloride contamination
- calculate the mean value and standard deviation of normalized A of all 13 survey lines perpendicular to the alignment of anode and cathode bars
- Repeat steps 1-4 for every measurement during the monitoring period

Due to the drying of cover concrete, the amplitudes recorded on the cathode and anode bar increased after the immersion in chloride solution. After applying the DC across the anode and cathode bar, the normalized amplitude climbed initially and slowed down as the moisture content in the cover concrete became stable. After day 22, the cathode curve tended to be constant and the anode curve tended to increase linearly. Taking the signal recorded at the cathode bar as a reference, the difference between anode and cathode curves can be considered the result of accelerated corrosion. The standard deviations which are shown as the error bar in Figure 5.6 are higher for the anode than for the cathode. This behavior can be explained by the non-uniform corrosion along the anode bar generated by direct current.

The variation of peak-to-peak amplitude of direct wave recorded on the cathode and anode bar was plotted in Figure 5.7. It is observed that the direct wave curve became linear after 10 days, earlier than the reflected wave curve, at 22 days (Figure 5.6), indicating that the moisture content decreased faster in the shallow subsurface, where the direct wave propagates.

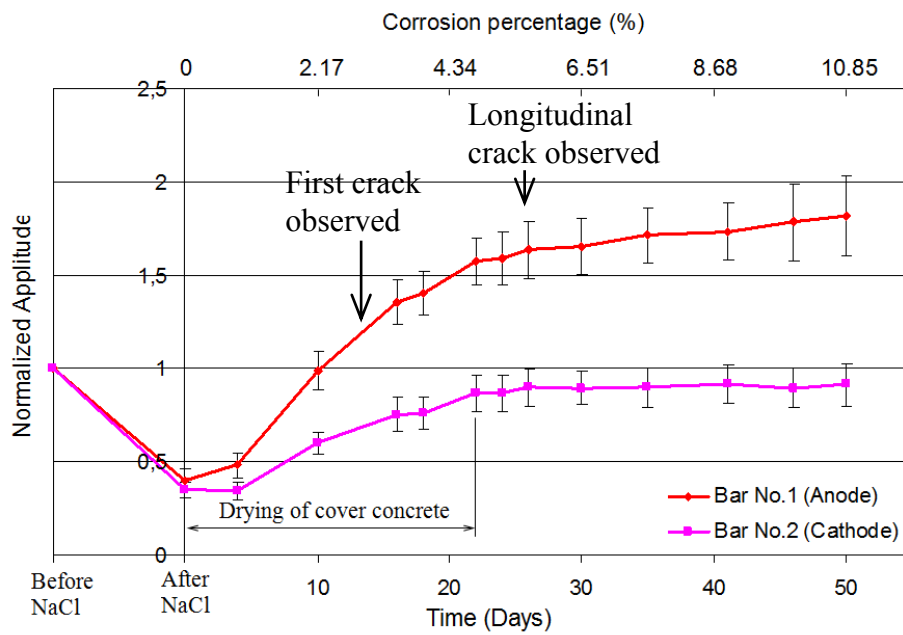


Figure 5.6 Variation of the normalized peak-to-peak amplitude (A) of RW (reflected wave) measured in Setup 1.

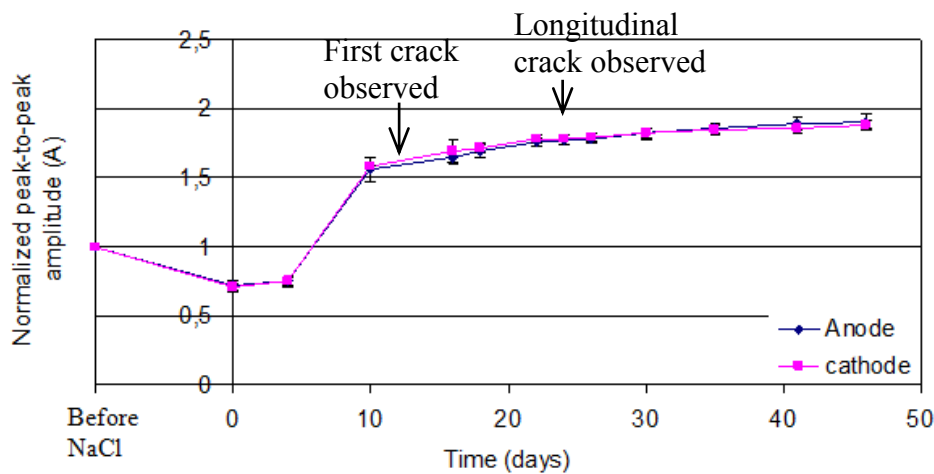
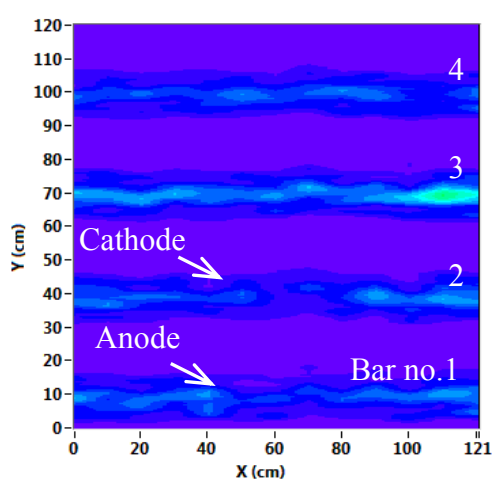


Figure 5.7 Variation of the normalized peak-to-peak amplitude (A) of DW (reflected wave) measured in Setup 1.

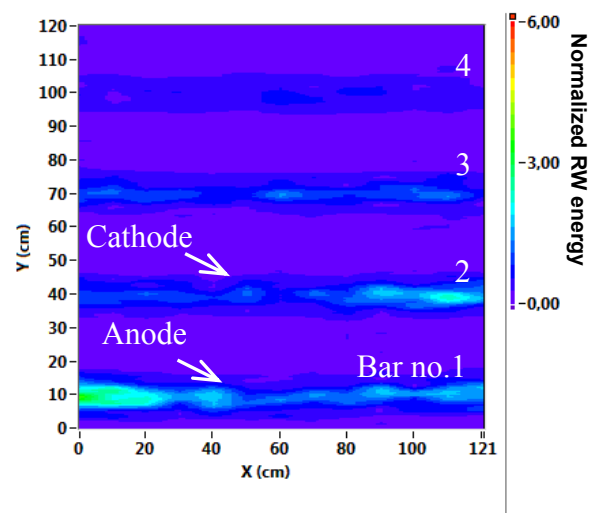
#### • 2D corrosion imaging with signal energy plot.

The change of signal amplitude is enhanced by calculating signal energy (Eq. 3.20) at the depth of the reinforcement and plotted in 2D (Section 3.3.2). During Setup 1, the signal amplitude increased for both the cathode and anode bar. In order to visualize the corrosion

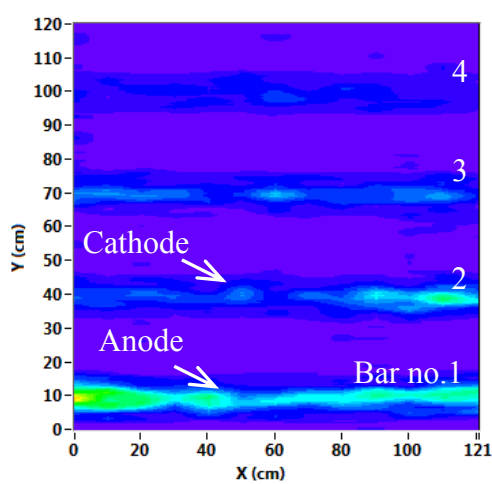
development on the anode bar, for each time step, the calculated signal energy was normalized with the value of the cathode bar. The obtained 2D-energy intensity plots in Figure 5.8 visualize the accelerated corrosion process on the anode bar. The first crack was observed on day 14. In the comparison with the initial state before corrosion (Figure 5.8 (b)), the early-stage corrosion is visualized by the high-energy intensity on the anode bar in Figure 5.8 (c-d), which is consistent with the result of half-cell potential measurement (Figure 5.9) measured on day 16. Then, as the corrosion developed and accumulated, the reflected signal energy continuously increased.



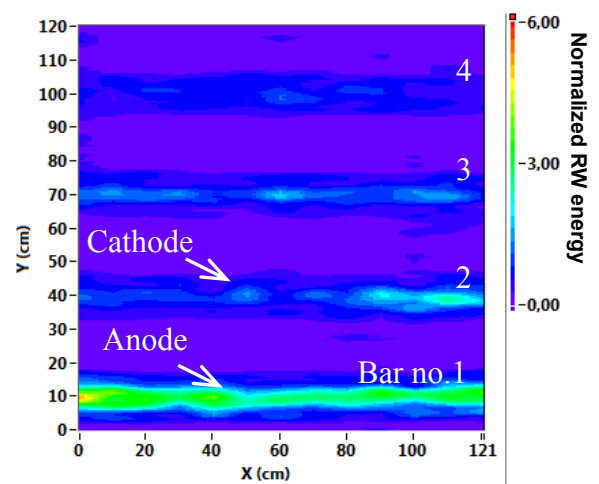
(a) Before chloride contamination



(b) After chloride contamination



(c) Day 4



(d) Day 10

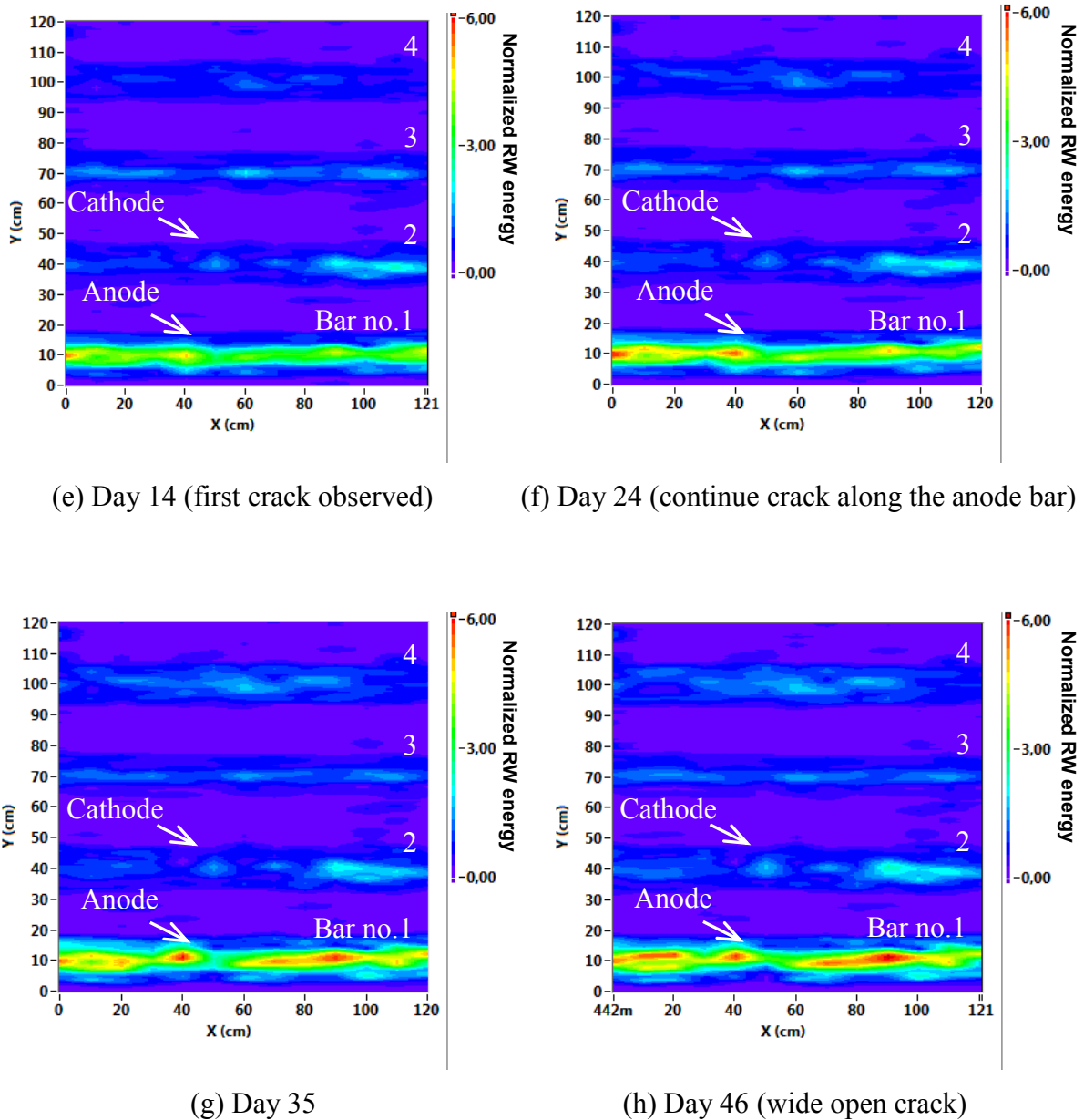


Figure 5.8 Corrosion imaging with normalized signal energy intensity plot (Setup 1): (a) baseline, before chloride contamination, (b) after chloride contamination, (c) Day 4, (d) Day 10, (e) Day 16, (f) Day 24, (g) Day 35, (h) Day 46.

A half-cell potential mapping was conducted on day 16 and the result in Figure 5.9 shows that the active corrosion progressed non-uniformly with higher risk of corrosion on the two ends of the anode bar where a more negative potential value is shown. This phenomenon can also be associated with the energy mapping in Figure 5.8 (f), (g) and (h), after day 24. The GPR signal energy intensity was higher, on the two ends of the anode bar.

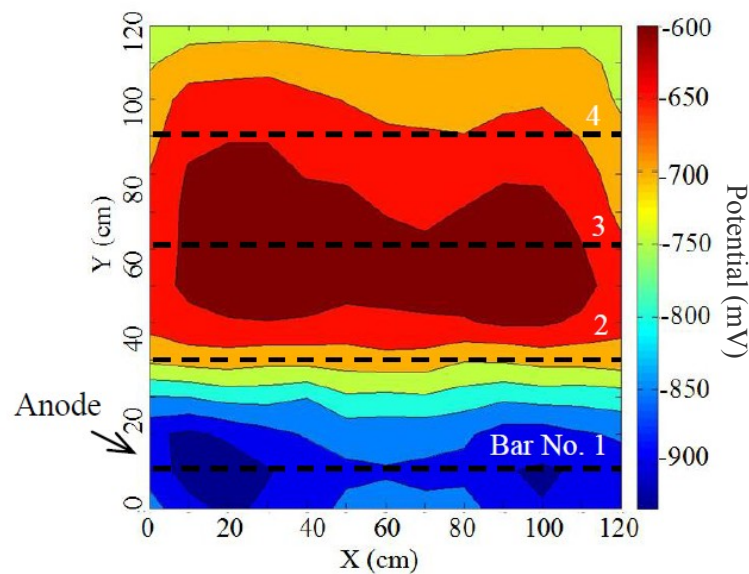
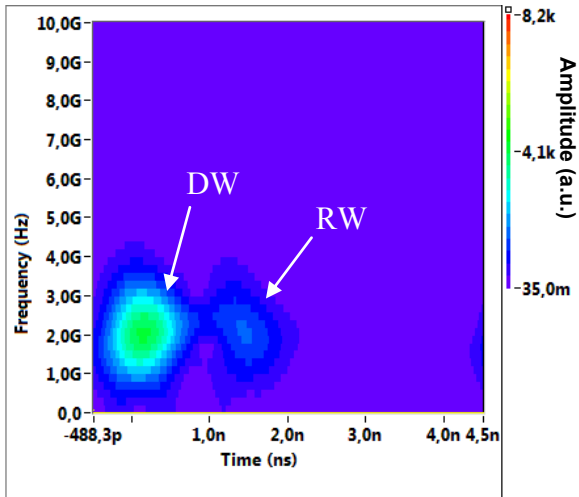


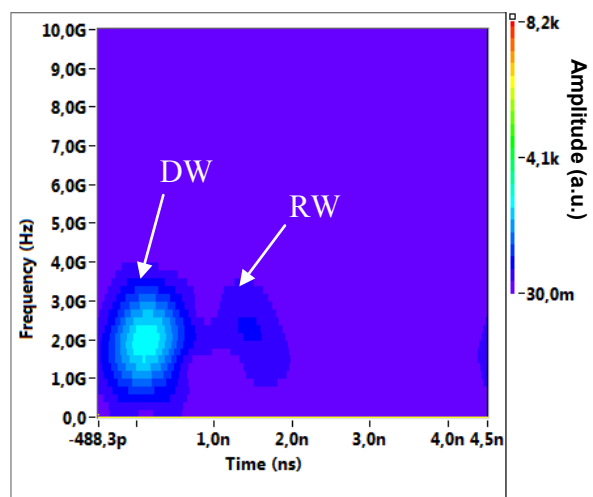
Figure 5.9 Half-cell potential contour map measured on day 16 of Setup 1.

- **Change of frequency spectrum**

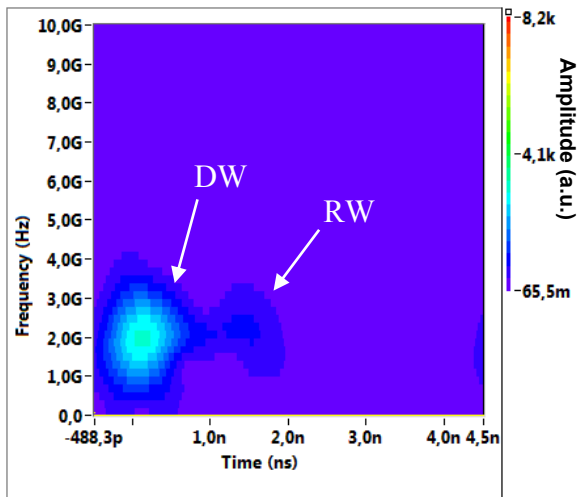
Figure 5.10 represents the signal recorded on the anode bar in time-frequency domain calculated by S-transform. In order to show the change of different measurements, the intensity of the time-frequency spectra was adjusted to the same scale. The frequency spectra of direct wave and reflected wave were extracted from the time-frequency spectra at their arrival time. Figure 5.11 and Figure 5.12 show the spectral content of the direct wave and reflected wave recorded on the anode (point A) during Setup 1. It was observed that the peak frequency of the reflected wave decreased from 2.0 GHz to 1.9 GHz after chloride exposure. Then, as the cover concrete got dry and chlorides migrated into the concrete, the amplitude of the frequency spectrum increased significantly while the peak frequency decreased slightly.



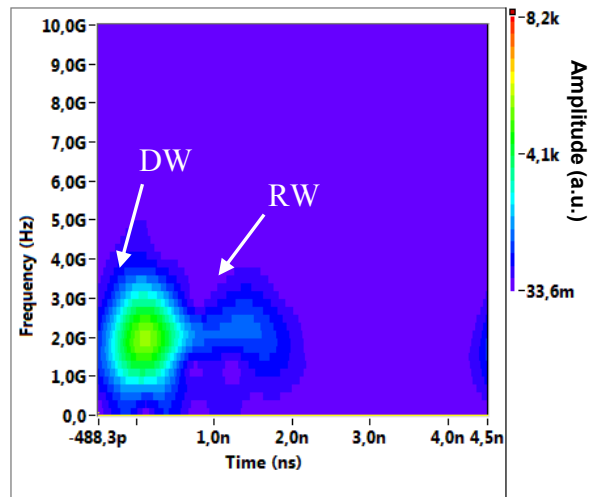
(a) Before chloride contamination



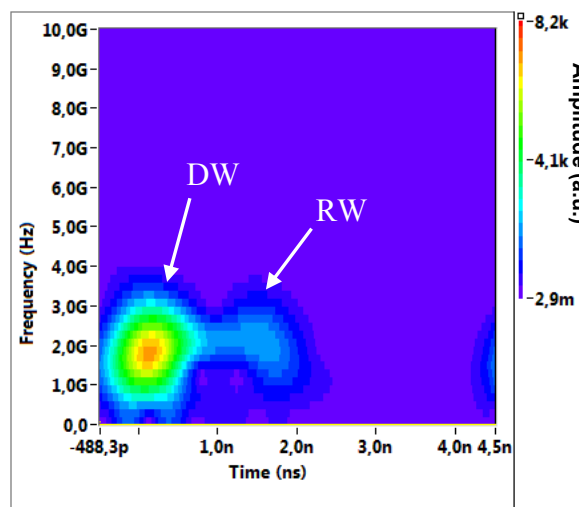
(b) After chloride contamination



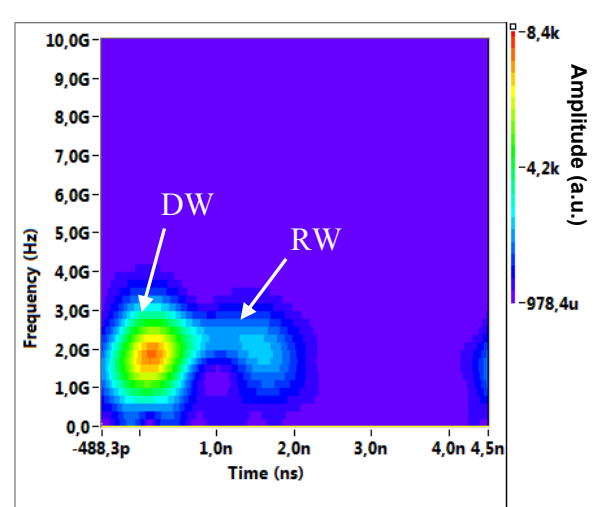
(c) Day 4



(d) Day 10



(e) Day 16 (first crack observed)



(f) Day 24 (continue crack along the anode bar)

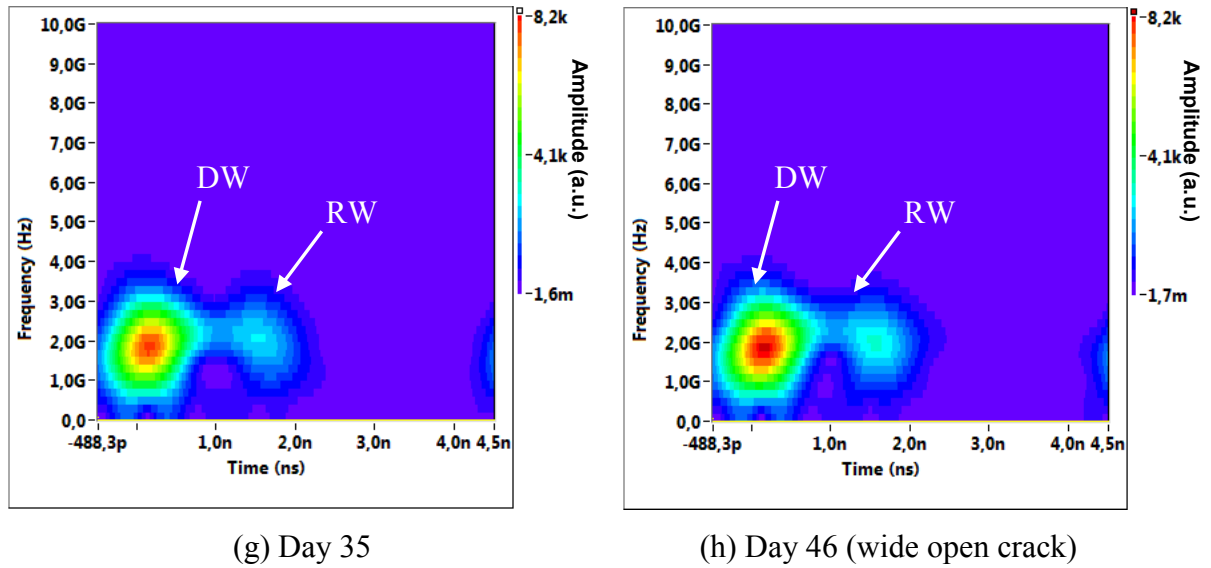


Figure 5.10 Time-frequency spectrogram of the time domain signal recorded on anode bar (Figure 5.5): (a) baseline, before chloride contamination (b) after chloride contamination, (c) Day 4, (d) Day 10, (e) Day 16, (f) Day 24, (g) Day 35, (h) Day 46.

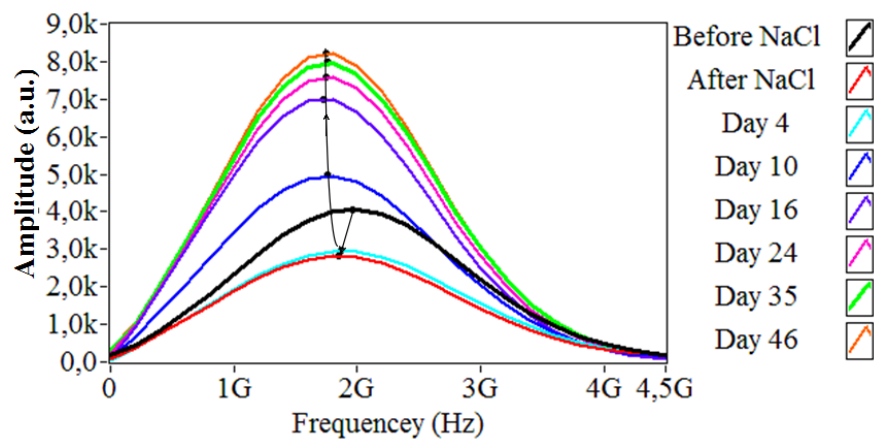


Figure 5.11 Frequency spectra of the direct wave signals recorded on anode bar (point A).

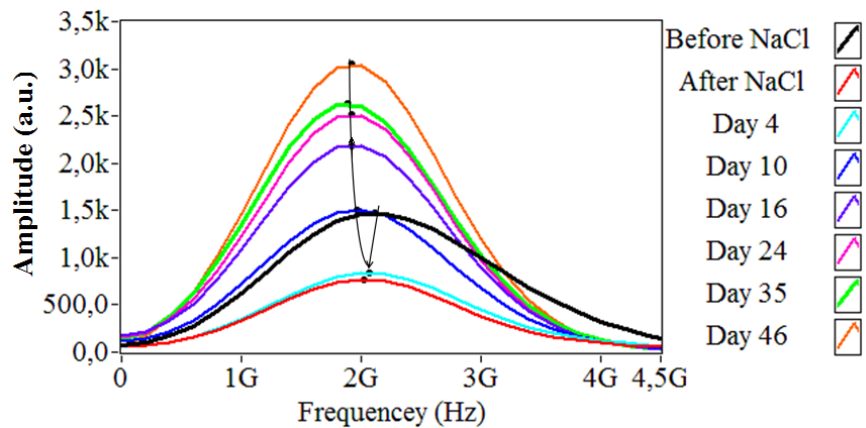
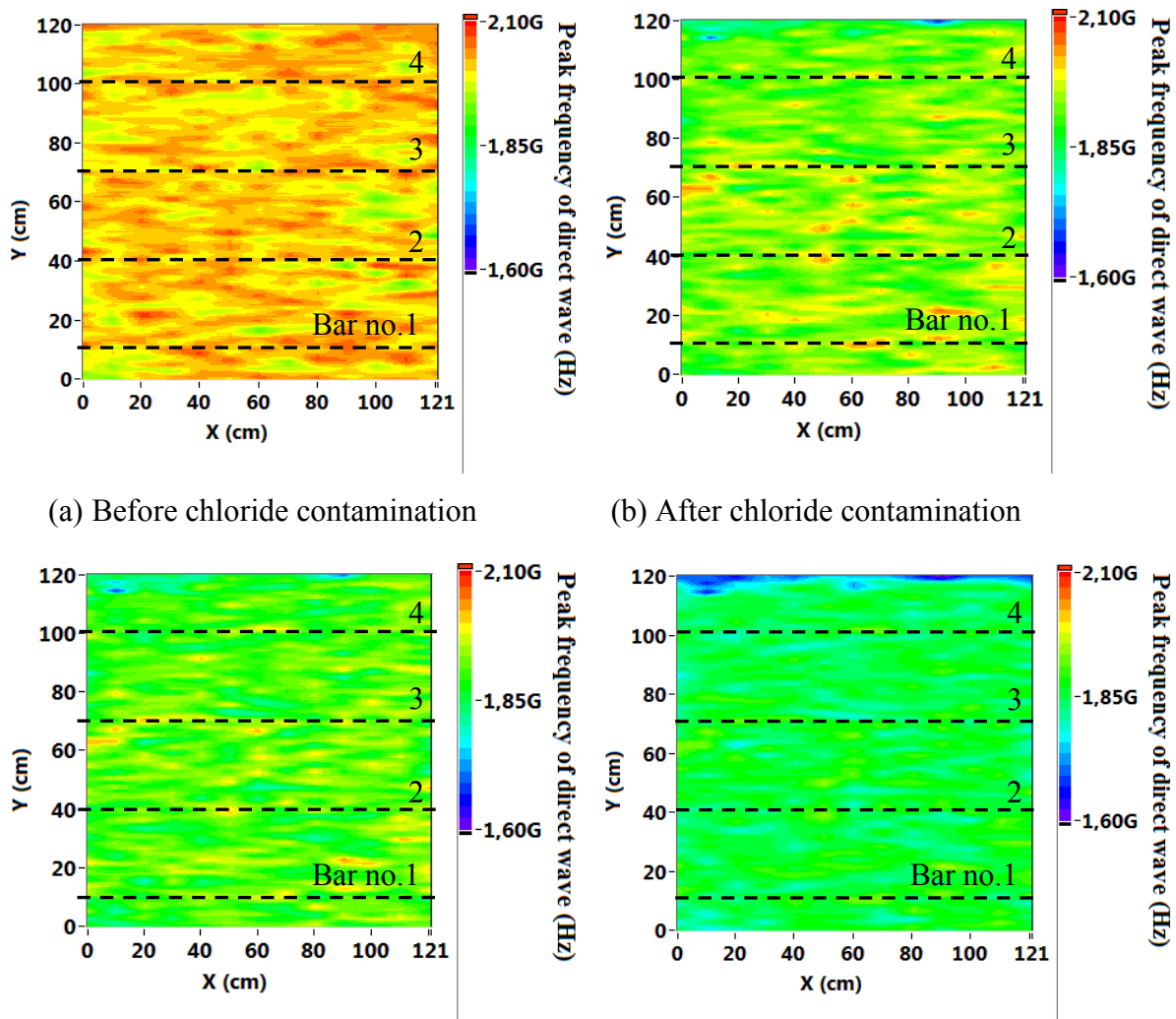


Figure 5.12 Frequency spectrum of the reflected wave signal recorded on cathode bar (point B).

- **2D mapping of peak frequency of direct wave to visualize the distribution of moisture-carrying chloride**

The peak frequency of direct wave for each A-scan was calculated and a 2D interpolation was performed to generate area frequency plots as shown in Figure 5.13. During Setup 1, before immersion in the chloride solution, the specimen was dry, hence the peak frequency of the direct waves for the whole specimen was relatively high (Figure 5.13 (a)). After the immersion in chloride solution, the moisture content increased, resulting in a decreased direct wave frequency (Figure 5.13 (b)). Then, the chlorides were transported and accumulated on the cover concrete surface, which further reduced the signal frequency (Figure 5.13 (c)-(g)). An area with low signal frequency was observed on the upper edge of the specimen, as shown in Figure 5.13 (e), where the concentration of NaCl is higher than the other part of the specimen.





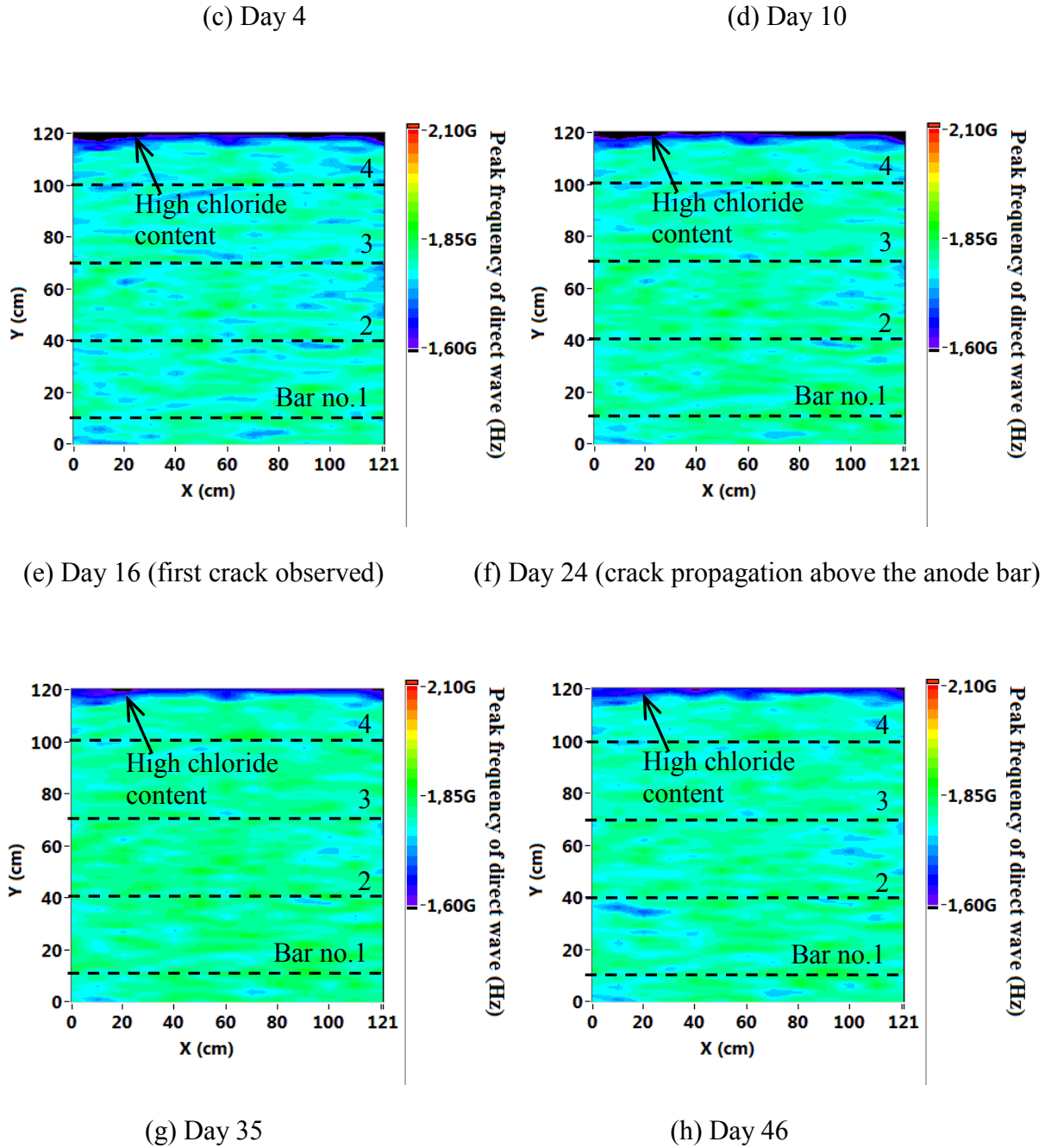


Figure 5.13 Mapping of direct wave peak frequency (Setup 1): (a) baseline, before chloride contamination, (b) after chloride contamination, (c) Day 4, (d) Day 10, (e) Day 16, (f) Day 24, (g) Day 35, (h) Day 46.

### 5.1.3.2 Setup 2

In Setup 1, it was found that the GPR signal was influenced by the change in moisture and chloride concentration. To remove these variables, in Setup 2, the accelerated corrosion process of the second pair of rebars in the upper layer of the same specimen was carried out

under dry conditions. The chlorides from Setup 1 remained in the concrete. After 2 months drying in the air, the chlorides and moisture content were considered to be stable enough for Setup 2.

Bar no. 3 and 4 were used as the cathode and anode bar, respectively. After DC impression for 4 days, cracks appeared on the cover concrete above the anode bar (bar no. 4) and propagated through the specimen in the following 2 days. The cracks appeared much earlier and developed much faster than in Setup 1, for which the cracks appeared after 14 days of impressing current and propagated through the specimen in 10 days. That is because, in the dry environment in Setup 2, less corrosion products penetrated into concrete pores which resulted in higher tensile stress in concrete and earlier appearance of cracks [48].

As a reference to the anode (bar no. 4), there is no significant variation of the signals acquired at the cathode bar (bar no. 3) during Setup 2, which indicates the stability of moisture and chloride content in the concrete. At the anode bar, the amplitude of the reflected wave increased and the signal travel time decreased as the corrosion developed (Figure 5.15), which repeated the observation in setup 1. The error bar of the peak-to-peak amplitude (A) of reflected wave is also summarized in Figure 5.16 and Figure 5.17. The accelerated corrosion on the anode bar (Bar no. 4) was visualized with the signal energy intensity plot, as depicted in Figure 5.17.

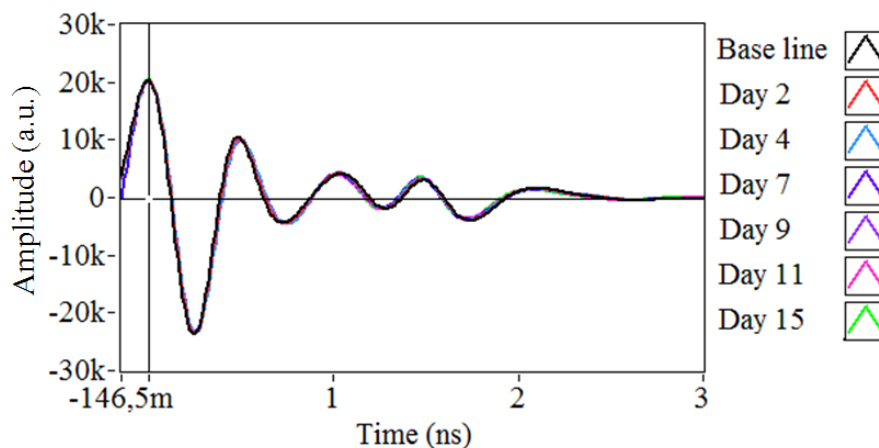


Figure 5.14 Time domain A-scans acquired at point C (cathode): during the experiment stage 2 with a 2.6 GHz antenna.

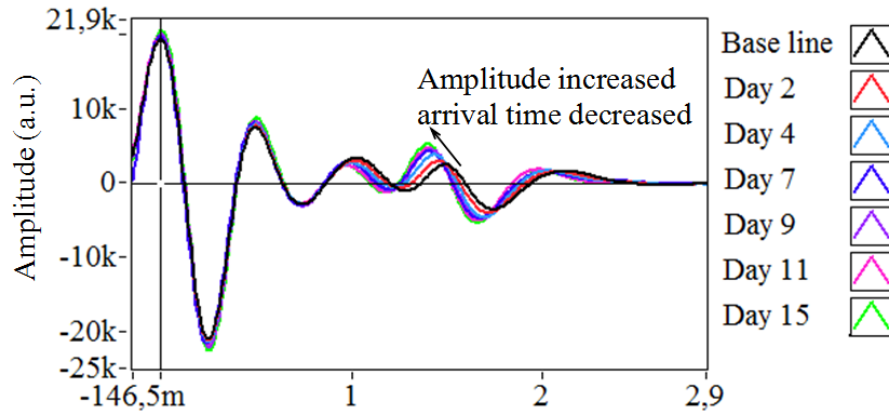


Figure 5.15 Time domain A-scans acquired at point D (anode) : during the experiment stage 2 with a 2.6 GHz antenna.

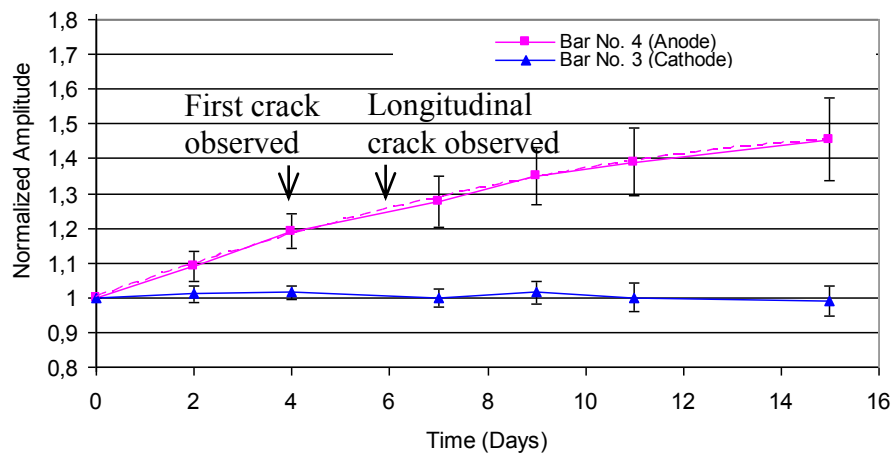
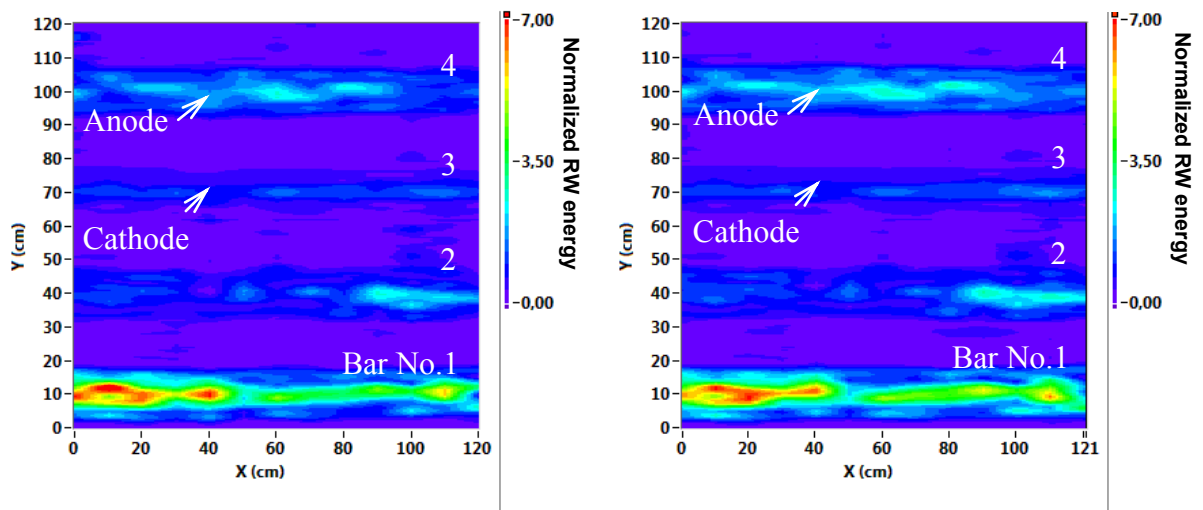


Figure 5.16 Effect of corrosion on the peak-to-peak amplitude (A) measured with a 2.6 GHz antenna in Setup 2



(a) Day 2

(b) Day 4

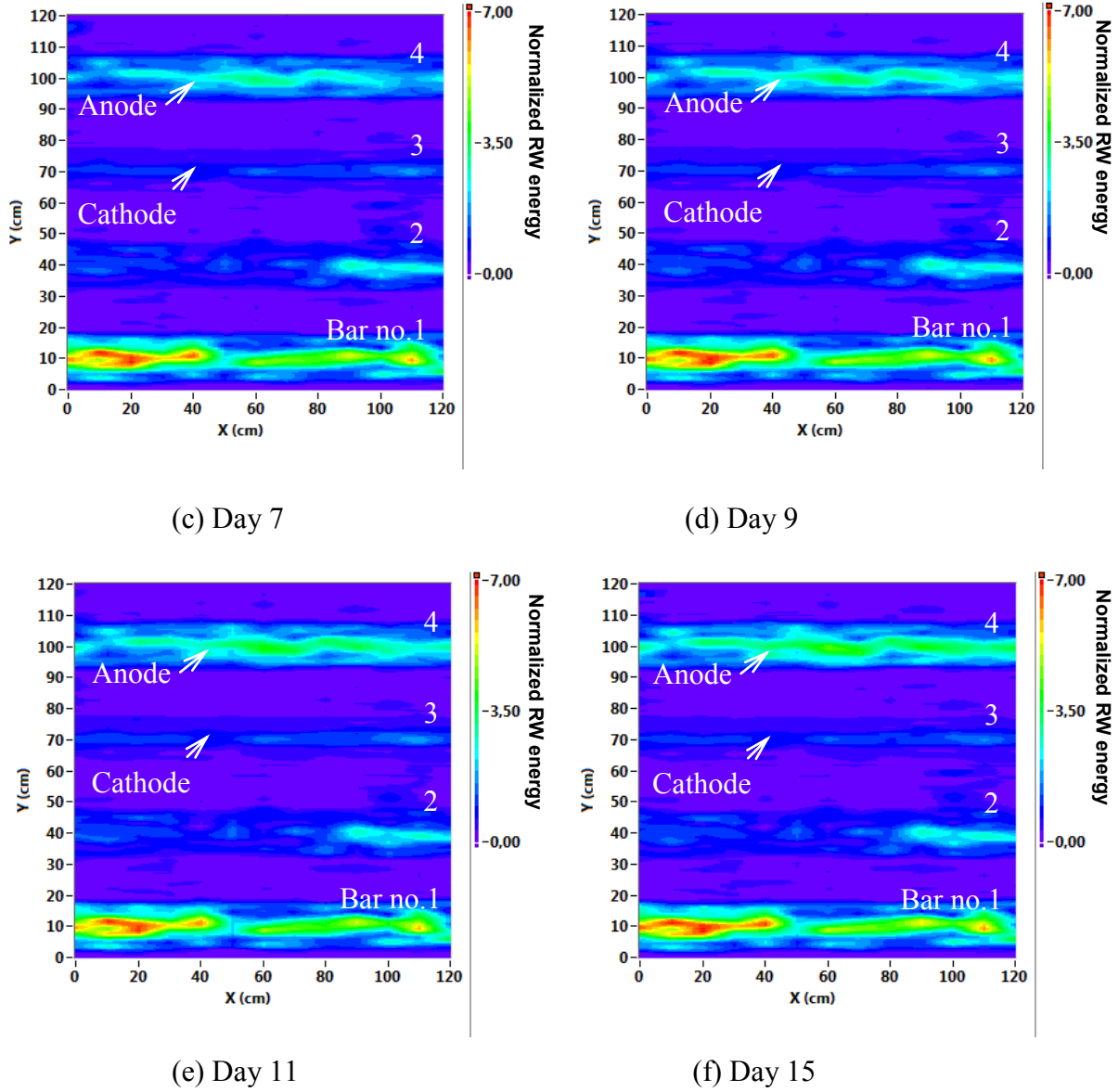


Figure 5.17 Corrosion visualization with normalized signal energy intensity plot (Setup 2): (a) Day 2 , (b) Day 4, (c) Day 7, (d) Day 9, (e) Day 11, (f) Day 15.

The frequency spectra of the anode bar reflected waves were obtained from the time-frequency spectra with the same procedure as used in setup 1. As depicted in Figure 5.18, no significant frequency shift was observed during this setup.

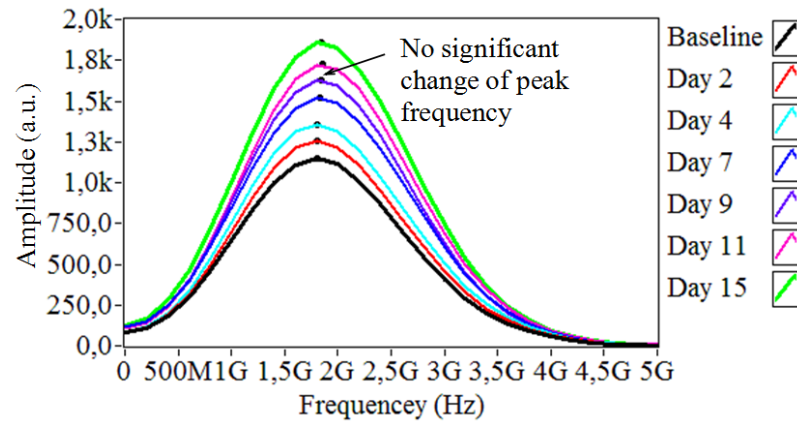


Figure 5.18 Frequency spectra of the reflected wave signal recorded on anode bar (point D).

#### 5.1.4 Verification of the corrosion mapping

After the GPR experiment was completed, core samples were taken from eight positions as shown in Figure 5.19. The corrosion mapping of the GPR signal energy intensity plots was confirmed by destructive observations with the concrete cores:

- Figure 5.20 (a) and (b) show the core samples and the corroded rebar taken from position a (bar no.1) in Figure 5.19. Driven by moisture, the rust penetrated through the cracks. Figure 5.21 shows the core sample taken from position b (bar no.2). No corrosion occurred at this position corresponding to the low-signal energy intensity in that area (Figure 5.17 (f)).
- Figure 5.22 shows the core sample taken from the position f (bar no.2). The rebar was lightly corroded, which can be found out in the GPR signal energy intensity plot (Figure 5.17 (f)).
- Figure 5.23 (a) and (b) show the pictures of the core sample and the rebar taken from position d (bar no.4). It is visible that, since the corrosion was induced in dry conditions, the rust concentrated around the rebar instead of penetrating into the crack.

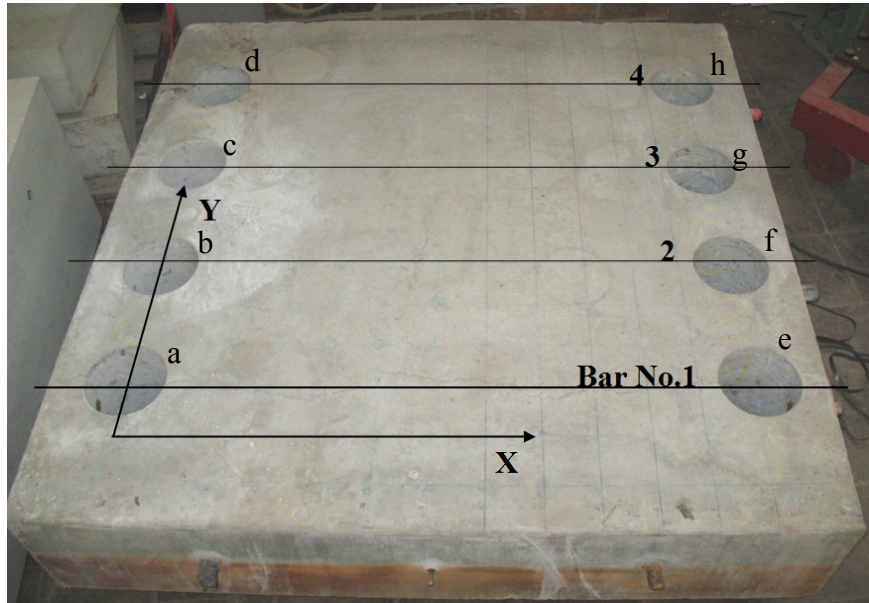


Figure 5.19 Location of the core samples.



(a)



(b)

Figure 5.20 (a) Core sample taken from position a (bar no. 1) in Figure 5.19,  
(b) corroded rebar no. 1 and the stained concrete that surrounded it.





Figure 5.21 Core sample taken from position b.



Figure 5.22. Core sample taken from position f showing the corrosion initiation that occurred.

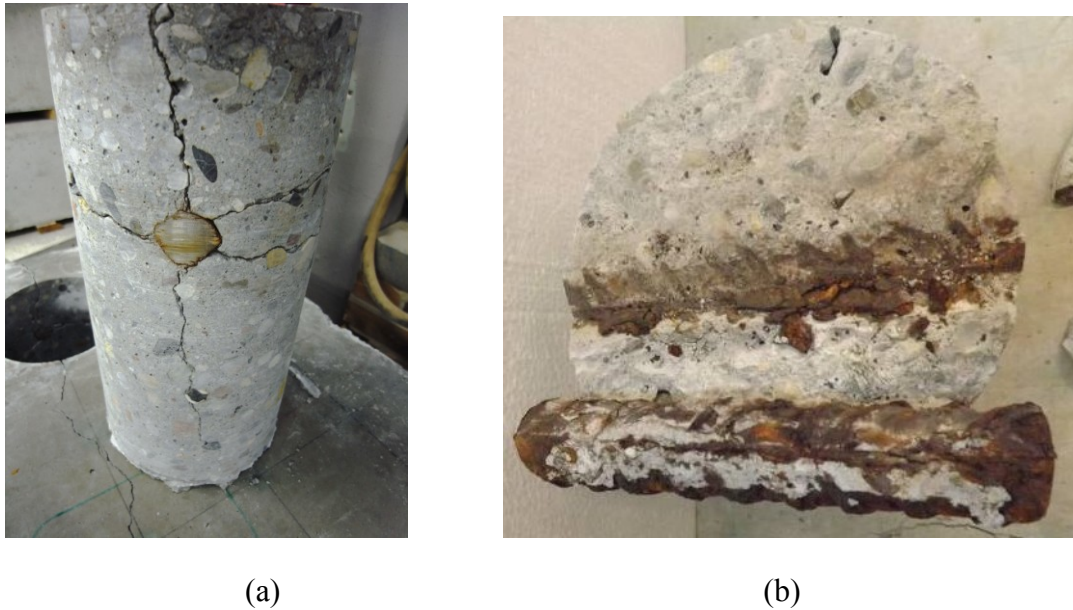


Figure 5.23 (a) Core sample taken from position d, (b) corroded rebar no. 1 and the stained concrete that surrounded it with rust particles.

#### 5.1.5 Verification of the chloride mapping

LIBS chloride measurements were employed to verify the results of chloride mapping. In the setup 1, the specimen was first immersed and then partially submerged in the chloride solution. During this setup, the chlorides were transported into the concrete by absorption, diffusion. In setup 2, the specimen was placed in dry environment, and the chloride ingress stopped. In order to investigate the chlorides' distribution in the concrete, LIBS tests were carried out according to [50]. At the end of the measurements, the core samples were split. Laser-induced breakdown spectroscopy (LIBS) measurements were carried out to investigate the depth profile of chloride content.



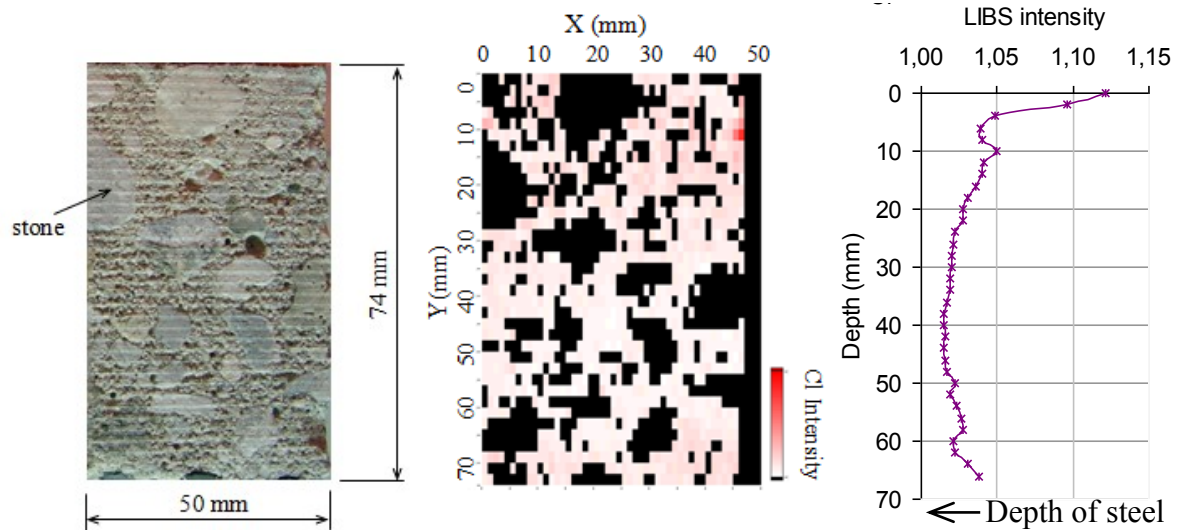


Figure 5.24 (a) The split core from position 1. (b) Spatially resolved chloride distribution: red = Cl, black = absence of Cl (aggregate), (c) Depth profiles of Chloride ingress.

Cl and Na are detected with the wavelength 837.59 nm and 818.32 nm, respectively. The measured intensity values were normalized with the background value. The areas marked with black represent low ratios, i.e. aggregates; the areas marked with pink represent the distribution of chlorides. The result of LIBS was calibrated to evaluate the element concentration. The average intensity was calculated for each horizontal scan line (2 mm wide), obtaining a depth profile plot (Figure 5.24 (c)).

In order to validate the observation in the chloride mapping with GPR DW peak frequency (Figure 5.13 (f)), core samples C1-C6 were taken from the part of the specimen with low direct-wave peak frequency (about 1.6 GHz). Core samples C7-C9 were taken from the part of the specimen with higher direct wave peak frequency (around 1.85 GHz). The position of the core samples can be found in Figure 5.25. The chloride contents in the samples were measured with LIBS. The depth profile in Figure 5.26 (a) shows the distribution of chloride in core C1-C6. The highest concentrations of Cl were found on the top surface (less than 1 cm from the surface). The chloride depth profile of core C7-C9 is shown in Figure 5.26 (b), in which the chloride concentration in the shallow region close to the concrete surface is lower than that for core C1-C6.

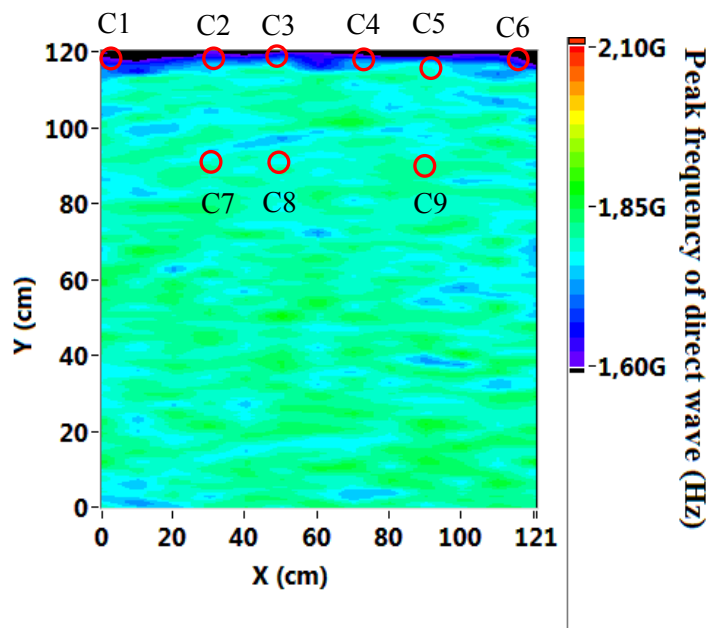
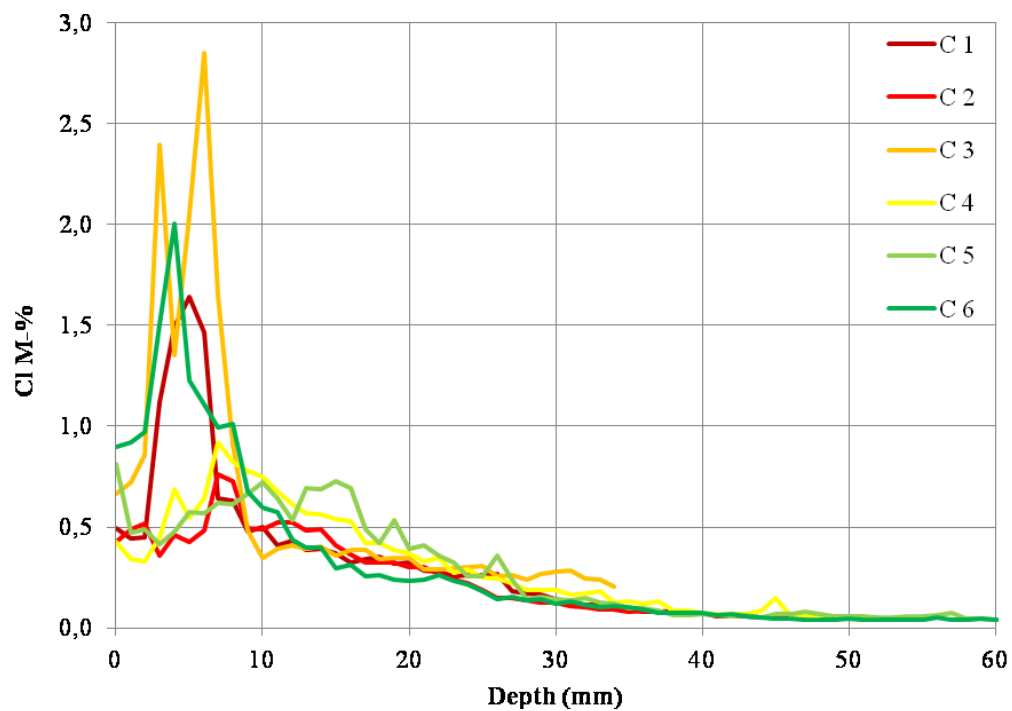
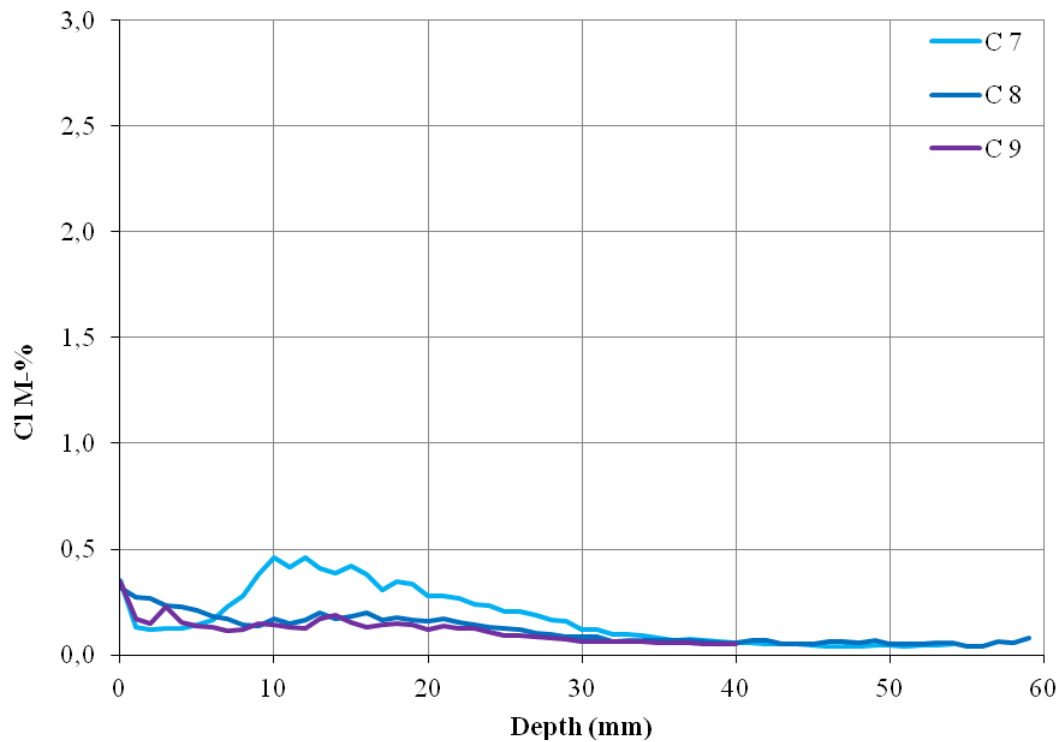


Figure 5.25 Location of the core samples for LIBS test.



(a) Chloride depth profile of the core sample C1-C6.



(b)

Figure 5.26 Chloride depth profile of the core samples measured with LIBS: (a) C1-C6; (b) C7-C9.

### 5.1.6 Discussion

#### 5.1.6.1 Effect of corrosion on GPR signal

From the result of Setup 1 and 2, it was found that the amplitude of the rebar reflected wave is more sensitive to the corrosion than the frequency. The amplitude of reflected wave increased and the travel time decreased as the corrosion developed. Based on Chen's corrosion model, this phenomenon can be explained mainly by three mechanisms:

- the property of the concrete-steel reflection interface changes after corrosion initiates, which is caused by the rust accumulation in the concrete-steel
- the cracks propagated in the concrete matrix
- the diffusion of the rust into the concrete pore structure and crack

All these mechanisms could result in a larger and multiple interface (including concrete, cracks, rust, air and steel), which manifested the stronger reflection of the GPR signal from the corroded rebars.

#### **5.1.6.2 Effect of moisture and chloride on GPR signal**

In Setup 2, it was observed that, when the moisture and chloride content was stable, the reinforcement corrosion didn't influence the GPR signal frequency. The change of center frequency observed in Setup 1 can be considered as only related to the change in moisture and chloride content in the cover concrete.

- **Moisture**

From the results (Figure 5.4, Figure 5.5, Figure 5.11 and Figure 5.12) it was observed that the the change in moisture content in the cover concrete after immersion leads to significant modification of the signal waveform. First, in time domain, the arrival time of the reflected wave was delayed and the amplitude of direct wave and reflected wave decreased as a result of increases in the real part of dielectric permittivity. The time flight of the signal depends on the permittivity. According to the mixing law in section 3.2.4, after the immersion the permittivity of concrete increased, leading to a decrease in the propagation velocity (Equation 3.2). In frequency domain, the peak frequency of direct wave and reflected wave decreased after the immersion. The decreases in signal amplitude and peak frequency were caused by the increase in signal attenuation during propagation related to the increase in concrete conductivity (section 3.2.3). This phenomenon was also observed in Laurens' experiment [53]. According to previous research [54], the decrease in the amplitude of the direct wave can be explained by the antenna-ground coupling effect. The dielectric permittivity of the material influences the radiation pattern of the antenna. A material with higher dielectric constant, such as wet concrete, tends to decrease the radiation aperture, thus limiting the energy received by the receiving antenna.

- **Chloride**

In Setup 1, after immersion, the cover concrete became dry and chlorides were transported into the concrete and accumulated on the top surface. According to Halabe's mixing law (section 3.2.4), the conductivity of the concrete is mainly related to the chloride and other ionic substances in pore solution. The increase in chloride concentration in concrete pore solution causes an increase in the signal attenuation.

The peak frequency of direct wave was selected as an indicator of signal attenuation related to moisture and chloride contamination. The features of direct wave have their advantage in being used for characterizing the moisture and chloride content in cover concrete, since it does not require the presence of the reflectors. The DW propagates through this shallow region of the cover concrete. The influence of GPR direct wave can be estimated with the following approximation [55]:

$$z = \frac{1}{2} \sqrt{\frac{vS}{f}} \quad (5.1)$$

where  $v$  is the EM velocity in the concrete,  $S$  is the separation distance between transmitting and receiving antennas, and  $f$  is the central frequency of the GPR signal. This influence zone is the region in which the chloride concentrates.

A similar research was done by Sbartai et al. [56], in which the amplitude of direct wave was used to evaluate and characterize the conductivity of concrete. However, the amplitude of direct wave is easily influenced by the factors such as the roughness of the concrete surface, and the distance between antenna and concrete. Frequency is a more stable indicator which is not affected by geometrical spreading or reflection losses. Mapping of the frequency of direct wave provides an intuitive plot to visualize chloride/moisture distribution in an area. Higher signal center frequency, which is a result of lower signal attenuation, indicates lower chloride concentration or lower moisture content. In contrast, lower signal frequency, related to high signal attenuation, indicates higher chloride/moisture content.

## 5.2 Experiment 2

The aims of this experiment include:

- testing the reproducibility of the result of Experiment 1
- investigating the influence of the parameters: rebar size and cover depth

### 5.2.1 Preparation of specimens

A total of four reinforced concrete specimens with  $80(L) \times 80(W) \times 24(D) \text{ cm}^3$  in size were manufactured (Figure 5.27). Experiments were carried out 4 months later to make sure the early hydration effect did not affect the GPR signal. Concrete class C35/40 was used. In order to improve the homogeneity of the concrete and reduce the scattering of radar wave, a maximum aggregates' size of 2 cm is designed, which is smaller than the wavelength. Four of them were designed to contain 2% NaCl by weight of cement which was added to the concrete mixture to simulate chloride contamination in concrete. Each specimen was reinforced with a pair of non-contact ribbed rebars with different size and cover depth. The design parameters of the specimens and the test program are summarized in Table 5.2.

Specimen	Dimension (cm)	Diameter of steel bar (mm)	Cover depth (cm)	Impressed current intensity ( $\mu\text{A}/\text{cm}^2$ )	Impressed current (A)
S1	80×80×24	25	4.5	125	0.079
S2	80×80×24	25	9	125	0.079
S3	80×80×24	16	4.5	125	0.050
S4	80×80×24	16	9	125	0.050

Table 5.2 The design parameters of the test specimens and test program

Two reference specimens with 2% ( $R_1$ ) and 0% ( $R_2$ ) sodium chloride (NaCl) by weight of cement added in the concrete mix, respectively, were also manufactured, as shown in Figure 5.28. Each reference specimen was designed to integrate the different design parameters corresponding to the four test specimens. After casting, they were placed in the same lab's indoor environment as the other four test specimens.

The corrosion process of rebars in concrete was accelerated by means of impressing direct current (D.C.). The corrosion rate is directly related to the current intensity. The smaller the

current intensity used, the closer the corrosion conditions to the natural corrosion. According to Gimes [57], when the current density is lower than  $125 \mu A/cm^2$ , the value of current density has no effect on the cracking of concrete cover. In this experiment, impressed current density was typically controlled at  $i = 125 \mu A/cm^2$  to accelerate the corrosion on different test specimens with an identical average corrosion rate.

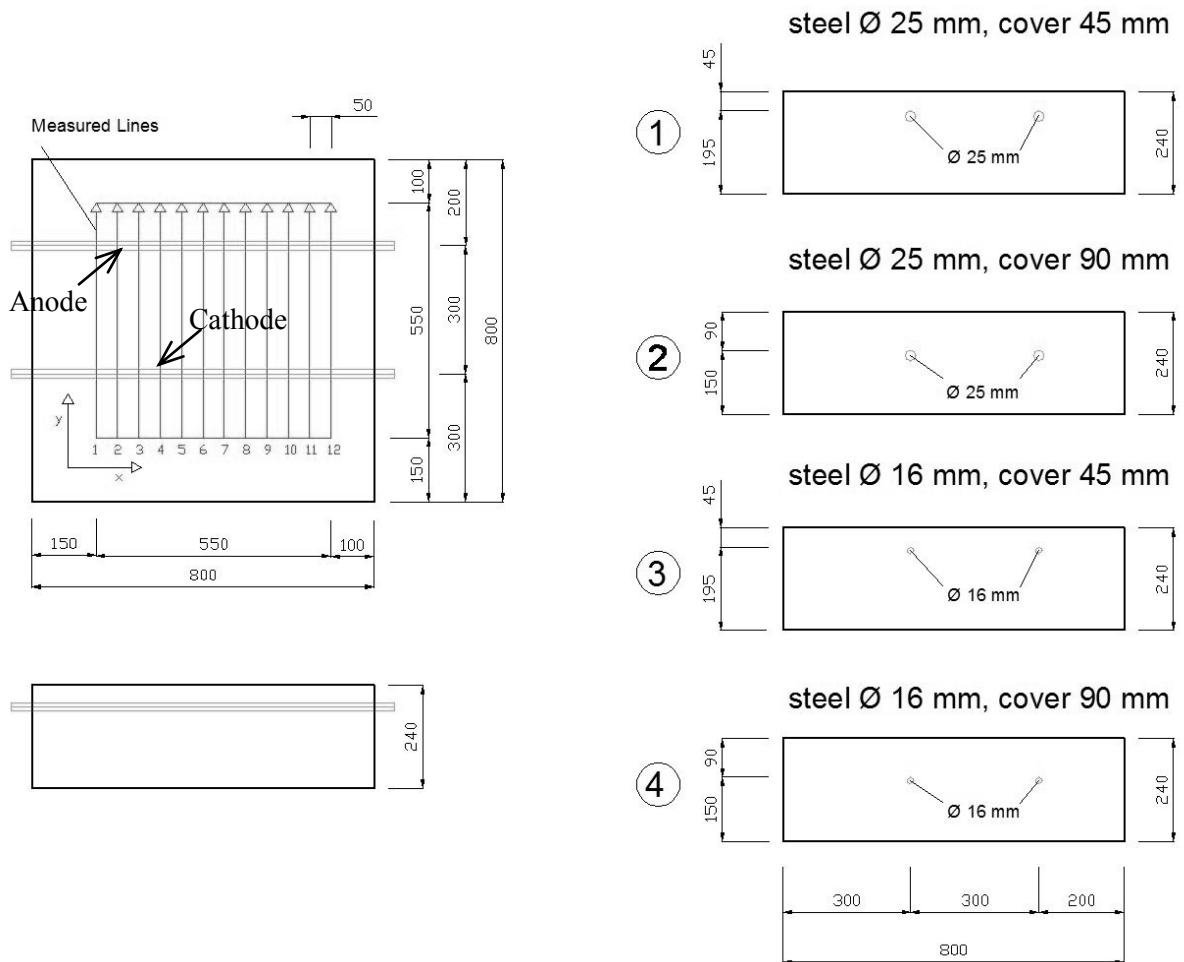


Figure 5.27 Schematic drawing of the test specimens and the measurement grid (unit: mm).

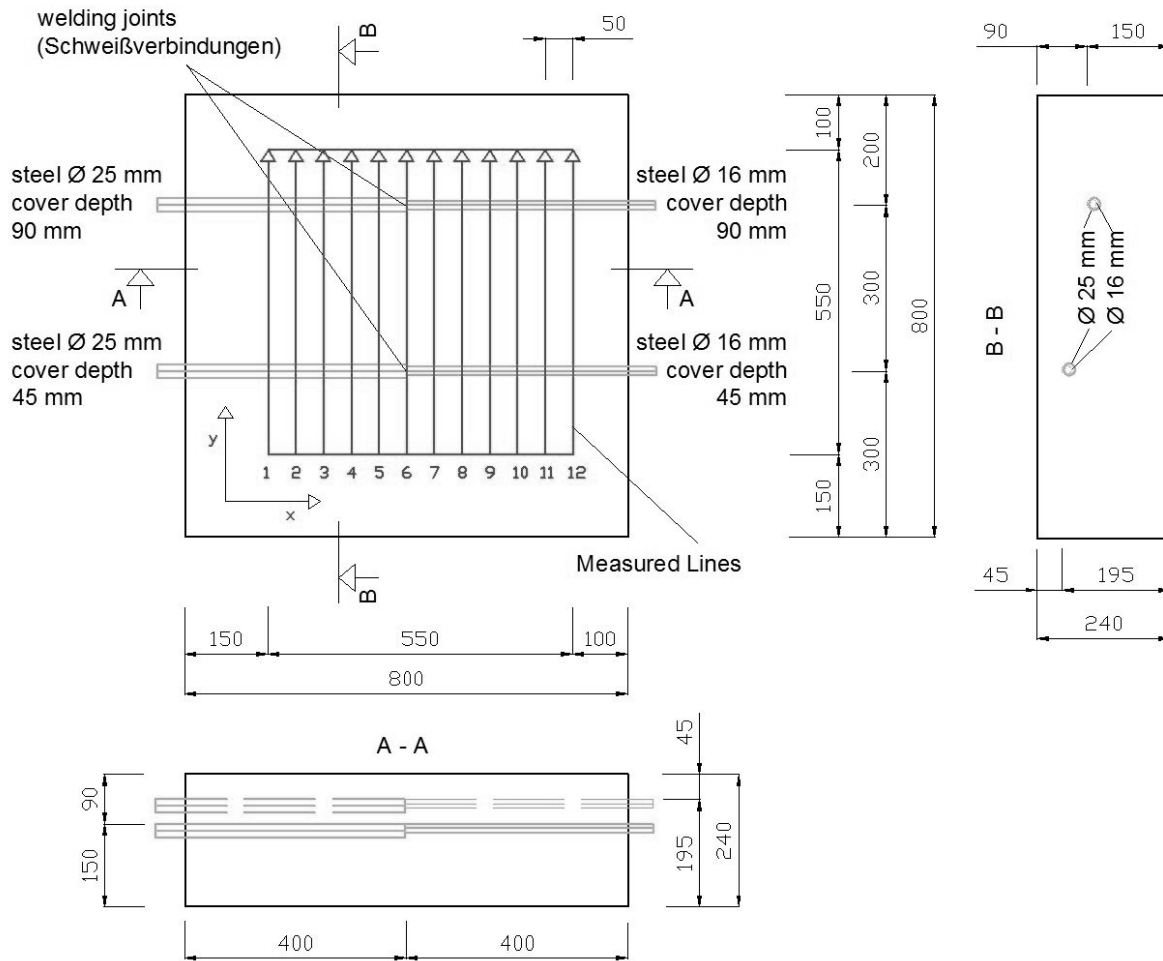


Figure 5.28 Schematic drawing of the reference specimens and the measurement grid  
(unit: mm).

### 5.2.2 GPR measurements

A GSSI SIR-20 system equipped with 2.6-GHz pulse antenna was used to monitor the corrosion process. During the accelerated corrosion process, GPR measurements were carried out every 2 days. 13 parallel survey lines with 5-cm spacing were collected in the y-direction, as shown in Figure 5.27 and Figure 5.28, with the antenna polarized perpendicular to the rebars to get the maximum rebar reflection (sampling rate: 400 scan/m, time window: 8 ns, points per A-scan: 512).



### 5.2.3 Experimental results

- **Time-domain**

Figure 5.29 (a) and (b) show the time domain A-scan waveforms measured over the rebar in test specimens S1 and S2 with 4.5-cm and 9-cm concrete cover, respectively. For specimen S1, the direct wave and the waves reflected by the rebars are represented by the first and second positive peak in the waveforms. For specimen S2, due to the attenuation effect, the reflected wave has smaller amplitude than S1, and is represented by the fourth positive peak in the waveforms.

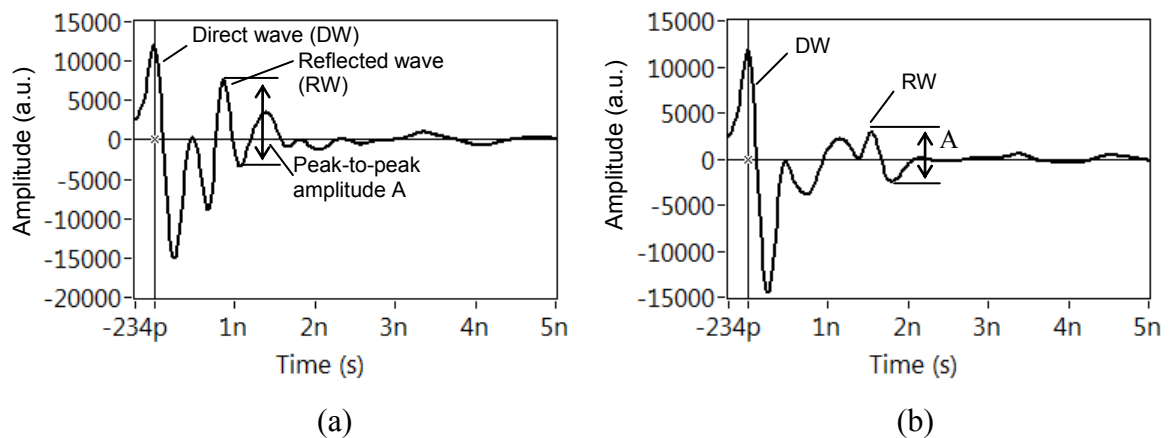
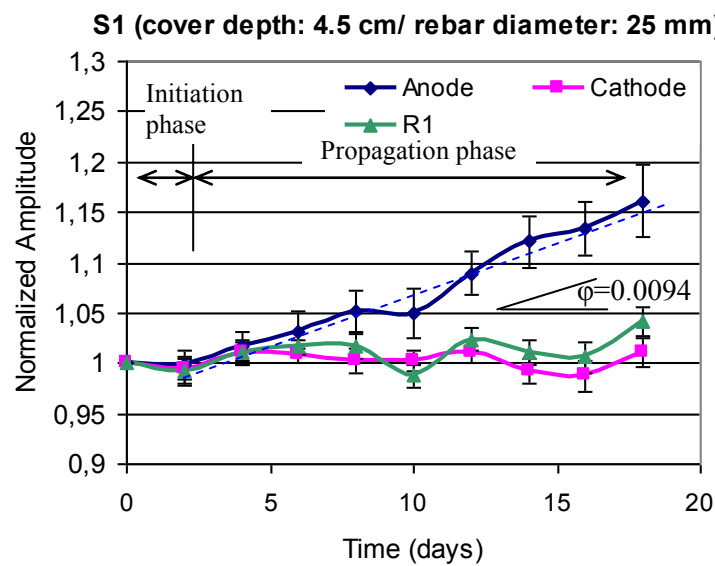


Figure 5.29 Time domain A-scans acquired above the rebar in specimen S1(a) and S2(b).

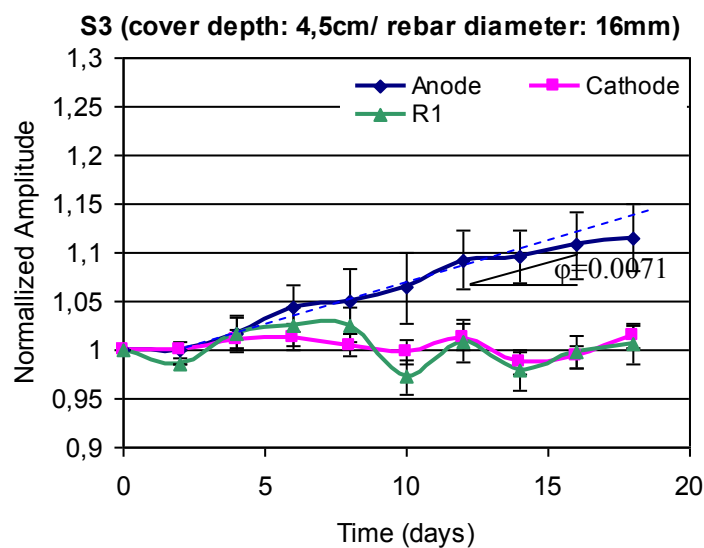
Figure 5.30 (a)-(d) show the development of the peak-to-peak amplitude of the reflected wave for different test specimens during the corrosion process. From these results, it was observed that in the first two days the amplitude didn't change. This phenomenon can be related to the first stage of corrosion initiation of Tuutti's corrosion model (Figure 2.3). Then, after two days, the corrosion process initiated, and the amplitudes of the reflected wave of the anode bar increased. As the corrosion developed, the corrosion products gradually filled the porous interfacial transition zone inducing a change of concrete-air-steel reflection interface into a dense concrete-rust-steel interface which may have caused the increase of reflected GPR signal. Just like with the results in Experiment 1 (Figure 5.6 and Figure 5.16), the standard deviations of the anode are higher than the ones of the cathode and increase during the corrosion process. The reflected amplitude measured on the test specimens with 9-cm cover showed a more pronounced increase than the test specimens with 4.5-cm covers. For a

given cover depth, larger-diameter rebars also cause a stronger increase in the reflected amplitude.

By plotting the reflected signal energy in the area, the corrosion occurring on the anode bar can be visualized, as shown in Figure 5.31, Figure 5.32, Figure 5.33 and Figure 5.34. An increase in signal energy on the anode could be observed before cover concrete cracked (day 6).



(a)



(b)

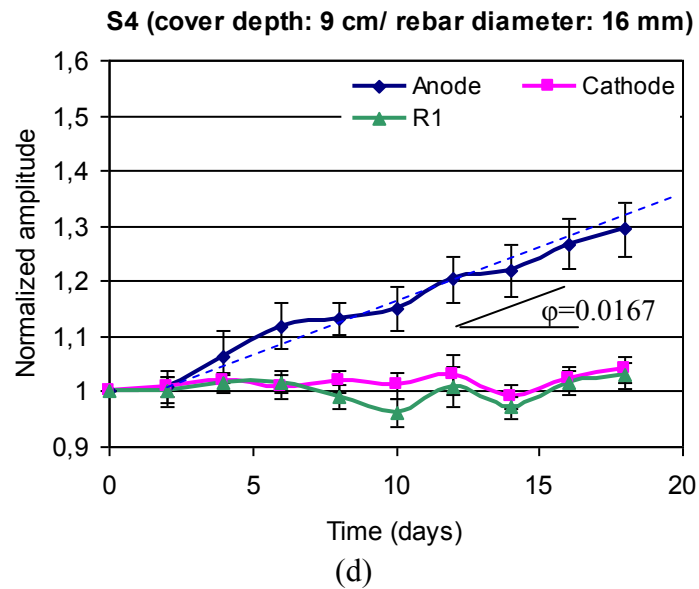
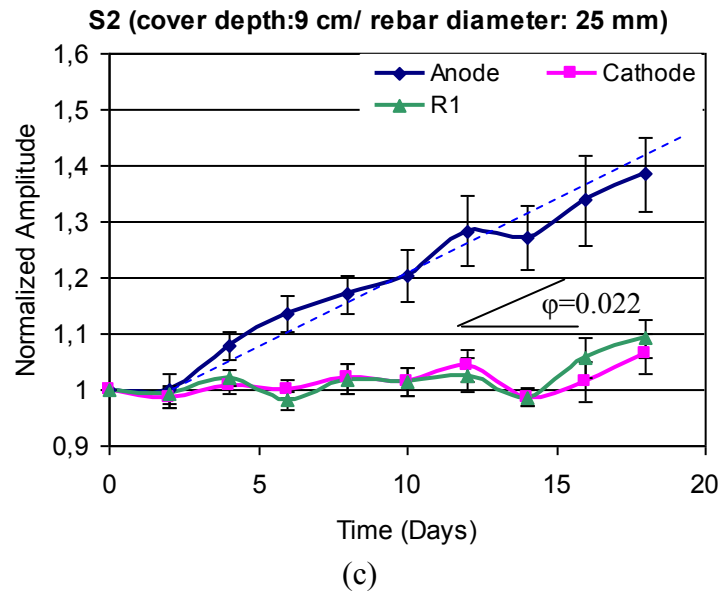
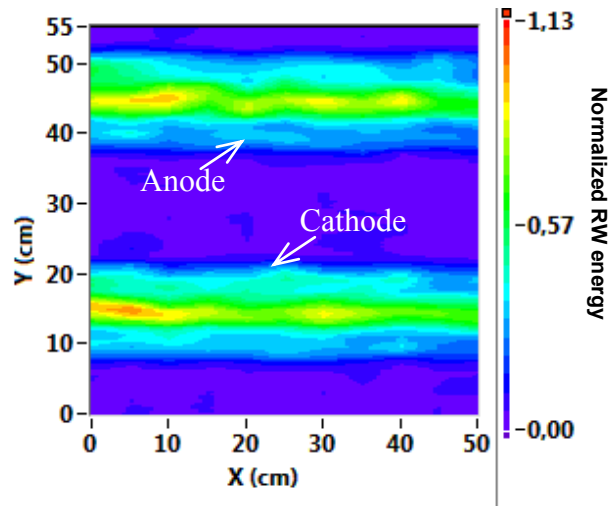
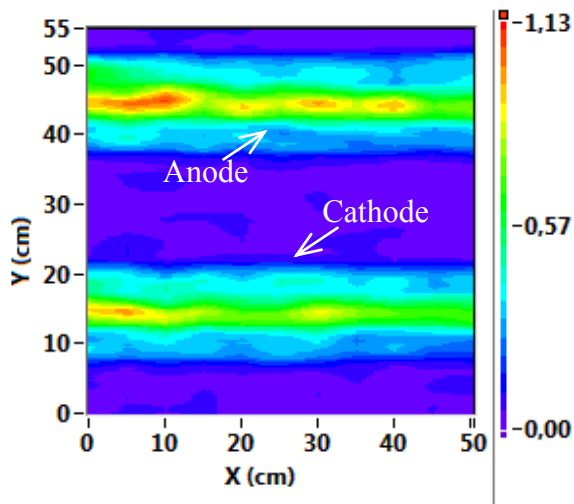


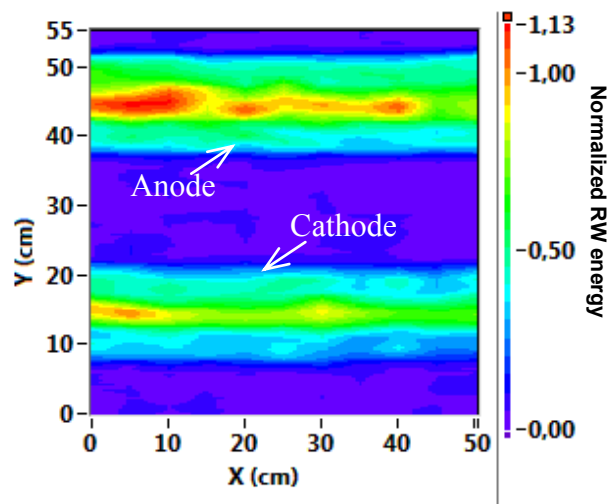
Figure 5.30 Effect of corrosion on the peak-to-peak amplitude (A) measured on: (a) S1, (b) S3  
(c) S2 and (d) S4.



(a) Day 0, baseline

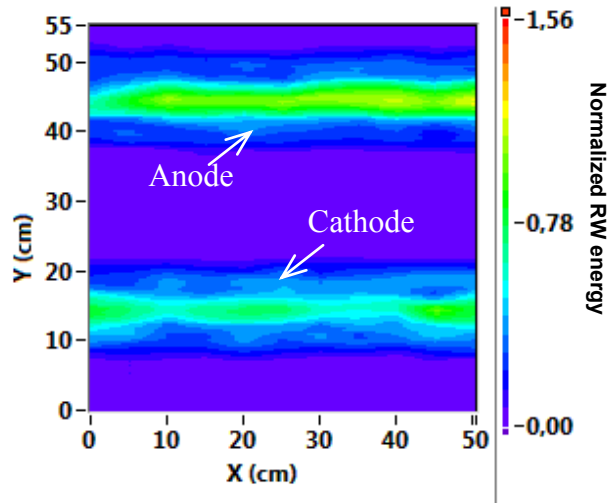


(b) Day 6, before cover concrete cracked

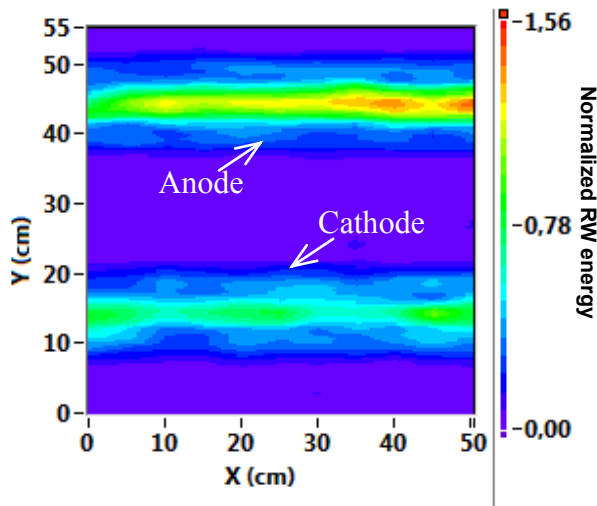


(c) Day 18

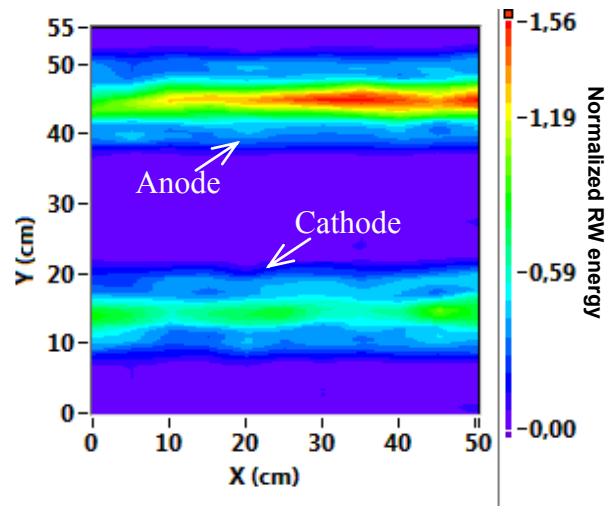
Figure 5.31 Corrosion visualization of specimen S1 (cover: 4.5 cm, rebar diameter: 25 mm) with normalized signal energy intensity plot: (a) day 0, (b) day 6 and (c) day 18.



(a) Day 0, baseline

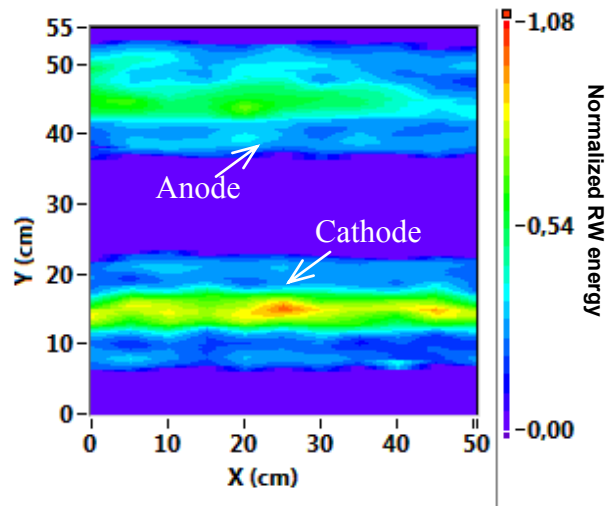


(b) Day 6 before cover concrete cracked

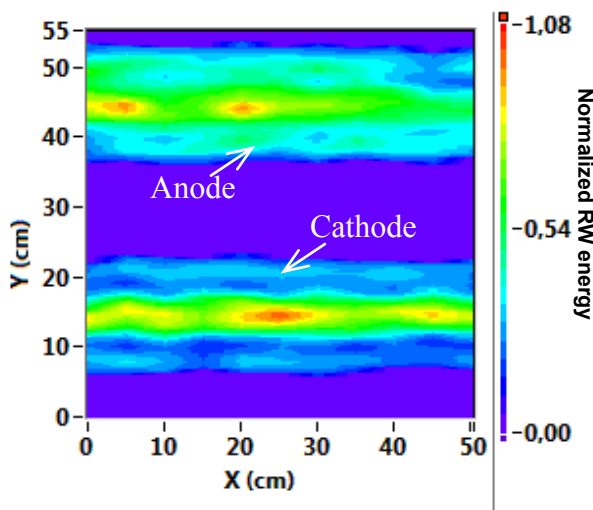


(c) Day 18

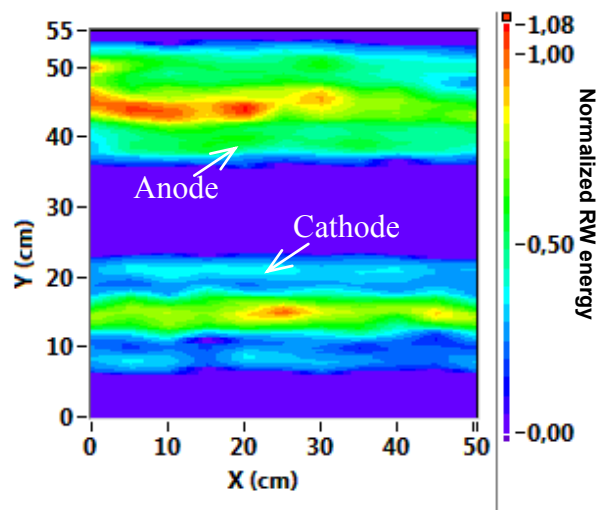
Figure 5.32 Corrosion visualization of specimen S3 (cover: 4.5 cm, rebar diameter: 16 mm) with normalized signal energy intensity plot: (a) day 0, (b) day 6 and (c) day 18.



(a) Day 0, baseline

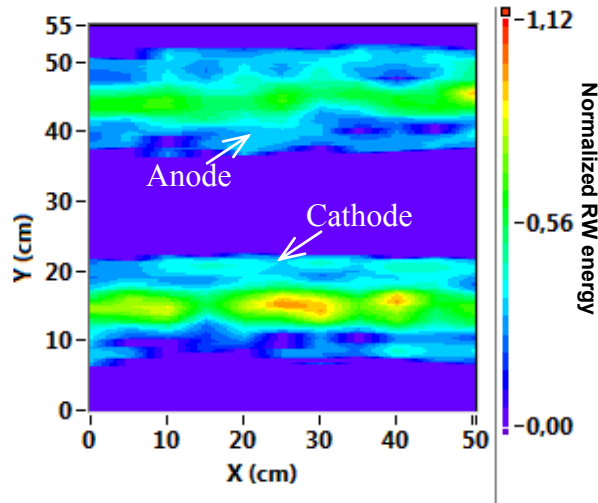


(b) Day 6, before cover concrete cracked

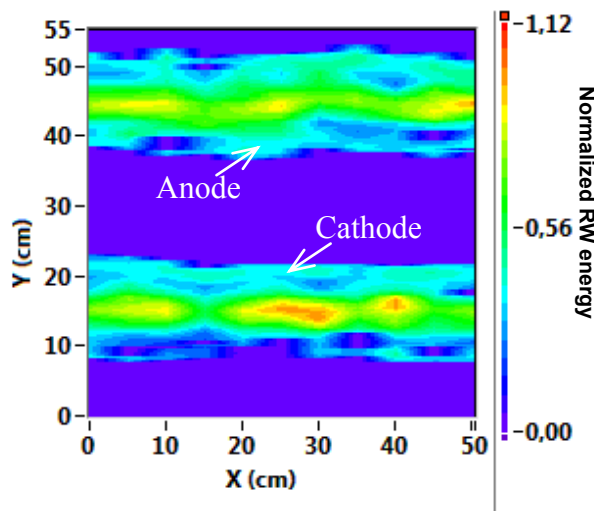


(c) Day 18

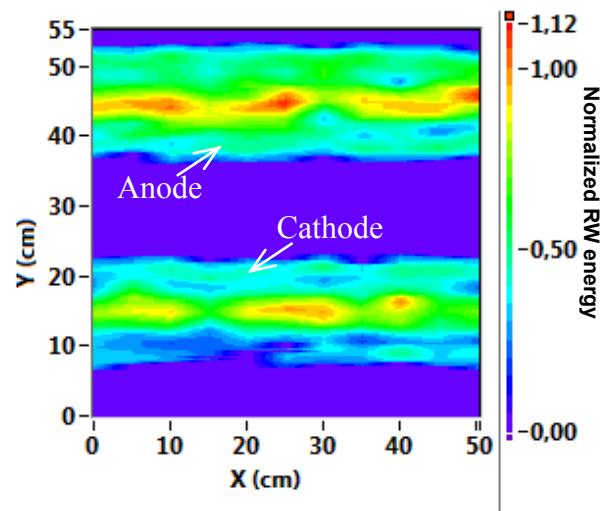
Figure 5.33 Corrosion visualization of specimen S2 (cover: 9 cm, rebar diameter: 25 mm) with normalized signal energy intensity plot: (a) day 0, (b) day 6 and (c) day 18.



(a) Day 0, baseline



(b) Day 6, before cover concrete cracked



(c) Day 18

Figure 5.34 Corrosion visualization of specimen S4 (cover: 9 cm, rebar diameter: 16 mm) with normalized signal energy intensity plot: (a) day 0, (b) day 6 and (c) day 18.

### • Frequency domain

To obtain the frequency spectrum of a reflected wave, first the time-frequency spectrum of the A-scan signal was calculated by using the S-transform, with a sampling rate 8 ns/512. Then, the frequency spectra of DW and RW were subtracted from the T-F spectrum at the arrival time of reflected wave on the time axis. Figure 5.35 (b) and Figure 5.36 (b) show the time-frequency spectrograms of the A-scan signals (Figure 5.35 (a) and Figure 5.36 (a)) acquired above the rebar with 4.5-cm and 9-cm concrete cover, respectively.

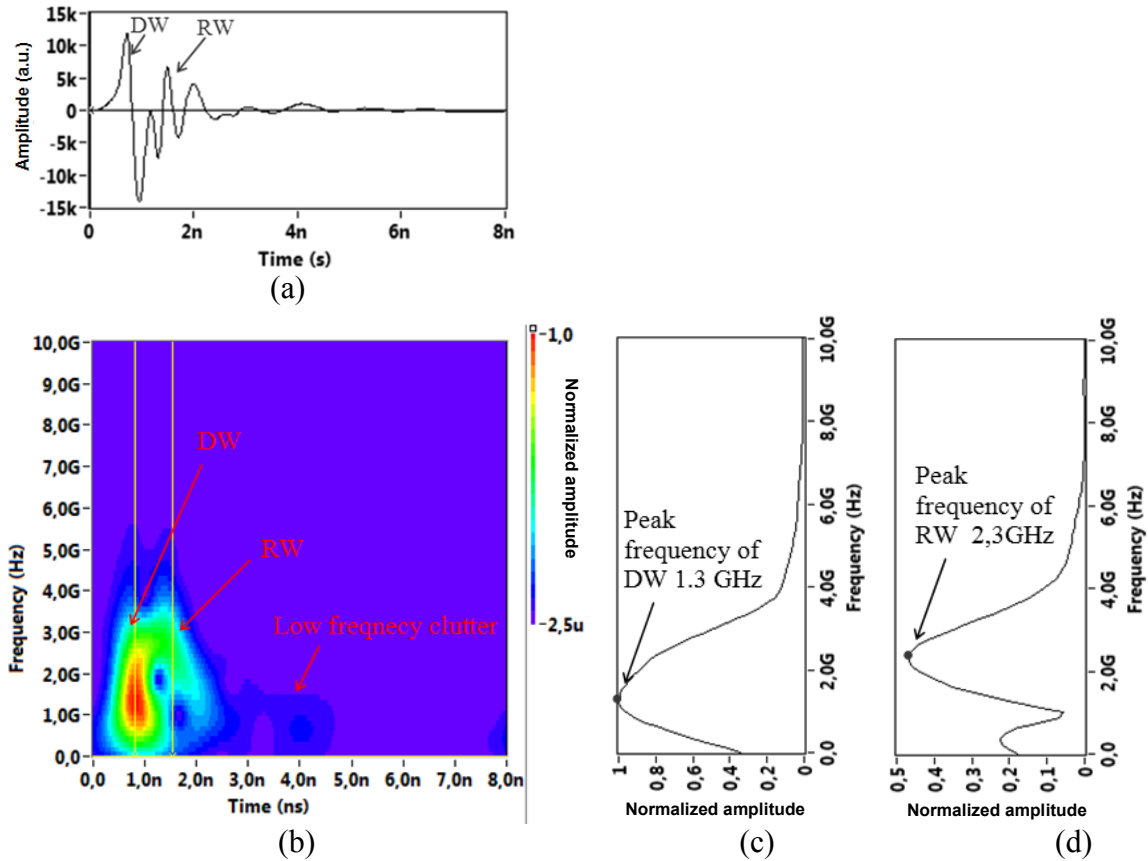
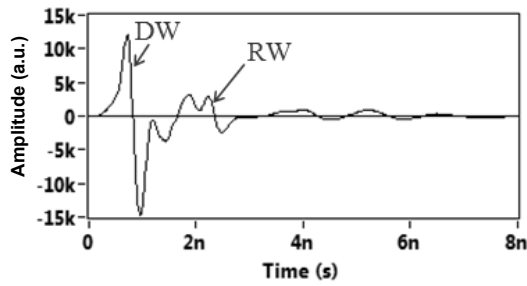


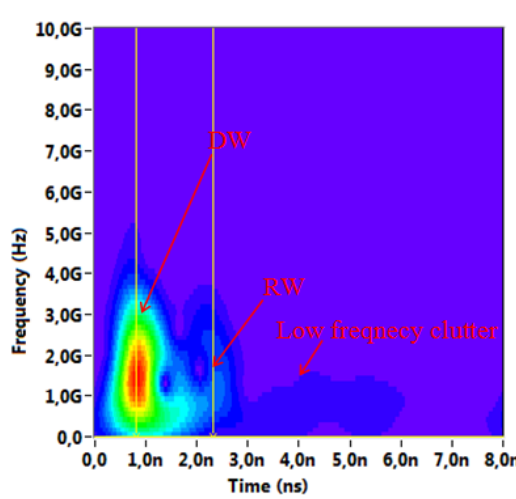
Figure 5.35 Procedure to obtain the frequency spectra of the direct and reflected wave: (a) time domain A-scan measured on S1 (cover: 4.5 cm, rebar size: 25 mm); (b) time-frequency representation of (a); (c) frequency spectrum of DW; (d) frequency spectrum of RW.

Figure 5.37 (a) and (b) are the frequency spectra of reflected waves acquired above the anode bar of test specimens S1 and S2 during the corrosion process. It is observed that the corrosion of the rebar doesn't cause any significant shift in the peak frequency of the reflected wave. The corrosion changes the property of concrete-steel reflection interface. That increases the reflected energy, which is the amplitude of time-domain signal or the amplitude of frequency spectra. However, it doesn't influence the dielectric property of propagation medium (concrete), in which mainly the signal propagates and attenuates. Therefore, the peak frequency of reflected wave didn't change during the corrosion process.

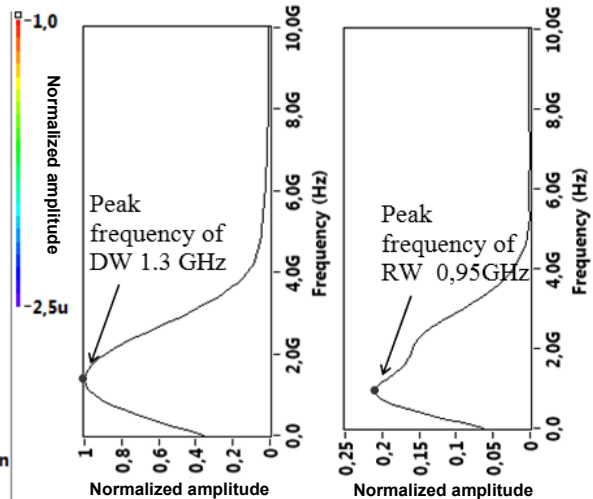




(a)



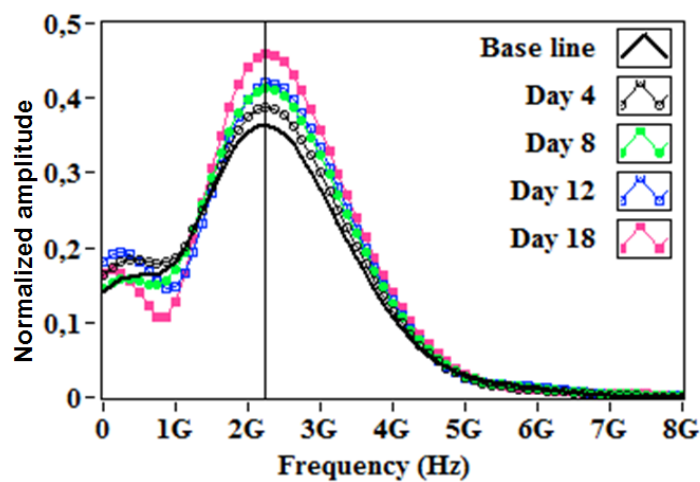
(b)



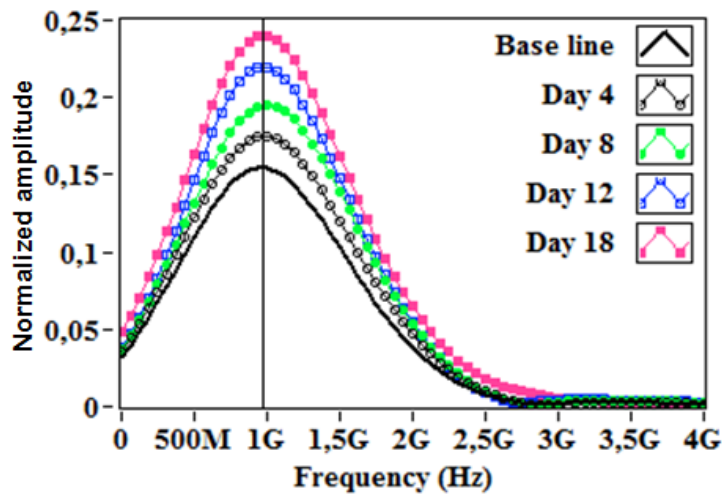
(c)

(d)

Figure 5.36 Procedure to obtain the frequency spectra of direct wave and reflected wave: (a) time domain A-scan measured on S2 (cover: 9 cm, rebar size: 25 mm); (b) time-frequency representation of (a); (c) frequency spectrum of DW; (d) frequency spectrum of RW.



(a)



(b)

Figure 5.37 The frequency spectra of reflected waves acquired above the anode bar of test specimen: (a) S1 (cover: 4.5 cm, rebar size: 25 mm) and (b) S2 (cover: 9 cm, rebar size: 25 mm), during inducing corrosion process.

Figure 5.38 shows the frequency spectra of direct wave and rebar reflected wave of the reference specimens R1 and R2. The signals acquired from the specimen R1 (2% NaCl by weight of cement) were attenuated to lower amplitudes and rendered a lower peak frequency than from R2 (0% NaCl). According to Halabe's mixture law (section 3.2.4), this amount of chloride in the concrete without moisture shouldn't cause any significant change in the dielectric permittivity of concrete. However, there is always a relatively small amount of water in the pores of concrete, which can partially dissolve the chloride. Chloride ions present in water, even with a low concentration, increase the conductivity of concrete resulting in an attenuation of the GPR signal.

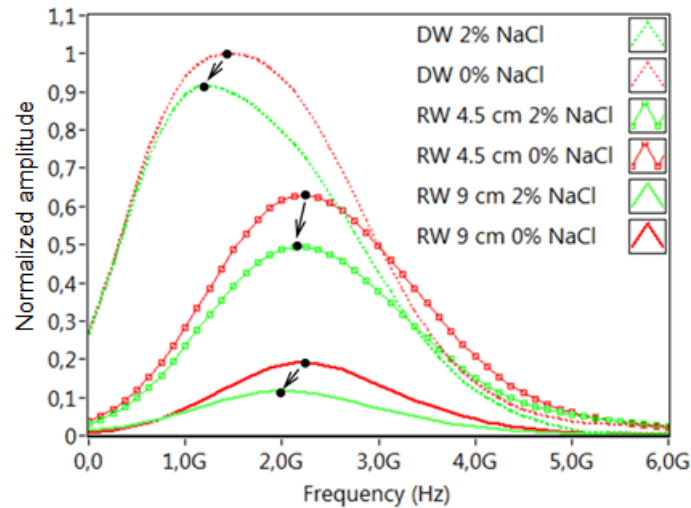


Figure 5.38 Frequency spectra of the rebar reflected waves.

#### 5.2.4 Discussion

The results of this experiment verified the findings of Experiment 1 and investigate the influence of cover depth and rebar size to the radar signal.

- In time domain, the amplitude of the reflected waves increased with increasing corrosion.
- The amplitude of the wavelets reflected by the deeper rebars showed a more pronounced increase than the amplitudes of shallow rebars. For a given cover depth, greater diameter rebars also cause a stronger increase in the reflected amplitude.
- In frequency domain, there is no significant change in the peak frequency of rebar reflected waves during the corrosion process.
- It is also found that, for specimens with 2% sodium chloride by weight of cement cast in the concrete, the GPR signal was attenuated to smaller amplitude and peak frequency. In order to quantify rebar corrosion with GPR signal amplitudes, the influence of chloride and moisture have to be taken into account.

### 5.3 Experiment 3

In Experiment 1 and Experiment 2, the general corrosion of reinforcements was accelerated by using impress current technique. This experiment focused on:

- investigating the GPR signal response to localized **pitting corrosion**;
- transferring the laboratory monitoring of artificial corrosion to the **field long-term monitoring** of general corrosion occurring in ambient environment.

#### 5.3.1 The BAM Large Concrete Slab (LCS)

The LCS was designed and constructed at the BAM site in Berlin in July 2002. The concrete slab is of 10 x 4 m<sup>2</sup> in size with a regular thickness of 30 cm (Figure 5.39) [58]. The concrete slab is partitioned in two sections referring to different testing problems. One section contains tendon ducts with different diameters and grouting defects along the pre-stressing steel. The other section provides areas with varying thickness, voids, auxiliary elements such as thermo-elements, water inlet and reinforcement mats for corrosion testing. To gain full information about an investigated area, a scanner system has been developed to allow for high-resolution testing with high reproducibility. The scanner-system can be used for automated impact-echo, ultrasonic-echo, radar and thermography measurements.

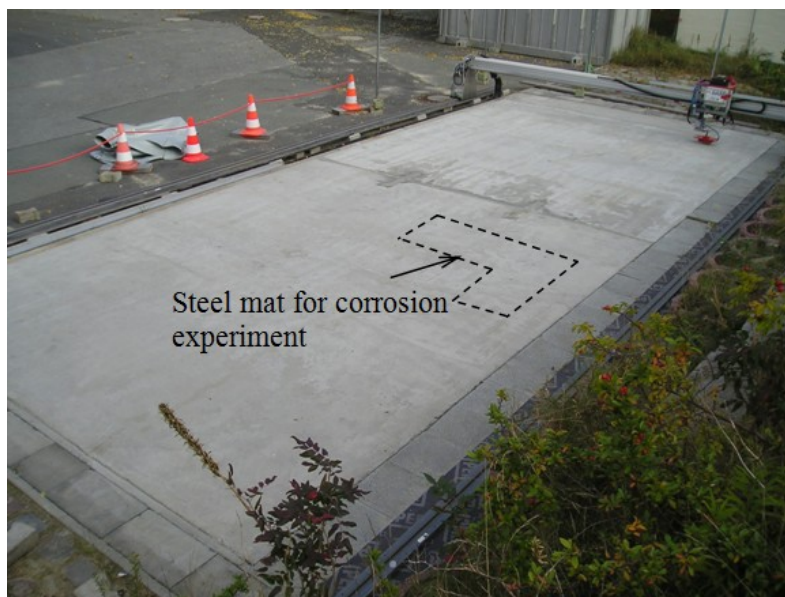


Figure 5.39 BAM Large Concrete Slab.

10-meter-long PVC ducts were imbedded under the slab at a distance of 30 cm (Figure 5.40). These ducts allow for positioning a radiation source approx. 30 cm below the specimen. So radiography is possible for every part of the slab.

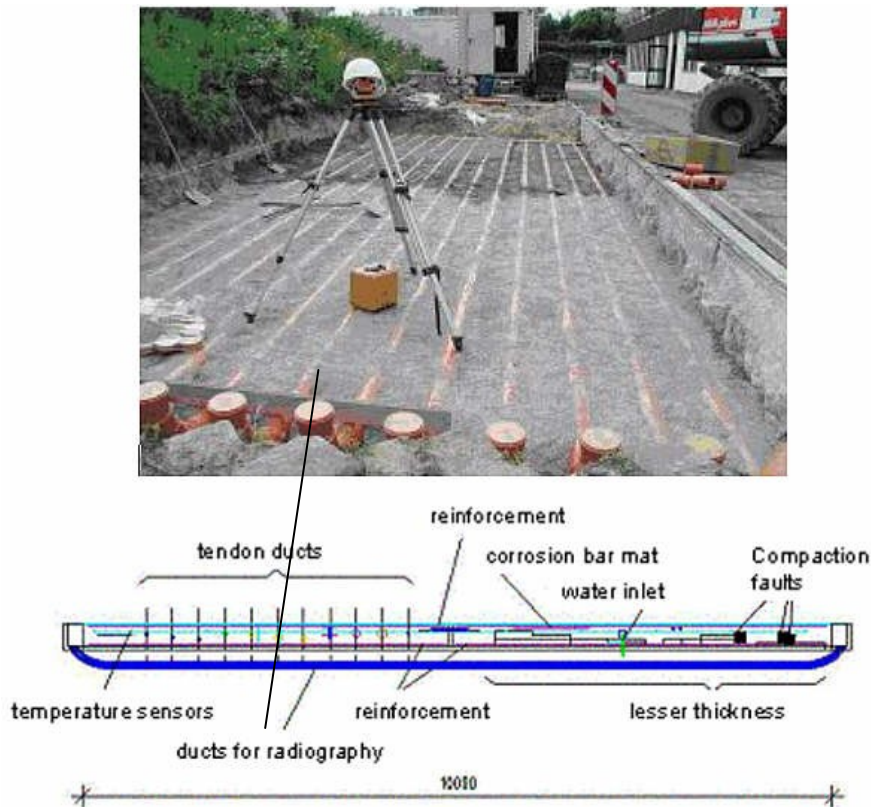


Figure 5.40 Foundation of the slab with ducts to position radiation sources [58].

Strength	C30/37
Water/Cement ratio	0.55
Cement type	CEM II/B-S 32.5 R
Aggregate	Gravel sand mixture, with maximum diameter 16 mm
Additives	Fly ash, plastifying admixture, flux

Table 5.3 Specifications of concrete mixture of LCS.

In the area for corrosion testing, there were two layers of rebars, as shown in Figure 5.41. The first layer has the rebars with 6-mm diameter, 15-cm spacing and 3-cm cover. In order to have contact with the reinforcement for the electrochemical measurement, the rebars were

extended outside the edge to the slab. The second layer is a steel mat, for which the steel bars have a diameter of 8 mm, a spacing of 3 cm and a cover depth of 5 cm. The specifications of the concrete mixture can be found in Table 5.3.

### 5.3.2 Artificial initiation to generate pitting corrosion

In order to totally initiate localized reinforcement pitting corrosion, 7 holes were drilled up to the depth of the steel mat (20-mm diameter) in March 2004 (see Figure 5.41) [59]. Each hole was filled with 15 g NaCl and water to achieve the critical corrosion condition. After the sodium chloride solution was completely sucked in, the holes were closed by repair mortar (Sika 613). Afterwards, the area was wetted and covered with plastic foil for 18 days.

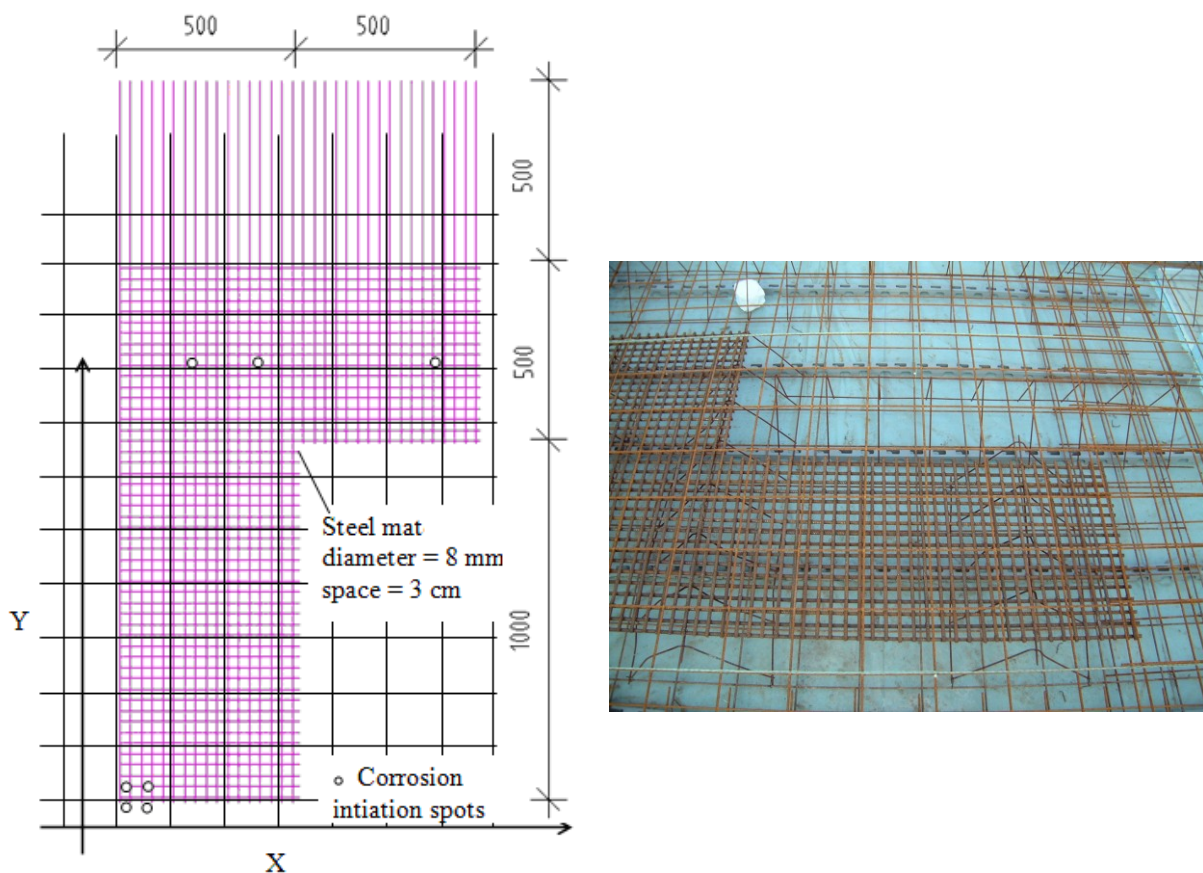


Figure 5.41 Reinforcement of the corrosion testing area of LCS and the positions of corrosion initiation spots.

### 5.3.3 HCP monitoring

HCP measurements were carried out to measure the active corrosion before and after chloride application in 2002, which is part of the work of the “Sustainable Bridge” project funded by

the European Commission within FP6. The measure grid is 10 cm x 10 cm. Ag/AgCl electrode was used. The result measured in March 2004, before chloride application, is shown in Figure 5.42. In the upper part, the potential reading was lower. Since the rebars extended outside the specimen are not protected by the concrete, the corrosion occurred and resulted in the lower potential reading in the area close to the upper edge of the slab.

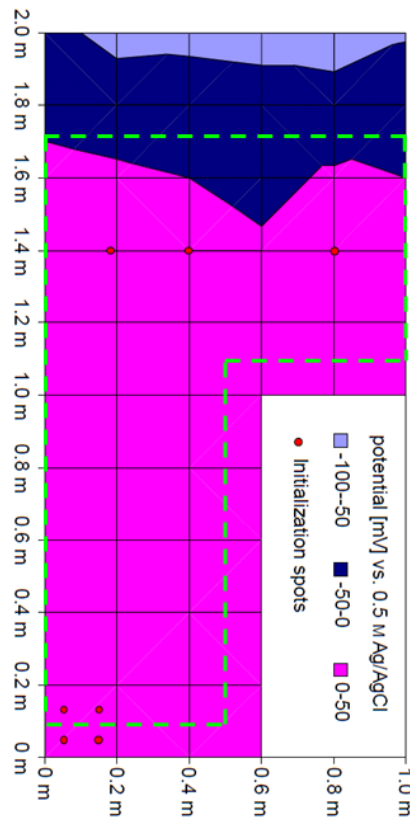


Figure 5.42 Potential mapping measured in March 2004, before installing the corrosion initialization spots [59].



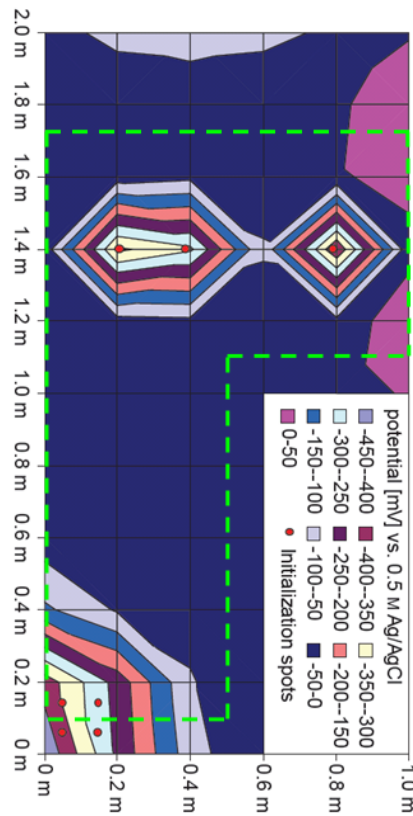


Figure 5.43 Potential mapping measured in April 2004, approximately 3 weeks after installing the corrosion initialization spots [59].

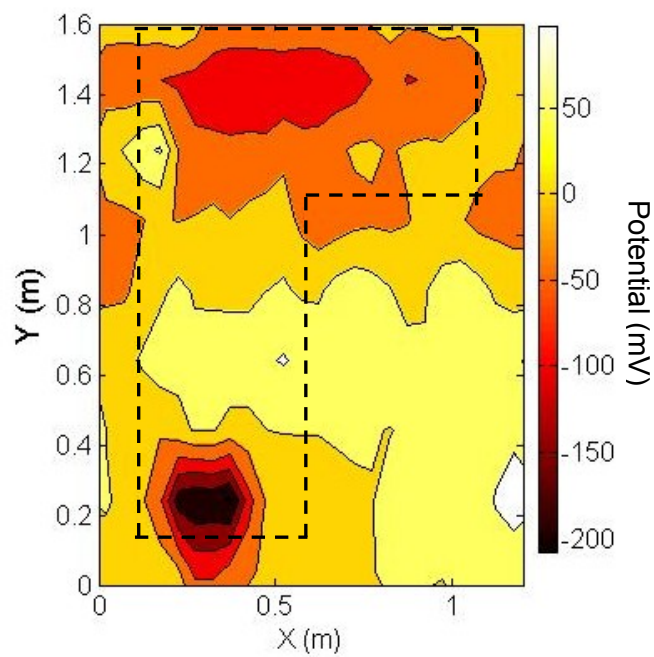


Figure 5.44 Potential mapping measured in May 2011



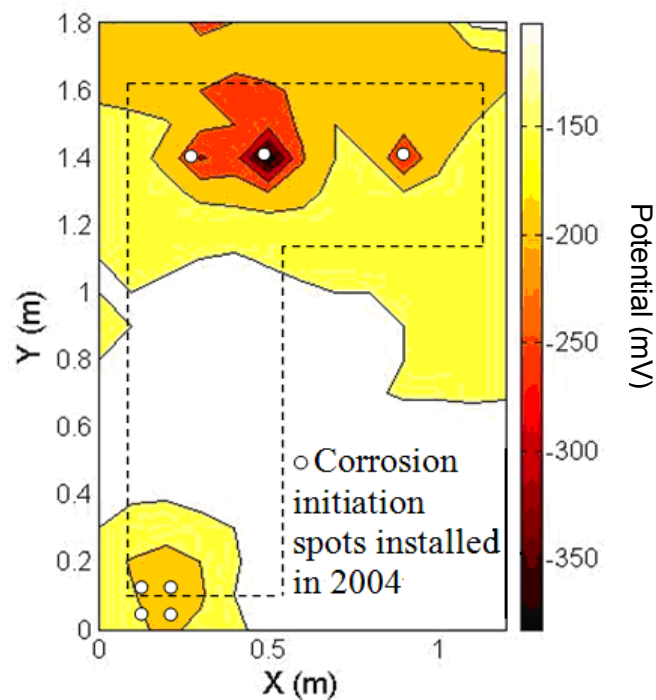


Figure 5.45 Potential mapping measured in August 2013.

Approximately 3 weeks after installing the corrosion spots (April 2004), the HCP measurement was performed, and the obtained potential contour map is shown in Figure 5.43. In the chloride-contaminated area, the potential reading was up to 400 mV more negative than the non-contaminated part, indicating high risk of active corrosion was happening.

I continue the study of reinforcement corrosion on LCS. HCP measurement was performed again in May 2011 and August 2013, with Cu/CuSO<sub>4</sub> electrode. The potential contour mapping obtained in 2011 is shown in Figure 5.44. Compared to the result measured in April 2004, the position of low-potential spot on the lower part of the steel mat shifted a bit to the upper right. The potential in this area is more negative than the other place. In the result obtained in 2013, the low-potential spots were once again identical with the position of the corrosion initiation spots. The potential at the location of C<sub>2</sub> was more negative than that for the other place.

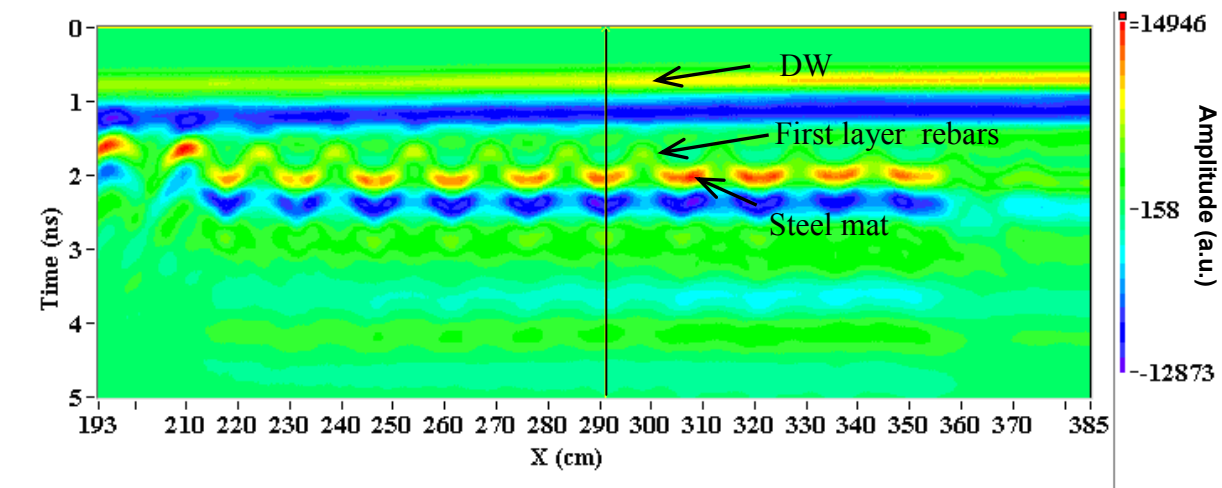
### 5.3.4 GPR-based corrosion monitoring

The old GPR data measured in 2003 and 2005 are available for this study with GSSI 1.5-GHz antenna. A new measurement was performed in August 2013 with GSSI 1.5-GHz and 2.6-

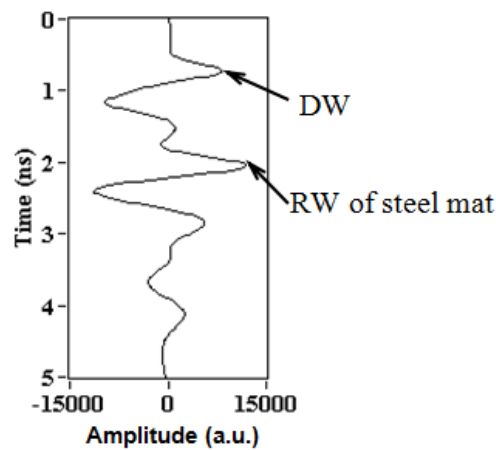
GHz antennas. The measure parameters are summarized in the Table 5.4. The GPR B-scan and A-scan signal are shown in Figure 5.4.

Year	Distance between measure lines (cm)	No. of scans/m	Time window (ns)	No. of points/scan
2003	5	281	10	1024
2005	2.5	448	10	512
2013	2	400	8	1024

Table 5.4 Parameters of the GPR measurements performed in 2003, 2005 and 2013.



(a)

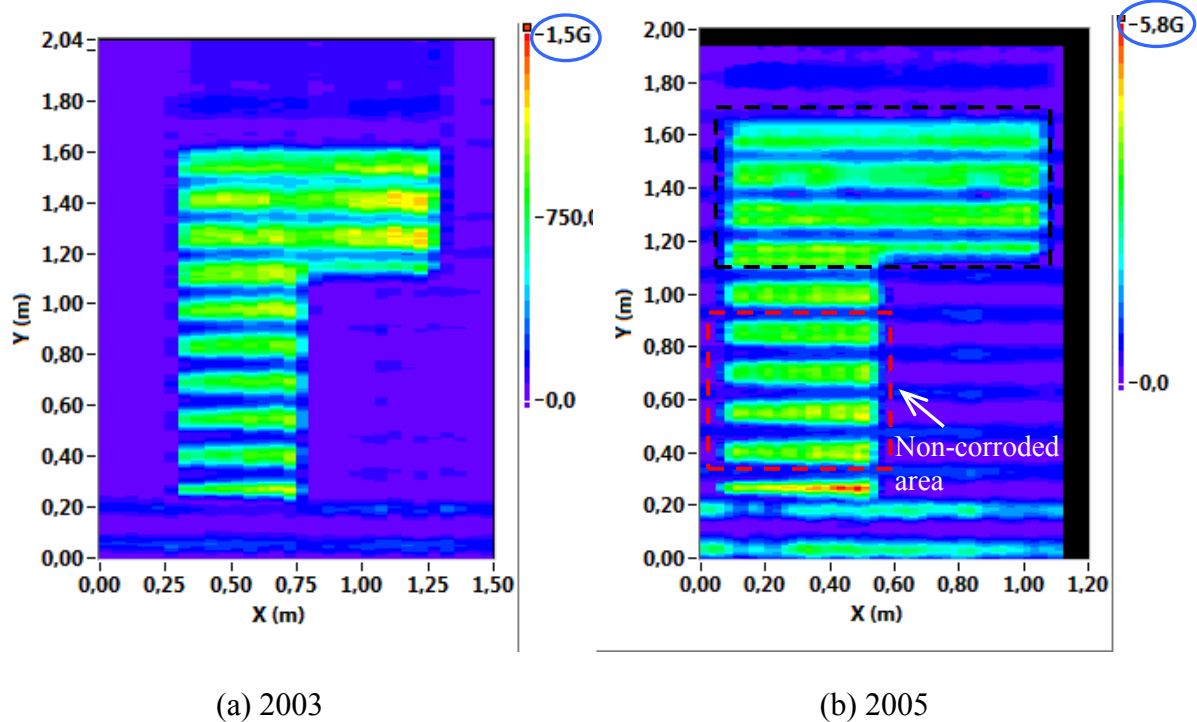


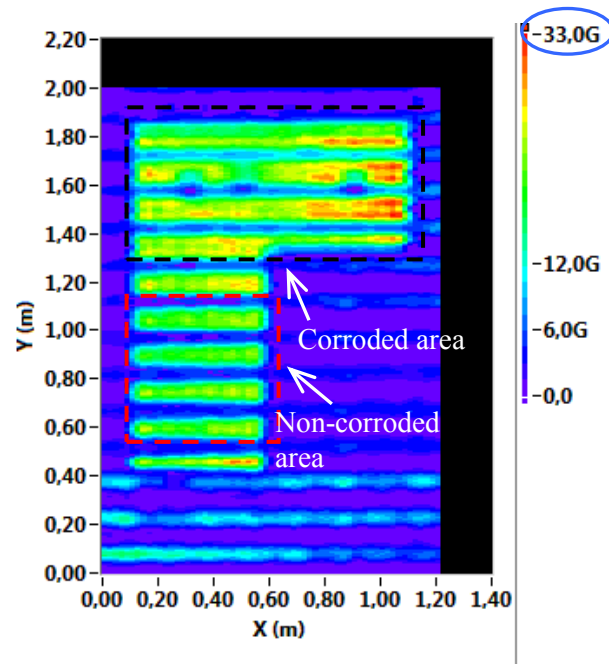
(b)

Figure 5.46 GPR signal: (a) B-scan, (b) A-scan

Figure 5.47 shows the GPR signal energy intensity mapping measured in 2003, 2005 and 2013, since the measurements were performed with different antennas and different measure parameters, in different years. The magnitudes of the GPR energy intensity mapping are very different. In order to compare the result and find out the corrosion area, the results need to be normalize at the same scale.

In this research, a novel method for magnitude normalization based on a mutual-information image registration technique is proposed to align and normalize the image or the datasets to an identical scale. The method and the developed automatic processing toolkit are introduced in Section 4.4.3. From the results in Figure 5.47, the signal energy intensities for the area marked with a red frame were stable and didn't have significant high or low magnitude, which can be considered a non-corroded area. From the result of HCP, there was no active corrosion detected in this area, either. The non-corroded area was selected in one of the images (for example, Figure 5.47 (b)) and automatically searched for the most similar area in another image (Figure 5.47 (c)). The information about the displacement, translation and rotation was obtained and aligned these two images into an identical coordinate system. Then, the relationship of the intensity of these two images was plotted and fitted with a function, as shown in Figure 5.48. It shows that, in the non-corroded area, the relationship of the signal energy magnitude is linear. By using this function, the magnitudes of signal energy intensities in Figure 5.47 (c) were normalized into a scale identical to that in Figure 5.47 (b).





(c) 2013

Figure 5.47 Corrosion visualization with GPR signal energy mapping measured in (a) 2003, (b) 2005 and (c) 2013.

An area with high signal energy intensity was found in the result for 2013, marked with a black frame in Figure 5.47 (b) and (c). According to the result of Experiment 1 and 2, this phenomenon is related to the general corrosion of the reinforcements. Figure 5.49 is the magnitude relationship of this corroded area of the results measured in 2005 (Figure 5.47 (b)) and 2013 (Figure 5.47 (c)). It shows that, in this area, the signal energy measured in 2013 increased significantly compared to the non-corroded area.

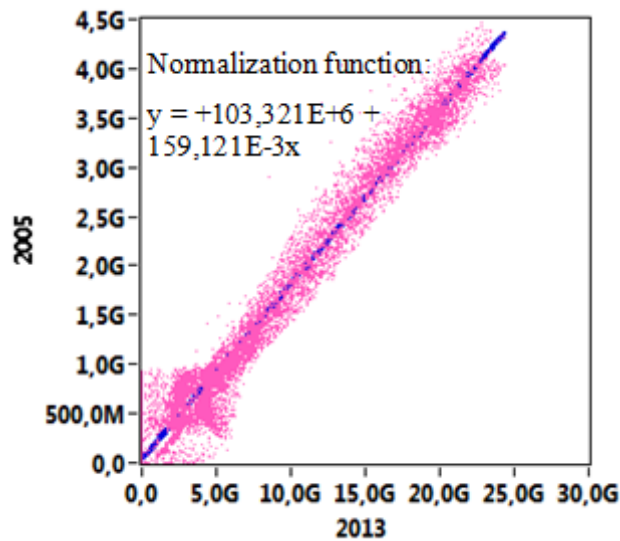


Figure 5.48 Magnitude relationship of the non-corroded area in the energy intensity plots measured in 2005 (Figure 5.47 (b)) and 2013 (Figure 5.47 (c))

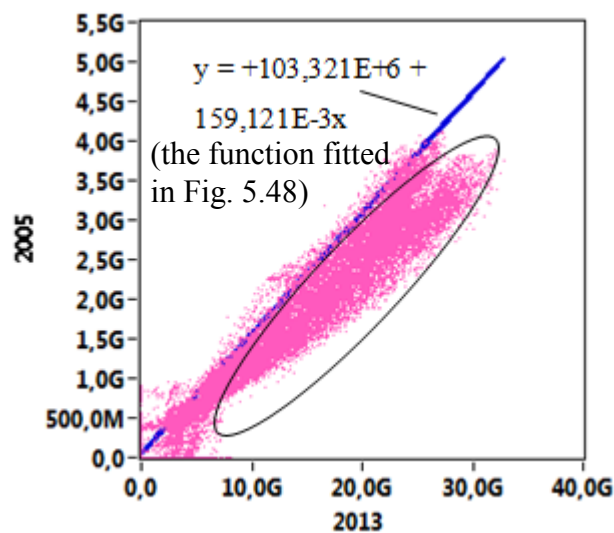
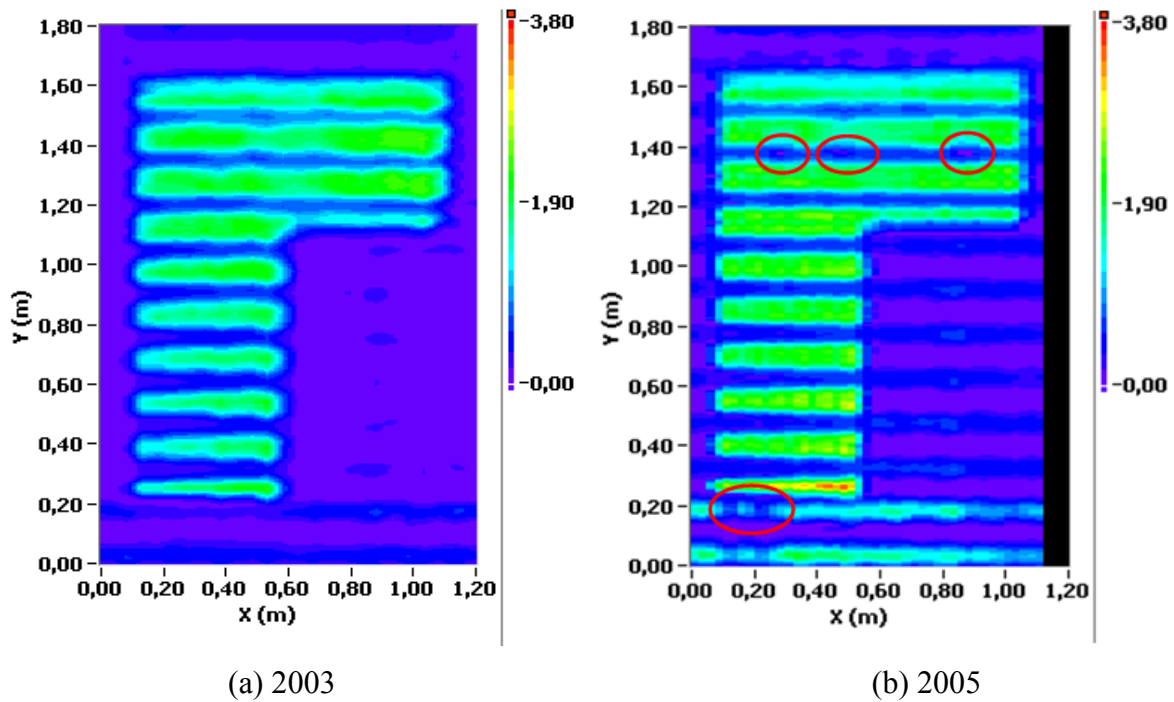


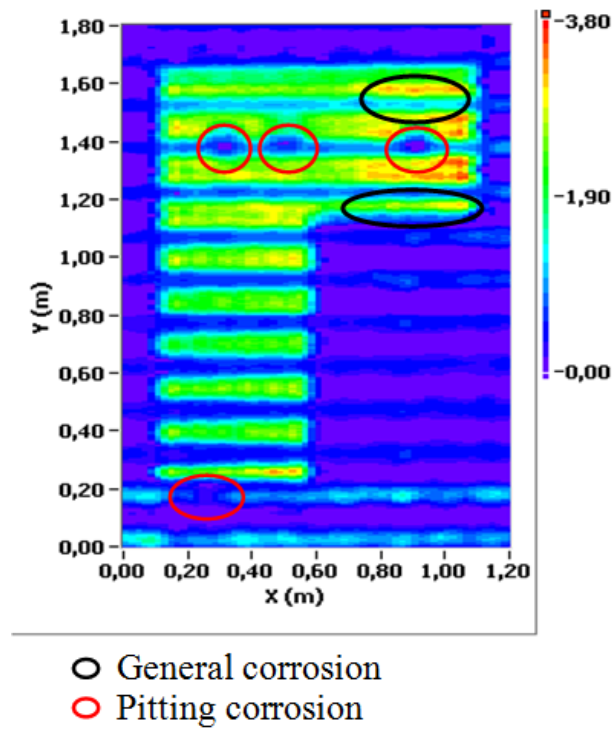
Figure 5.49 Magnitude relationship of the corroded area in the energy intensity plots measured in 2005 (Figure 5.47 (b)) and 2013 (Figure 5.47 (c))

Figure 5.50 (a), (b) and (c) show the energy intensity mapping after normalization. Since the chlorides were applied concentrated, pitting corrosion occurred locally in the area of the corrosion initiation spots. In Figure 5.50 (b), for which the measurement was taken one year after the installation of corrosion initiation spots, the pitting corrosion can be observed with a lower magnitude in the radar graph. In Figure 5.50 (c), the pitting area became bigger compared to Figure 5.50 (b). Figure 5.51 is the energy intensity mapping measured with a

2.6-GHz antenna in 2013. The corrosion pit can be more clearly visualized when a higher frequency antenna was used.

Figure 5.52 shows the mapping of DW peak frequency. In 2005, three out of seven corrosion initiation spots can be detected with low DW peak frequency. In 2013, the measurement was carried out two days after rain. A decrease in frequency can be observed in Figure 5.52 (c) compared to Figure 5.52 (b) due to increased moisture. Six out of seven corrosion initiation spots were detected.





(c) 2013

Figure 5.50 Normalized signal energy intensity mapping for corrosion visualization measured with a 1.5-GHz antenna in (a) 2003, (b) 2005 and (c) 2013.

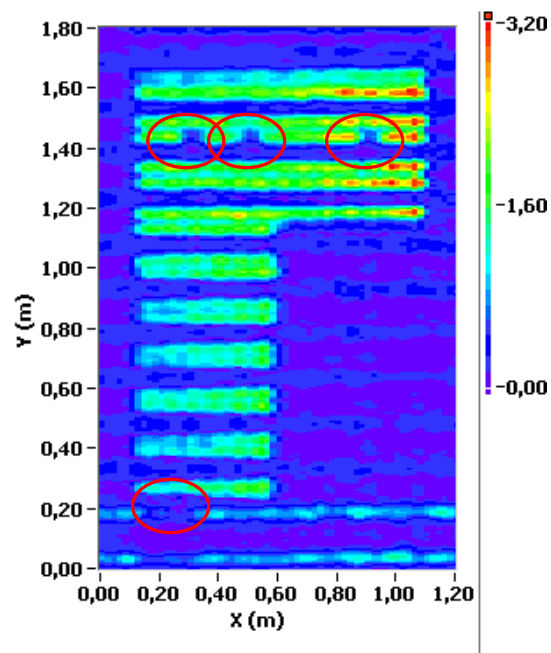
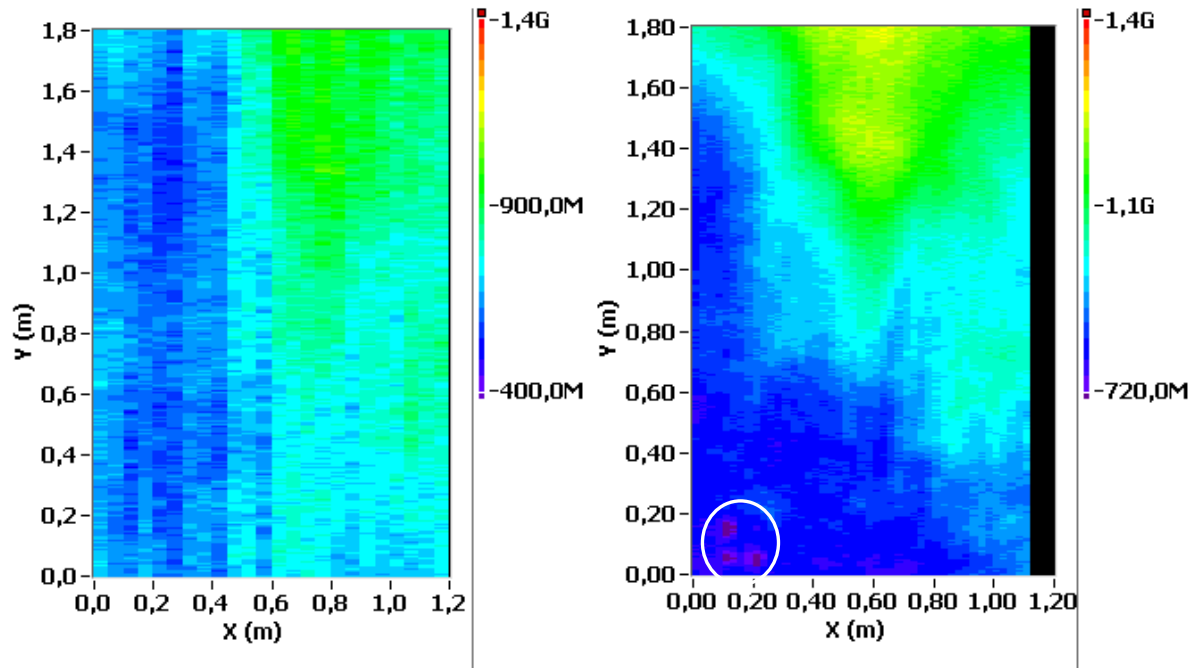
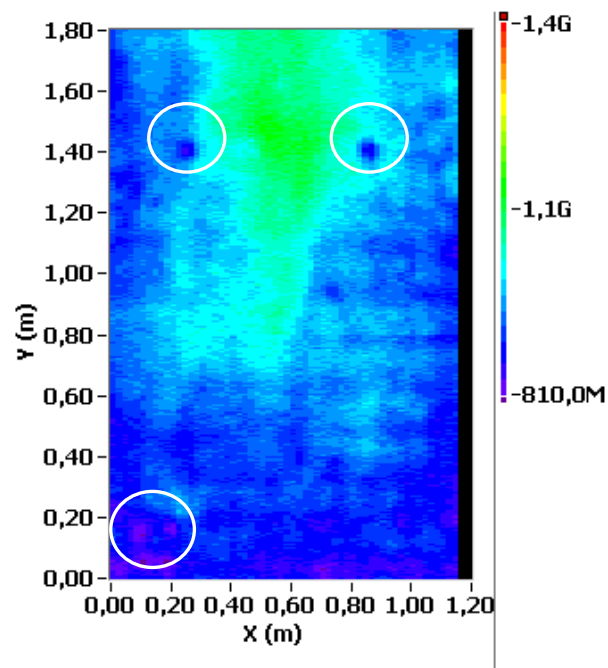


Figure 5.51 Normalized signal energy intensity mapping for corrosion visualization measured with a 2.6-GHz antenna in 2013.



(a) 2004, before installing the corrosion initialization spots.

(b) 2005



(c) 2013

Figure 5.52 Mapping of direct wave peak frequency: (a) 2003, (b) 2005 and (c) 2013.



### 5.3.5 Summary

This experiment showed an example of using GPR for corrosion long-term periodic monitoring. The proposed signal processing methods, which use signal energy for corrosion mapping and DW peak frequency for chloride contamination mapping, were successfully applied to this field testing, since the GPR measurements were carried out in different years with different measurement parameters. A novel method was proposed to align and normalize the magnitude of GPR corrosion mapping based on a mutual-information image registration technique. The normalized corrosion mapping results visualized the development of reinforcement corrosion occurring in the past ten years.



## Chapter 6 Conclusions

This thesis presents an experimental effort of monitoring reinforcement corrosion with Ground-Penetrating Radar (GPR) and the establishment of a novel signal processing procedure to provide valuable quantitative information about corrosion and the distribution of chloride in the cover concrete.

Experiments were carried out to periodically monitor the reinforcement corrosion in laboratory and ambient environment. Several NDT methods were employed to verify the GPR observations and investigation of the mechanism. Data processing in both time and time-frequency domains were performed in LabVIEW<sup>TM</sup> software environment to investigate the change of GPR signal attributes to corrosion process and chloride contamination. The derivate tendencies of the signal changes are summarized in Table 6.1.

	Time domain: Amplitude		Frequency domain: Peak frequency		Governing mechanism
	DW	RW	DW	RW	
Effect of general corrosion	---	↑	---	---	Expansion, cracking and change of concrete-steel interface
Effect of pitting corrosion	---	↓	---	---	Significant loss of steel section
Effect of moisture carrying chloride	↓	↓	↓	↓	Increased conductivity leading to higher signal attenuation
↑ - increase, ↓ - decrease, --- no change.					

Table 6.1 Summary of correspondences and mechanisms for corrosion and chloride contamination with GPR signal attributes.

### • GPR signal responses to reinforcement corrosion

An important finding of this research is that, due to different damage mechanisms, GPR signals have an opposite response to general corrosion and pitting corrosion. For general corrosion, the expansion of rust and cracking results in a larger and multiple interface (including concrete, cracks, rust, air and steel) which manifested the stronger reflection of the GPR signal from the corroded rebar. For pitting corrosion, the significant loss of steel section results in a lower amplitude of the wave reflected from a rebar.

- **GPR-based 2D corrosion mapping**

The related increase/reduction of the reflected wave amplitude can be enhanced by calculating the signal energy of the reflected wave. The results of the laboratory experiments showed that this method holds the potential to visualize corrosion at an early stage, even before cover concrete cracked.

- **GPR-based corrosion long-term monitoring**

There are several parameters that influence the GPR reflected wave amplitude, such as rebar size and cover depth. The proposed method is called “corrosion monitoring” instead of “corrosion detection;” i.e., a baseline measurement is always needed to qualitatively derivate the decay. By comparing the results measured in different years, the development of the reinforcement corrosion process can be visualized.

Since the measurements were performed with different antennas and different measure parameters, in different years, the magnitudes of the GPR energy intensity mapping are very different. In order to compare the result and find out the corrosion area, it is important to normalize the results to an identical scale. A novel method was proposed based on a mutual-information image registration technique to automatically interpolate, align and normalize the magnitude of GPR energy intensity mapping. Then, by comparing the results measured in different years, the cumulative information of corrosion can be quantitatively estimated.

- **GPR signal responses to chloride contamination**

Another important finding is that reinforcement corrosion doesn't change the peak frequency of the direct wave and reflected wave, while high moisture and/or chloride content cause high signal attenuation and downshift the GPR frequency spectra. The peak frequency of GPR direct wave and reflected wave was selected to evaluate the signal attenuation. Theoretically, it is also possible to estimate the EM wave attenuation with other signal attributes, such as amplitude, travel time and wave velocity. However, these attributes are easily influenced by factors such as scattering, geometric spreading and transmission and reflection effects, etc. The frequency of an EM pulse is not affected by geometrical spreading or reflection losses. It can be used as a more reliable attribute than time domain attributes to estimate the signal attenuation.

- **GPR-based 2D chloride mapping**

The chloride-contaminated concrete, which resulted either by the use of de-icing salt or marine exposure, has a very typical chloride depth profile. The chlorides were greatly concentrated in a small region close to the concrete surface. This region is actually where the GPR direct wave propagates through. Thus, the peak frequency of direct wave was finally chosen as an attribute to map the signal attenuation related to chloride contamination. The peak frequency of direct wave was calculated by using S-transform and mapped in 2D. The area with low frequency indicates high chloride and/or moisture content. In the laboratory experiment and the LCS long-term monitoring, the high chloride-contaminated areas were successfully visualized by using this proposed method.

The proposed method was applied to a case study, which showed an example of ten-year long-term periodic monitoring of the reinforcement corrosion under ambient environmental conditions. In order to discover the development of corrosion from the historical GPR data taken over different measure grids and with different measure parameters, a mutual information-based image registration technique was employed to align and normalize GPR data sets. The results successfully visualized the development of corrosion within the last ten years, which warrants the possibilities of further transferring the proposed method to large-scale measurements on site.



## Publications

S.-X. Hong, W.-L. Lai, G. Wilsch, R. Helmerich, R. Helmerich, T. Günther, H. Wiggenhauser, “Periodic Mapping of Reinforcement Corrosion in Intrusive Chloride Contaminated Concrete with GPR”, *Journal of Construction and Building Material*, vol. 66, pp. 671–684, 15 Sep. 2014, DOI: 10.1016/j.conbuildmat.2014.06.019.

S.-X Hong, W. L. Lai, R. Helmerich. “Experimental Monitoring of Chloride-Induced Reinforcement corrosion and Chloride contamination in concrete with Ground Penetrating Radar”, *Journal of Structure and Infrastructure Engineering*, vol. 11, pp. 15-26, 2015, DOI: 10.1080/15732479.2013.879321.

S.-X. Hong, W.-L. Lai, R. Helmerich. “Accelerated Corrosion in Chloride Contaminated Concrete with Ground Penetrating Radar”, *GPR 2012 Conference*, China, June 2012, DOI: 10.1109/ICGPR.2012.6254927

S. Hong, Lai, W. L., Helmerich, R., Milmann, B. (2012). “NDT-Based Monitoring of Accelerated Reinforcement Corrosion in Concrete”, *6th International Conference of Association for Bridge Maintenance and Safety (IABMAS 2012)*, Lake Como, Italy, July 2012, ISBN 978-415-62124.

## References

- [1] P. Schießl and T. F. Mayer, "Final reports on the first phase of the DafStb/BMBF joint research project "Sustainable building with concrete", Subproject A2, "Life management system", " German Committee for Structural Concrete DAfStB 2007.
- [2] B. Elsener, C. Andrade, J. Gulikers, R. Polder, and M. Raupach, "Half-cell potential measurements - Potential mapping on reinforced concrete structures," *Materials and Structures*, vol. 36, pp. 461-471, 2003.
- [3] J. Boll, R. P. G. v. Rijn, K. W. Weiler, J. A. Ewen, J. Dalipathy, S. J. Herbert, and T. S. Steenhuis, "Using ground-penetrating radar to detect layers in a sandy field soil," *Geoderma*, vol. 70, pp. 117-132, 1996.
- [4] N. J. Cassidy, "Evaluating LNAPL contamination using UPR signal attenuation analysis and dielectric property measurements: Practical implications for hydrological studies," *Journal of Contaminant Hydrology*, vol. 94, pp. 49-75, 2007.
- [5] S. E. Kruse, J. C. Schneider, D. J. Campagna, J. A. Inman, and T. D. Hickey, "Ground penetrating radar imaging of cap rock, caliche and carbonate strata," *Journal of Applied Geophysics*, vol. 43, pp. 239-249, 2000.
- [6] M. R. Mahmoudzadeh, A. P. Francés, M. Lubczynski, and S. Lambot, "Using ground penetrating radar to investigate the water table depth in weathered granites — Sardon case study, Spain," *Journal of Applied Geophysics*, vol. 79, pp. 17-26, 2012.
- [7] T. L. Dobecki and S. B. Upchurch, "Geophysical applications to detect sinkholes and ground subsidence," *The Leading Edge*, vol. 25, pp. 336-341, 2006.
- [8] G. Parkinson and C. Ekes, "Ground penetrating radar evaluation of concrete tunnel linings," in 12<sup>th</sup> International Conference on Ground Penetrating Radar, Birmingham, UK 2008.
- [9] T. Saarenketo, "NDT Transportation," in *Ground Penetrating Radar: Theory and Application*, H. M. Jol, Ed.: Elsevier, pp. 395-444, 2009.



- 
- [10] A. Kalogeropoulos, "Non-destructive determination of chloride and water content in concrete using ground penetrating radar," in *The Natural, Architectural and Built Environment Faculty*. vol. PhD: Federal Institute of Technology-Lausanne, 2012.
- [11] K. Tuutti, "Corrosion of steel in concrete," Swedish Cement and Concrete Research Institute, Stockholm 1982.
- [12] K. Hong and R. D. Hooton, "Effects of cyclic chloride exposure on penetration of concrete cover," *Cement and concrete research*, vol. 29, pp. 1379-1386, 1999.
- [13] S. Bioubakhsh, "The penetration of chloride in concrete subject to wetting and drying: measurement and modelling." vol. Doctoral London: University College London, 2011.
- [14] G. Wilsch, F. Weritz, D. Schaurich, and H. Wiggensauser, "Determination of chloride content in concrete structures with laser-induced breakdown spectroscopy," *Construction and Building Materials*, vol. 19, pp. 724-730, 2005.
- [15] Y. Liu and R. E. Weyers, "Modelling the time to corrosion cracking in chloride contaminated reinforced concrete structures," *ACI Materials in Civil Engineering*, vol. 15, pp. 675-681, 1998.
- [16] R. E. Weyers, "Service life model for concrete structures in chloride laden environments," *ACI Materials Journal*, vol. 95, pp. 445-453, 1998.
- [17] "ASTM C876-09, Standard test method for corrosion potentials of uncoated reinforcing steel in concrete. ," American Society for Testing and Material.
- [18] DGZfp, "Merkblatt für elektrochemische potentialmessungen zur ermittlung von bewehrungsstahlkorrosion in stahlbetonbauwerken (B3)," Deutsche Gesellschaft für Zerstörungsfreie Prüfung e.V. Berlin, 2008.
- [19] B. Tred 2000 Ltd, J Broomfield Consultants Risk Review Ltd "Handbook for corrosion rate measurement," in *Corrosion in concrete* vol. Report 2, 2001.
- [20] M. Raupach and P. Schiessl, "Monitoring system for the penetration of chlorides, carbonation and the corrosion risk for the reinforcement " in *Proceedings of the 6th International Conference on Structural Faults and Repair*, 1995.

## References

---

- [21] W. J. McCarter, M. Emerson, and H. Ezirim, "Properties of concrete in the cover zone developments in monitoring techniques," *Magazine of Concrete Research*, vol. 47, pp. 243-251, 1995.
- [22] P. Cosentino, B. Grossman, C. Shieh, S. Doi, H. Xi, and P. Erbland, "Fiber-optic chloride sensor development," *Journal of Geotechnical Engineering*, vol. 121, pp. 610-617, 1995.
- [23] F. J. Arregui, Y. Liu, I. R. Matias, and R. O. Claus, "Optical fiber humidity sensor using a nano Fabry-Perot cavity formed by the ionic self-assemble method," *Sensors and Actuators*, vol. B59, pp. 54-59, 1999.
- [24] P. M. M. Basheer, K. T. V. Grattan, T. Sun, A. E. Long, D. McPolin, and W. Xie, "Fiber optic chemical sensor systems for monitoring pH changes in concrete," in *SPIE 5586, Advanced Environmental, Chemical, and Biological Sensing Technologies II*, Philadelphia, USA, 2004.
- [25] R. M. Narayanan, S. G. Hudson, and C. J. Kumke, "Detection of rebar corrosion in bridge decks using statistical variance of radar reflection pulses," in *7th International GPR Conference Proceeding*, 1998, pp. 601-605.
- [26] S. S. Hubbard, J. Zhang, P. J. M. Monteiro, J. E. Peterson, and Y. Rubin, "Experimental detection of reinforcing bar corrosion using non-destructive geophysical techniques," *ACI Materials Journal*, pp. 100-M85, 2003.
- [27] W.-L. Lai, T. Kind, M. Stoppel, and H. Wiggenhauser, "Measurement of accelerated steel corrosion in concrete using ground-penetrating radar and a modified half-cell potential method," *Journal of Infrastructure Systems*, vol. 19, pp. 205-220, 2013.
- [28] S. Koppenjan, "Ground penetrating radar systems and design," in *Ground Penetrating Radar Theory and Application*, M. J. Harry, Ed., 2009, pp. 73-97.
- [29] J. A. Huisman, S. S. Hubbard, J. D. Redman, and A. P. Anna, "Measuring soil water content with ground penetrating radar: a review," *Vadose zone Journal* vol. 2, pp. 476-491, 2003.

- 
- [30] A. P. Anna and S. W. Cosway, "Ground penetrating radar survey design," in Proceedings of the symposium on the application of Geophysics to engineering and environmental problems, SEGEEP'92, Oakbrook, IL, 1992, pp. 329-351.
- [31] P. J. Bevelacqua, "Antenna arrays: Performance limits and geometry optimization." vol. Doctor of Philosophy: Arizona State University, 2008.
- [32] S. J. Radzevicius and J. J. Daniels, "Ground penetrating radar polarization and scattering from cylinders," Journal of Applied Geophysics, vol. 45, pp. 111-125, 2000.
- [33] N. J. Cassidy, "Electrical and magnetic properties of rocks, soils and fluids," in Ground Penetrating Radar: Theory and Applications, H. M. Jol, Ed., 2009, pp. 41-72.
- [34] U. B. Halabe, A. Sootodehnia, K. R. Maser, and E. A. Kausel, "Modelling the electromagnetic properties of concrete," ACI Materials Journal, vol. 90, pp. 552-563, 1993.
- [35] A. Peyman, C. Gabriel, and E. H. Grant, "Complex permittivity of sodium chloride solutions at microwave frequencies," Bio Electro Magnetics, vol. 28, pp. 267-274, May 2007.
- [36] W.-L. Lai, T. Kind, and H. Wiggemhauser, "A study of concrete hydration and dielectric relaxation mechanism using ground penetrating radar and short-time Fourier transform," Journal on advances in signal processing, vol. 2010 Jan, 2010.
- [37] R. Yelf and D. Yelf, "Where is True Time Zero?," in Ground penetrating radar, GPR 2004, Delft, The Netherlands 2004, pp. 279 - 282
- [38] N. J. Cassidy, "Ground penetrating radar data processing, modelling and analysis," in Ground penetrating radar: theory and application H. M. Jol, Ed., 2009, pp. 141-176.
- [39] H. M. Jol and C. S. Bristow, "GPR in sediments: advice on data collection, basic processing and interpretation, a good practice guide," in Ground Penetrating Radar in Sediments, 2011.
- [40] J. A. Aitken and R. R. Stewart, Shallow GPR and seismic surveying in a carbonated environment: Belize vol. 16, 2004.

- [41] A. V. Ristic, D. Petrovacki, and M. Govedarica, "A new method to simultaneously estimate the radius of a cylindrical object and the wave propagation velocity from GPR data," *Computers and Geosciences*, vol. Vol. 35, pp. 329-347, 2009.
- [42] L. Nuzzo, G. Leucci, S. Negri, M. T. Carrozzo, and T. Quarta, "Application of 3D visualization techniques in the analysis of GPR data for archaeology," *Annals of Geophysics*, vol. 45, pp. 321-337, April 2002.
- [43] U. Böniger, "Attributes and their potential to analyze and interpret 3D GPR data." vol. Dr. rer. nat Potsdam, Germany: University Potsdam, 2010.
- [44] A. H. Nuttall, "Spectral estimation by means of overlapped fast Fourier transform processing of windowed data," Naval Underwater Systems Center, U.S. 1971.
- [45] W. L. Lai, T. Kind, and H. Wiggenhauser, "Using Ground penetrating radar and time-frequency analysis to characterize construction materials," *NDT&E International*, vol. 44, pp. 111-120, 2011.
- [46] R. G. Stockwell, L. Mansinha, and R. P. Lowe, "Localization of the complex spectrum: the S transform," *IEEE Transactions of Signal Processing*, vol. 44, pp. 998-1001, 1996.
- [47] H. Wiggenhauser, "Advanced NDT methods for the assessment of concrete structures," in *Concrete repair, Rehabilitation and retrofitting II*, M. G. Alexander, H. D. Beushausen, F. Dehn, and P. Moyo, Eds. Lodon: Taylor & Francis Group, 2009.
- [48] T. A. E. Maaddawy and K. A. Soudki, "Effectiveness of impressed current technique to simulate corrosion of steel reinforcement in concrete," *Journal of materials in civil engineering*, vol. 15, 2003.
- [49] W. K. Zhao, G. Tian, B. B. Wang, Z. J. Shi, and J. X. Lin, "Application of 3D GPR attribute technology in archaeological investigations," *Applied geophysics*, vol. 9, pp. 261-269, 2012.
- [50] P. Claisse, "Transport properties of concrete," *International Concrete Research & Information Portal*, vol. 27, pp. 43-48, January 2005.

- 
- [51] T. A. E. Maaddawy and K. A. Soudki, "Effectiveness of impressed current Technique to simulate corrosion of steel reinforcement in concrete," *Journal of Materials in Civil Engineering*, vol. 15, pp. 41-47, 2003.
- [52] W. H. Hartt, "Laboratory method for corrosion testing of reinforce concrete using impressed current," *Corrosion*, vol. 133, 1979.
- [53] S. Laurens, J. P. Balayssac, J. Rhazi, and G. Arliguie, "Influence of concrete relative humidity on the amplitude of Ground-Penetrating Radar (GPR) signal," *Materials and Structures*, vol. 35, pp. 198-203, 2001.
- [54] R. L. Roberts and J. J. Daniels, "Modelling near-field of GPR in three dimensions using FDTD method," *Geophysics*, vol. 62, pp. 1114-1126, 1997.
- [55] R. A. V. Overmeeren, S. V. Sariowan, and J. C. Gehrels, "Ground penetrating radar for determining Volumetric soil water content results of comparative measurements at two test sites," *Journal of Hydrology*, vol. 197, pp. 316-338, 1997.
- [56] Z. M. Sbartai, S. Laurens, J. P. Balayssac, G. Arliguie, and G. Ballivy, "Ability of the direct wave of radar ground-coupled antenna for NDT of concrete structures," *NDT&E International*, vol. 39, pp. 400-407, 2006.
- [57] W. D. Grimes, W. H. Hartt, and D. H. Turner, "Cracking of concrete in sea water due to embedded metal corrosion," *National Association of Corrosion Engineers*, vol. 35, pp. 309-316, 1979.
- [58] A. Taffe, K. Borchardt, and H. Wiggemhauser, "Specimen for the improvement of NDT-methods design and construction of a large concrete slab for NDT methods at BAM," in *Non-Destructive Testing in Civil Engineering Berlin, Germany*, 2003.
- [59] R. Bäßler, A. Burkert, and G. Eich, "Electrochemical techniques to detect corrosion stage of reinforcement in concrete structures," *Federal Institute for Material Research and Testing (BAM)*, Berlin, Germany 2005.